



UNIVERSIDAD NACIONAL AUTÓNOMA DE MÉXICO  
PROGRAMA DE POSGRADO EN CIENCIAS FÍSICAS

**CHARACTERIZATION OF THE QUARK-GLUON  
PLASMA USING PARTICLE IDENTIFICATION IN PP  
AND PB-PB COLLISIONS AT THE LHC**

TESIS  
QUE PARA OPTAR POR EL GRADO DE:  
MAESTRO EN CIENCIAS (FÍSICA)

PRESENTA:  
OMAR VÁZQUEZ RUEDA

TUTOR  
DR. ANTONIO ORTIZ VELÁSQUEZ

MIEMBROS DEL COMITÉ TUTOR  
DRA. GABRIELA MURGUÍA ROMERO  
DR. GUY PAIC

CIUDAD UNIVERSITARIA, CD. MX. ABRIL 2018



Universidad Nacional  
Autónoma de México

Dirección General de Bibliotecas de la UNAM

**Biblioteca Central**



**UNAM – Dirección General de Bibliotecas**  
**Tesis Digitales**  
**Restricciones de uso**

**DERECHOS RESERVADOS ©**  
**PROHIBIDA SU REPRODUCCIÓN TOTAL O PARCIAL**

Todo el material contenido en esta tesis esta protegido por la Ley Federal del Derecho de Autor (LFDA) de los Estados Unidos Mexicanos (México).

El uso de imágenes, fragmentos de videos, y demás material que sea objeto de protección de los derechos de autor, será exclusivamente para fines educativos e informativos y deberá citar la fuente donde la obtuvo mencionando el autor o autores. Cualquier uso distinto como el lucro, reproducción, edición o modificación, será perseguido y sancionado por el respectivo titular de los Derechos de Autor.



Universidad Nacional  
Autónoma de México

Dirección General de Bibliotecas de la UNAM

**Biblioteca Central**



**UNAM – Dirección General de Bibliotecas**  
**Tesis Digitales**  
**Restricciones de uso**

**DERECHOS RESERVADOS ©**  
**PROHIBIDA SU REPRODUCCIÓN TOTAL O PARCIAL**

Todo el material contenido en esta tesis esta protegido por la Ley Federal del Derecho de Autor (LFDA) de los Estados Unidos Mexicanos (México).

El uso de imágenes, fragmentos de videos, y demás material que sea objeto de protección de los derechos de autor, será exclusivamente para fines educativos e informativos y deberá citar la fuente donde la obtuvo mencionando el autor o autores. Cualquier uso distinto como el lucro, reproducción, edición o modificación, será perseguido y sancionado por el respectivo titular de los Derechos de Autor.

I would like to dedicate this thesis to my loving parents, Olimpia and Benjamin.



## Acknowledgements

Firstly, I would like to acknowledge Dr. Antonio Ortiz who was my main supervisor during my Master studies. I am really thankful for the confidence and opportunity he gave to conduct an investigation within the ALICE experiment on behalf of the ALICE-ICN-UNAM group. I appreciate the time and efforts that he invested to make my academic and professional profile thrive. I could not be more thankful to him for teaching me how to succeed within an international environment where hard work and perseverance are milestones. I will always remember his saying when facing exhaustion; *Al final habrá buenas recompensas (There will be good rewards at the end of the road)*. Even if those good rewards are only self-satisfaction, it is always worth giving the best of us.

I want to thank Dr. Guy Paic who is the team leader of the ALICE-ICN-UNAM group for his teaching and comments within the group discussions, they have always been fruitful to understand the physics of ultrarelativistic collisions.

I would like also to thank to M.I. Juan Luciano Díaz and Ing. Juan Eduardo Murrieta for the technical support when operating the ICN-UNAM cluster.

Support for this work has been received from CONACyT under the grant number 293375 and PAPIIT-UNAM under Project No. IN102118.



## Abstract

High-energy and relativistic heavy-ion collisions at the CERN Large Hadron Collider (LHC) have marked the beginning of a new era in the field of heavy-ion physics where the creation of a state of matter characterized by extreme conditions of high temperature and energy density has triggered questions such as: does hadronic matter undergo a phase transition to a deconfined quark-gluon plasma in the limit of both, high temperature and almost vanishing baryo-chemical potential?. What are the hadronization mechanisms for the bulk production?. Does the dynamical evolution of the "fireball" can be understood only within a hydrodynamic basis framework?. What are the mechanisms for parton energy-loss?. These questions can be partly addressed through the study of the production of light-flavor charged particles, (i. e. hadrons that have in their content the  $u$ ,  $d$ , and  $s$  quarks). The work in this thesis aims to provide inputs to face the aforementioned questions through a systematic study of the production of identified charged hadrons at the LHC energies. The thesis is organized as follows. In Chapter 1, a summary of the theory of the strong interactions and a description of the QCD phase diagram is presented. In addition, an overview of ultrarelativistic heavy-ion collisions and a short discussion of the Glauber model in nuclear interactions is given. Chapter 2 starts with a description of ALICE (A Large Ion Collider Experiment), mainly focusing on the unique capabilities that it bears to perform particle identification (PID) using the ITS, TOF, TPC and, HMPID detectors. Chapter 3 deals with the measurement of the production of identified charged pions, kaons, and (anti)protons as a function of transverse momentum ( $p_T$ ) in Pb–Pb and pp collisions at  $\sqrt{s_{NN}} = 5.02$  TeV. The techniques used to extract the  $p_T$  spectra of identified charged particles using the TPC (Time Projection Chamber) detector are extensively described. In addition, a detailed description of the relevant contributions to the systematic uncertainties is presented. Chapter 4 is devoted to the physics results, and it is divided into two sections. The former section is dedicated to results from *soft* probes ( $1 < p_T < 2$  GeV/ $c$ , interval in the  $p_T$  spectra) which embraces the centrality dependence of pions, kaons, and (anti)protons spectra, the centrality dependence of the kaon-to-pion and proton-to-pion ratios as well as results from a Blast-Wave model study. Surprisingly, the Blast-Wave model, which is a hydrodynamic basis model is capable to describe simultaneously the spectra of pions, kaons, and (anti)protons for  $p_T$  below 2 GeV/ $c$ .



This is a three-parameter model where  $\langle\beta_T\rangle$  is the average transverse velocity,  $T_{\text{kin}}$  is the freeze-out temperature and  $n$  is the exponent of the velocity profile. It was observed that the expansion velocity ( $T_{\text{kin}}$ ) increases (decreases) with increasing multiplicity. In addition, an increase of approximately 3% of the average transverse velocity with respect to Pb–Pb results at 2.76 TeV for the most central collisions was noticed. Further comparisons to results from Pb–Pb collisions at  $\sqrt{s_{\text{NN}}} = 2.76$  TeV are highlighted. The latter section is devoted to discuss the results from *hard* probes. This includes the centrality dependence of the nuclear modification factor  $R_{\text{AA}}(p_T)$ . Furthermore, it includes results from a study of the fractional momentum loss ( $S_{\text{loss}}$ ) as a function of the characteristic path-length ( $L$ ) and the Bjorken energy density times the equilibration time ( $\epsilon_{\text{Bj}}\tau_0$ ) at different  $\sqrt{s_{\text{NN}}}$ . The study has been conducted using public results of inclusive and identified charged hadrons from intermediate to large transverse momentum ( $5 < p_T < 20$  GeV/ $c$ ). Within uncertainties and for all the transverse momentum values which were explored, we have observed that the functional form of  $S_{\text{loss}}$  vs.  $(\epsilon_{\text{Bj}}\tau_0)^{3/8}L$  seems to follow a universal linear scaling. Chapter 4 summarizes the physics results achieved in the study of the measurement of identified charged particles.

---

## Resumen

La presente tesis consistió en la medición de la producción de piones, kaones y protones en colisiones Pb-Pb y pp a la energía de  $\sqrt{s_{NN}} = 5.02$  TeV y  $\sqrt{s} = 5.02$  TeV, respectivamente usando el detector TPC. El contenido de esta tesis se resume por capítulo de la siguiente manera:

- El Capítulo 1 expone un breve resumen acerca de la teoría de la cromodinámica cuántica (QCD), la cual describe de manera fundamental las interacciones fuertes. También se integra una breve discusión acerca de las colisiones nucleares y sus diferentes fases, desde inicios de la colisión, creación del plasma de quarks y gluones hasta el desacoplamiento de los hadrones del medio hadrónico.
- El Capítulo 2 expone las características del detector ALICE y resalta las cualidades únicas que posee para la identificación de partículas. Además se expone con gran detalle al detector TPC.
- En el Capítulo 3 se discute de manera extensa la técnica para la medición de la producción de hadrones identificados en colisiones Pb-Pb y pp a la energía de  $\sqrt{s_{NN}} = 5.02$  TeV. Detalles acerca de las correcciones y una amplia discusión del estudio de las incertidumbres sistemáticas se dan también en este capítulo.
- El Capítulo 4 está dividido en dos secciones. En la primera sección se discuten los resultados de *física suave* mientras que en la segunda se discuten resultados de *física dura*.
- El Capítulo 5 finalmente enlista las conclusiones y contribuciones al campo de la física de colisiones de iones pesados.

Las colisiones ultra relativistas de iones pesados en el Large Hadron Collider (LHC), han confirmado la creación de un medio deconfinado de quarks y gluones altamente denso, denominado, el plasma de quarks y gluones (QGP) [1]. La existencia de este medio ha sido previamente confirmada experimentalmente en el Super Proton Synchrotron (SPS) [2] y el Relativistic Heavy Ion Collider (RHIC) [3–5]. Experimentalmente también se ha confirmado que este medio posee propiedades semejantes a las de un líquido perfecto [5, 6]. El programa de física de iones pesados del LHC está enfocado en expandir el régimen de energía hasta poco más de veinte veces la alcanzada en RHIC, además de llevar a cabo mediciones más precisas que permitan estudiar las propiedades del QGP.

El experimento ALICE del LHC [7, 8] está dedicado al estudio de las propiedades del QGP mediante colisiones de Plomo-Plomo (Pb-Pb), protón-Plomo (p-Pb) y protón-protón (pp).

En una colisión frontal entre dos iones de plomo (Pb-208), la producción de partículas es superior en hasta tres órdenes de magnitud a la de una colisión pp. Debido a que el estudio de las propiedades del QGP se lleva a cabo mediante mediciones en estados finales i.e., piones, kaones, protones, electrones, etc., y además de que varios de los fenómenos atribuidos al QGP dependen de la masa o especie de la partícula, la identificación precisa y medición de la producción de hadrones en un amplio rango de momento transversal ( $p_T$ ) es uno de los objetivos primordiales de ALICE.

ALICE (ver Fig. 2.1) tiene una geometría cilíndrica cuyas dimensiones generales son de 26 m de longitud y 16 m de alto y 16 m de ancho. El sistema de subdetectores del barril central el cual cubre el intervalo de  $45^\circ$  hasta  $135^\circ$  del ángulo polar y la región completa del ángulo azimutal está rodeado por un solenoide que provee un campo magnético con una intensidad de,  $0.2\text{ T} \leq B \leq 0.5\text{ T}$ . La muestra de datos para la medición de la producción de hadrones identificados (PID) en la región de rapidéz central ( $|y| < 0.5$ ) en colisiones Pb-Pb a la energía de  $\sqrt{s_{NN}} = 5.02\text{ TeV}$  fue de 9.5 millones de eventos de baja intensidad durante la corrida 2 del LHC en el año 2015, mientras que para la misma medición usando el detector HMPID, una muestra de 100 millones de eventos fue usada debido a su menor aceptación. El mismo análisis de PID en colisiones pp requirió el uso de aproximadamente 65 millones de eventos. El estudio de las propiedades del QGP mediante los espectros de momento transversal requieren que este último abarque un amplio rango ( $0.2 < p_T < 20\text{ GeV}/c$ ), para ello, los diferentes subdetectores del barril central; ITS, TPC, TOF y HMPID son empleados en análisis independientes. La Tabla 3.4 y Tabla 3.5 listan los intervalos en los cuales los diferentes subdetectores pueden hacer mediciones de PID en colisiones Pb-Pb y pp, respectivamente. Este trabajo de tesis está enfocado a la medición de la producción de hadrones identificados en colisiones Pb-Pb y pp a la energía de  $\sqrt{s_{NN}} = 5.02\text{ TeV}$  y  $\sqrt{s} = 5.02\text{ TeV}$ , respectivamente usando el detector TPC de ALICE. Es por ello que se pone énfasis en la descripción de los análisis usando la TPC y sólo se hará mención de los demás subdetectores.

El detector ITS (Inner Tracking System) [7] lo conforman 6 capas de subdetectores de silicio y es usado principalmente para rastreo, reconstrucción del vértice primario de interacción de la colisión y como un sistema de disparo. Por su parte, también puede realizar identificación de partículas por medio de la pérdida de energía específica ( $dE/dx$ ) cuya resolución es del orden de 6.5% en colisiones centrales de Pb-Pb (ver Fig. 2.2). La medición de la producción de hadrones identificados con el detector TOF (Time Of Flight) [7] está basada en la parametrización de las distribuciones de tiempo de vuelo de las partículas que surgen

del vértice primario de interacción hasta su llegada al detector en función del momento (ver Fig. 2.2). El detector HMPID (High Momentum Particle Identification) [7] consiste en siete contadores RICH (Ring Imaging Cherenkov) de enfoque de proximidad idénticos. La medición de la producción de partículas identificadas se hace mediante la parametrización de la correlación entre el ángulo de Cherenkov ( $\theta_{CH}$ ) y el momento (ver Fig. 2.2) usando la suma de tres funciones Gaussianas.

El detector TPC (Time Projection Chamber) [7] es el principal aparato de rastreo de ALICE. Por sí solo puede hacer identificación de partículas por medio de la  $dE/dx$ . En un ambiente de alta densidad de partículas (colisiones centrales), la resolución de la  $dE/dx$  es de aproximadamente 8%.

Como a continuación se describirá, la medición de la producción de hadrones identificados se ha hecho en dos análisis independientes. En el primer análisis, la medición se lleva a cabo en el intervalo,  $0.2 < p_T < 0.1 \text{ GeV}/c$  y comunmente nos referimos a él como el análisis del bajo  $p_T$ . El segundo análisis comprende el intervalo de momento transverso,  $2 < p_T < 20 \text{ GeV}/c$  y nos referiremos a él como el análisis de la subida relativista (rTPC) o alto  $p_T$ .

En la región de momento ( $0.2 < p < 1 \text{ GeV}/c$ ) donde la señal de  $dE/dx$  entre todas las especies está bien separada (ver Fig. 2.2), una técnica de identificación basada en la parametrización de la distribución del número de sigmas en subintervalos de momento con una función Gaussiana puede dar información acerca de la producción de las diferentes especies (ver Fig. 3.1). La distribución del número de sigmas se define como la diferencia entre el valor medido de la  $dE/dx$  y el valor dado por la curva de Bethe-Bloch (ver App. A). Es posible hacer identificación de partículas en la subida relativista ( $2 < p < 20 \text{ GeV}/c$ ) debido a que la correlación  $dE/dx$  vs.  $\beta\gamma$ , obedece el comportamiento de la forma funcional;  $\log(\beta\gamma)$  en el intervalo ( $3 < \beta\gamma < 1000$ ), donde  $\beta\gamma$  se define como el cociente entre momento y masa de la partícula. Además, la casi constante separación entre piones, kaones y protones permite explotar el uso de las curvas de Bethe-Bloch ( $\langle dE/dx \rangle$  vs.  $\beta\gamma$ ) y resolución relativa ( $\langle dE/dx \rangle / \sigma_{\langle dE/dx \rangle}$  vs.  $\langle dE/dx \rangle$ ) (ver Fig. 3.23). En la subida relativista, la medición de la producción de hadrones identificados en diferentes subintervalos de momento se obtiene mediante la parametrización de la  $dE/dx$  usando la suma de cuatro funciones Gaussianas que describen la señal de piones, kaones, protones y electrones, respectivamente. Los valores de  $\langle dE/dx \rangle$  y  $\sigma_{\langle dE/dx \rangle}$  se obtienen de las parametrizaciones de la curva de Bethe-Bloch y resolución relativa, respectivamente.

El conjunto de correcciones aplicadas al espectro de momento transverso se resume de la siguiente manera (ver Sec. 3.1.5):

- EFICIENCIA. La corrección por eficiencia de rastreo (ver Fig. 3.5) se aplica en función de la especie. Para el caso del análisis de bajo momento transversal, la corrección se aplica también en función de la carga.
- GEANT3/GEANT4. La eficiencia de rastreo para antiprotones ( $\bar{p}$ ) es corregida dado que las interacciones hadrónicas con el material del detector están subestimadas por los actuales generadores de eventos. La misma corrección se aplica en ambos análisis, pp y Pb-Pb.
- GEANT-FLUKA. Es una corrección por absorción y es aplicada a la eficiencia de rastreo para antikaones ( $K^-$ ). La misma corrección se aplica en ambos análisis, pp y Pb-Pb.
- FEED-DOWN. Dado que la contaminación por partículas secundarias; productos de decaimientos débiles ( $\Lambda^0$  y  $K_S^0$ ) y de interacciones con el material son relevantes primordialmente para (anti)protones, aunado que la producción de extrañeza en los actuales generadores de eventos es subestimada, se corrige por dicha contaminación basándose en una combinación entre datos y Monte Carlo. La corrección por feed-down consiste en describir las distribuciones de distancia de máximo acercamiento al vértice de interacción en el plano transversal ( $DCA_{xy}$ ) usando una combinación de distribuciones de Monte Carlo (“templates”) que describan la contribución de partículas primarias, secundarias por decaimientos débiles y secundarias por interacción con el material (ver Figs. 3.7, 3.8, 3.9, 3.10, 3.11).

El estudio de las incertidumbres sistemáticas se ha hecho de manera independiente para ambos análisis y las diferentes componentes se pueden clasificar de manera general en dos grupos.

1. Variación en los cortes para la selección de eventos y trazas (ver Sec. 3.1.7).

Estas componentes se aplican de manera común a ambos análisis. El sistemático asociado a la selección de eventos es del orden del 0.5%. La incertidumbre sistemática en la selección de trazas se obtuvo variando los parámetros como lo muestra la Tabla 3.2. La máxima diferencia entre el espectro de momento transversal inclusivo de partículas cargadas nominal y el espectro de momento transversal inclusivo después de la variación en los cortes es asociado al error sistemático.

2. Errores sistemáticos asociados a la identificación de partículas en la región del bajo  $p_T$  (ver Sec. 3.1.7).

- Se estudió el efecto de cambiar el número de cluster ( $N_{cl}$ ) usados para la reconstrucción de la  $dE/dx$ . El valor nominal fue de 70 y fue variado a 90. La máxima desviación en la razón de partículas cuando se usa  $N_{cl} = 70$  y  $N_{cl} = 90$  fue asignado como incertidumbre sistemática (ver Sec. 3.1.7).
- Se cambió la estrategia para la extracción de la producción de partículas. En lugar de parametrizar las distribuciones de  $N_\sigma$  mediante un ajuste, se hizo conteo de bins en el intervalo,  $[-3\sigma, +3\sigma]$  (ver Sec. 3.1.1 y Sec. 3.1.7).
- El intervalo para la estimación de la contaminación por partículas secundarias en el ajuste de las distribuciones de  $DCA_{xy}$  fue variado de  $[-3\text{cm}, +3\text{cm}]$  a  $[-1\text{cm}, +1\text{cm}]$  (ver Sec. 3.1.7).

La incertidumbre sistemática total es la suma en cuadratura de todas las componentes (ver Figs. 3.16, 3.17, 3.18 ). La incertidumbre sistemática total para piones, kaones y protones con carga negativa en colisiones centrales tienen como valor máximo 2.8%, 5% y 6%, respectivamente.

3. Incertidumbres sistemáticas asociados a la identificación de partículas en la región de la subida relativista (ver Sec. 3.2.10).

Esta incertidumbre sistemática en la identificación de partículas es generada por la imprecisa parametrización de las curvas de Bethe-Bloch y resolución relativa. Dado que para todas las centralidades se parametrizaron curvas distintas, se estimó de manera conjunta la diferencia entre el punto usado para parametrizar y el valor evaluado en la parametrización, estos resultados están resumidos en las Figs. 3.30, 3.31 para colisiones Pb-Pb y pp, respectivamente. Las curvas de color rojo en las mismas figuras representan la parametrización a los valores de desviación estándar de todas las diferencias previamente mencionadas. A su vez, las curvas rojas representan las cotas inferior(superior) en la cual los valores de  $\langle dE/dx \rangle$  y  $\langle dE/dx \rangle / \sigma_{\langle dE/dx \rangle}$  pueden variar para la descripción de la  $dE/dx$ .

Habiendo resumido el análisis de identificación de partículas, se discutirán los resultados.

Como se mencionó, la medición de la producción de piones, kaones y protones incluye seis análisis, cuyos resultados fueron combinados. La diferencia entre el resultado combinado y los resultados individuales están dentro de las incertidumbres sistemáticas y es menor al 10%

(ver Fig. 3.39).

### *Discusión de resultados de física suave*

La Fig. 4.1 muestra el espectro de momento transverso de piones, kaones y protones para diferentes centralidades. Es notorio que el espectro de protones tiende a hacerse plano en la región de bajo momento transverso. Este efecto es atribuido a flujo radial [9], el cual es un efecto de tipo hidrodinámico reflejado en partículas de bajo momento transverso que sufren de un “boost” colectivo de tal manera que partículas de bajo momento transverso son suprimidas y la producción de aquellas con momento transverso de alrededor de 150 MeV/ $c$  incrementa. De manera similar, los efectos del flujo radial se pueden visualizar en la Fig. 4.2, donde se muestra la dependencia con la centralidad de la razón proton a pión. La razón exhibe un máximo de  $\approx 0.85$  ( $\approx 0.38$ ) al rededor del valor de 3 GeV/ $c$  para colisiones centrales (periféricas). La Fig. 4.2 también muestra una comparación con resultados de colisiones Pb-Pb a la energía de  $\sqrt{s_{NN}} = 2.76$  GeV y se puede observar que a la energía de 5.02 TeV, el pico está recorrido hacia la derecha con respecto del pico a 2.76 TeV, este efecto da indicios de la presencia de mayor flujo radial el cual se estimó de ser  $\approx 3\%$  mayor a 5.02 TeV. En [10] se reportó que modelos de hadronización basados en recombinación de partones [11–13] que describen de manera exitosa la producción de hadrones en la región de momento transverso menor a 5 GeV/ $c$  pueden describir también la razón barión a mesón. Es importante también notar que para todas las centralidades la descripción cualitativa es similar.

El modelo hidrodinámico de Blast-Wave introducido por Schnederman *et al.* [14] es usado para describir la evolución de la forma espectral de colisiones centrales a periféricas. Para ello, se realiza un ajuste simultáneo a la distribución de momento transverso de piones, kaones y protones usando la Eq. 4.1. Este modelo comprende tres parámetros libres;  $T_{kin}$  (temperatura de fijamiento cinético),  $\langle\beta_T\rangle$  (rapidéz transversa promedio de expansión del medio hadrónico) y  $n$  (exponente de la rapidéz de expansión). Debido a que los valores de los parámetros son sensibles a los intervalos de ajuste, los rangos utilizados fueron; 0.5-1 GeV/ $c$ , 0.2-1.5 GeV/ $c$  y 0.3-3 GeV/ $c$  para piones, kaones y protones, respectivamente. La Fig. 4.4 (izquierda) muestra el acuerdo entre modelo y datos, mostrando a su vez un mejor acuerdo para colisiones centrales. La Fig. 4.4 (derecha) muestra la correlación entre  $\langle\beta_T\rangle$  y  $T_{kin}$ . La escala de colores está asociada con la densidad de multiplicidad promedio en la región de rapidéz central. Se puede observar que yendo de colisiones periféricas a colisiones entras, los valores de  $\langle\beta_T\rangle$  ( $T_{kin}$ ) incrementan (decrecen), respectivamente. Además, para colisiones centrales,  $T_{kin} \approx 90$  MeV está por debajo del valor esperado para la transición de

fase de QCD ( $\approx 157$  MeV) de un medio confinado a un medio deconfinado [15]. Por tanto, la diferencia entre la temperatura para la transición de fase y  $T_{\text{kin}}$  puede dar una evidencia indirecta de la existencia de una fase de gas hadrónico, dentro de las severas limitaciones del modelo de Blast-Wave.

### *Discusión de resultados de física dura*

Los efectos como la supresión de jets y la pérdida de energía inducida cuando un partón energético atraviesa el medio del QGP [16] puede ser estudiada experimentalmente por medio del factor de modificación nuclear ( $R_{AA}$ ) [17] (ver Eq. 4.2), el cual se define como el cociente entre el espectro de momento transverso en colisiones nucleares y el espectro de momento transverso en colisiones pp normalizado por el número promedio de colisiones binarias,  $\langle N_{\text{coll}} \rangle$ , el cual se obtiene de simulaciones de Glauber [18] (ver Sec. 1.2). En la ausencia de efectos inducidos por el medio, esta razón sería aproximadamente igual a la unidad ( $R_{AA} \approx 1$ ) pues las colisiones nucleares serían descritas simplemente como una superposición lineal de colisiones binarias de tipo minimum bias pp (donde hasta ahora no hay pruebas de la creación de un QGP). Sin embargo, la Fig. 4.5 muestra la dependencia del factor de modificación nuclear con el momento transverso para diferentes centralidades. Se observa que para cualquier centralidad y un valor de momento transverso mayor a  $8$  GeV/ $c$ , el factor de modificación nuclear de los mesones comparten el mismo comportamiento tanto cualitativo como cuantitativo. También se observa que por debajo del mismo valor de momento transverso, los efectos de flujo y recombinación se manifiestan para el caso de protones, donde se observa una menor supresión al rededor de  $4$  GeV/ $c$ . Además, en [19] se reportó que el factor de modificación nuclear para piones, kaones y protones en un intervalo de momento transverso mayor a  $10$  GeV/ $c$  tienen todos el mismo comportamiento cualitativo y cuantitativo dentro las incertidumbres sistemáticas. Finalmente, se observó que la mayor supresión está asociada con colisiones centrales.

La pérdida de momento fraccional ( $S_{\text{loss}}$ ) de hadrones de alto momento transverso definida por la colaboración PHENIX [20] puede usarse como una medida alternativa al factor de modificación nuclear para estudiar la pérdida de energía de partones de alto momento. En [21, 22] se reporta que la pérdida de energía de estos partones está dominada por procesos de tipo pQCD: radiación inducida de gluones que sufren múltiples dispersiones con los constituyentes del medio. La pérdida de momento fraccional reflejaría la pérdida de energía fraccional promedio ( $\langle \Delta E/E \rangle \sim S_{\text{loss}}$ ) inicial de un partón energético al atravesar el QGP. La forma funcional de  $S_{\text{loss}}$  está dada por la Ec. 4.9 (ver Sec. 4.2.2) donde el cambio en



momento transverso ( $\delta p_T \equiv p_T^{\text{pp}} - p_T^{\text{AA}}$ ) con  $p_T^{\text{AA}}$  ( $p_T^{\text{pp}}$ ) igual a los valores de momento transverso en colisiones A-A(pp), respectivamente. La medición en colisiones pp es escalada por  $\langle N_{\text{coll}} \rangle$  asociado a la respectiva clase de centralidad. Asumiendo la validez del escalamiento por  $\langle N_{\text{coll}} \rangle$  y que las funciones de fragmentación no cambian de colisiones pp a colisiones A-A,  $\delta p_T$  reflejaría la pérdida de momento (energía) para que la producción de hadrones en colisiones A-A sea igual a la producción en colisiones pp. Tomando en cuenta la interrelación entre la pérdida de energía y el decaimiento de la sección eficaz en colisiones pp, la expresión para el cambio de momento transverso sería dada por  $\delta p_T \approx (p_T \omega_c)^{1/2}$ . Considerando  $\omega_c = \hat{q}L^2/2$  y a partir de cálculos ideales de pQCD donde  $\hat{q} \propto \varepsilon^{3/4}$  [23] siendo  $\varepsilon$  igual a la densidad de energía del sistema y  $L$  una longitud característica que el partón atravesaría dentro del QGP, se esperaría que  $\delta p_T \approx p_T^{1/2} \varepsilon^{3/8} L$ . La estimación de  $L$  está basada en consideraciones geométricas de colisiones nucleares y su estimación se obtuvo de simulaciones de Glauber (ver Sec. 4.2.2). La densidad de energía se calculó basándose en la definición de la densidad de energía de Bjorken ( $\varepsilon_{\text{Bj}}$ ) [24].

En un artículo que publicamos en 2018 [25] se reportaron las siguientes correlaciones:

1.  $S_{\text{loss}}$  vs.  $\varepsilon_{\text{Bj}} \tau_0$
2.  $S_{\text{loss}}$  vs.  $(\varepsilon_{\text{Bj}} \tau_0)^{3/4} L^2$
3.  $S_{\text{loss}}$  vs.  $(\varepsilon_{\text{Bj}} \tau_0)^{3/8} L$

La Fig. 4.7 muestra la correlación (1) para tres diferentes valores de  $p_T^{\text{pp}}$ : 5 GeV/ $c$  (izquierda), 10 GeV/ $c$  (centro) y 15 GeV/ $c$  (derecha). Para valores de momento transverso mayor a 10 GeV/ $c$ , la pérdida de momento fraccional incrementa linealmente con la densidad de energía. Se observó que la pendiente para resultados de RHIC es más pronunciada que la de los resultados en el LHC. Para valores de  $p_T^{\text{pp}} \approx 5$  GeV/ $c$  sabemos que otros efectos como flujo son relevantes por lo que observamos un cambio sutil en el cambio de la pendiente, es decir, no se verifica  $S_{\text{loss}} \propto \varepsilon_{\text{Bj}} \tau_0$ .

La Fig. 4.8 muestra la correlación (2) para tres diferentes valores de  $p_T^{\text{pp}}$ : 5 GeV/ $c$  (izquierda), 10 GeV/ $c$  (centro) y 15 GeV/ $c$  (derecha). Se observa que para todos los valores de  $p_T^{\text{pp}}$  explorados, el comportamiento no es lineal además de que la extrapolación a  $(\varepsilon_{\text{Bj}} \tau_0)^{3/4} L^2 = 0$  no da como resultado una pérdida de momento fraccional igual a cero.

El panel superior de la Fig. 4.9 muestra la correlación (3) para tres diferentes valores de  $p_T^{\text{pp}}$ : 5 GeV/ $c$  (izquierda), 10 GeV/ $c$  (centro) y 15 GeV/ $c$  (derecha). Observamos que

dentro de las incertidumbres sistemáticas y para todos los valores de  $p_T^{\text{pp}}$  explorados, el crecimiento de  $S_{\text{loss}}$  con  $(\epsilon_{\text{Bj}}\tau_0)^{3/8}L$  es lineal. Esta linealidad por primera vez es vista para todos los sistemas que comprende un amplio rango de energías; desde 62.4 GeV hasta 5020 GeV. Es importante notar que la pérdida de momento fraccional decrece yendo de  $p_T^{\text{pp}} \approx 10 \text{ GeV}/c$  a  $p_T^{\text{pp}} \approx 15 \text{ GeV}/c$  en aproximadamente 20%. Esta observación es consistente con el comportamiento esperado a muy alto  $p_T$  ( $S_{\text{loss}} \propto 1/\sqrt{p_T}$ ) en donde el factor de modificación nuclear tiende a la unidad [26].

El panel inferior de la Fig. 4.9 muestra la correlación (3) para los mismos valores de  $p_T^{\text{pp}}$  para partículas identificadas: piones, kaones y protones en colisiones Pb-Pb a la energía de  $\sqrt{s_{\text{NN}}} = 2.76 \text{ TeV}$ . Para valores de  $p_T^{\text{pp}}$  mayores a  $10 \text{ GeV}/c$  y para todas las especies de partículas, el crecimiento es lineal. Sin embargo para  $p_T^{\text{pp}} = 5 \text{ GeV}/c$  la linealidad se mantiene sólo para hadrones cargados, piones y kaones. A pesar de que el comportamiento también es lineal para protones, la pendiente es menos pronunciada. Este resultado está de acuerdo con mediciones del factor de modificación nuclear para protones con  $p_T \approx 5 \text{ GeV}/c$  donde efectos como flujo son predominantes.



# Table of contents

<b>1</b>	<b>Hadronic matter under extreme conditions</b>	<b>1</b>
1.1	Strong interactions and the QCD phase diagram . . . . .	1
1.2	Nucleus-nucleus collisions . . . . .	3
1.3	Glauber model . . . . .	6
<b>2</b>	<b>The ALICE experiment at the LHC</b>	<b>11</b>
2.1	ALICE at the LHC . . . . .	11
2.1.1	The ALICE TPC . . . . .	15
<b>3</b>	<b>Measurement of identified particle production using the ALICE TPC</b>	<b>21</b>
3.0.1	Event selection and normalization . . . . .	21
3.0.2	Track selection . . . . .	22
3.1	Low $p_T$ . . . . .	24
3.1.1	Fits to $N_\sigma$ . . . . .	24
3.1.2	Particle abundances . . . . .	26
3.1.3	Uncorrected $p_T$ spectra . . . . .	27
3.1.4	Transformation of the pseudorapidity to rapidity dependence of the yields . . . . .	29
3.1.5	Corrections . . . . .	29
3.1.6	Crosschecks . . . . .	32
3.1.7	Systematic uncertainties . . . . .	32
3.2	High $p_T$ analysis . . . . .	44
3.2.1	Additional cut on the $\varphi$ angle . . . . .	44
3.2.2	Calibration of $dE/dx$ vs $\eta$ . . . . .	45
3.2.3	$V^0$ selection and parameterizations of the Bethe-Bloch and resolution curves . . . . .	45
3.2.4	Fits to $dE/dx$ . . . . .	46
3.2.5	Particle abundances vs $p$ . . . . .	48

---

3.2.6	Particle abundances vs $p_T$ . . . . .	51
3.2.7	Uncorrected $p_T$ spectra . . . . .	52
3.2.8	Corrections . . . . .	52
3.2.9	Systematic uncertainties . . . . .	52
3.2.10	Systematic uncertainty on the extraction of the particle abundances	52
3.3	Combined results . . . . .	61
<b>4</b>	<b>Results and discussions</b>	<b>63</b>
4.1	Soft physic . . . . .	63
4.1.1	Transverse momentum spectra . . . . .	64
4.2	Hard processes . . . . .	67
4.2.1	Nuclear modification factor . . . . .	67
4.2.2	Energy density and path-length dependence of the fractional momentum loss . . . . .	68
<b>5</b>	<b>Conclusions</b>	<b>77</b>
	<b>References</b>	<b>79</b>
	<b>Appendix A The Bethe-Bloch formula</b>	<b>85</b>

# Chapter 1

## Hadronic matter under extreme conditions

This chapter starts presenting a brief overview of the underlying theory of the strong nuclear interactions. In the first section, some predictions from Lattice Quantum Chromodynamics of the phase transition from confined nuclear matter to deconfined quarks and gluons are outlined. This discussion will lead to a description of the phase diagram of QCD and eventually to a systematic description of a nucleus-nucleus collision and its different states in space-time, which for the last decades, has been the main system used to understand QCD under extreme conditions. This chapter finalizes with an overview of the Glauber model, which is used to describe nucleus-nucleus collisions as multiple nucleon-nucleon interactions and to relate observables such as the charged particle multiplicity to geometric quantities involved in nuclear interactions.

### 1.1 Strong interactions and the QCD phase diagram

Quantum Chromodynamics (QCD) is the theory of the strong nuclear interactions. The strong nuclear force is responsible to bind *quarks* ( $q$ ) to form hadrons. There are six different quarks (up ( $u$ ), down ( $d$ ), strange ( $s$ ), charm ( $c$ ), bottom ( $b$ ) and top ( $t$ )), which in addition to the electric charge, they also carry color charge (red ( $R$ ), blue ( $B$ ) and green ( $G$ )). Additionally, there are six antiquarks ( $\bar{q}$ ). Gluons are bosons having spin 1, which are the mediators of the strong interaction. Isolated quarks have never been observed experimentally, which indicates that quarks are always bound together to form color-neutral hadrons. An important characteristic of QCD is the behavior of its coupling constant as a function of the momentum transfer ( $Q$ ). Figure 1.1 shows an illustration of the effective (or running) coupling constant

( $\alpha_s$ ) as a function of  $Q$ . The interaction between quarks becomes stronger at long distances or low energies, which is a signature of the color confinement [27]. Even if a  $q - \bar{q}$  pair were forced apart, the potential energy of the tow becomes large enough that a new  $q - \bar{q}$  pair pops up from the vacuum. In this way, quarks are always confined inside hadrons. The same figure shows the other extreme of the QCD coupling constant. At high momentum transfer or short distances, the interaction becomes weak.

In order to create matter subject to extreme conditions of temperature and high energy density in a laboratory, ultra-relativistic heavy nuclei collisions can be used. Calculations from Lattice QCD (LQCD) predict a deconfinement transition between hadronic matter to a QGP (see Ref. [28] for a recent review) at an energy density of about  $1 \text{ GeV}/\text{fm}^3$ . Moreover, using the methods of LQCD, it was demonstrated that at zero baryo-chemical potential ( $\mu_B$ ), the corresponding transition linked to the restoration of chiral symmetry is of crossover type with a continuous, smooth but rapid increase of the thermodynamic quantities in a narrow region around the pseudo-critical temperature,  $T_c$  [29]. The value of the pseudo-critical temperature at vanishing  $\mu_B$  is currently calculated in LQCD to be  $(154 \pm 9) \text{ MeV}$  [30] and  $(156 \pm 9) \text{ MeV}$  [31, 32]. Thermodynamic properties of a system are most readily expressed in terms of a phase diagram in the space of thermodynamic parameters – in the case of QCD – as a  $T - \mu_B$  phase diagram. Each point on the diagram corresponds to a stable thermodynamic state, characterized by various thermodynamic functions, such as, e.g., pressure, baryon density, etc (as well as kinetic coefficients, e.g., diffusion or viscosity coefficients, or other properties of various correlation functions) [33–37]. Static thermodynamic quantities can be derived from the partition function – a Gibbs sum over eigenstates of QCD Hamiltonian. In this volume of partonic or hadronic matter, the total particle number is not being conserved at relativistic energies due to particle creation (annihilation). However, the probability distributions (partition functions) describing the particle species abundances have to respect the presence of certain, to have conserved net quantum numbers ( $i$ ). Particularly nonzero net baryon number and zero net strangeness and charm. Their global conservation is achieved by adding to the system Lagrangian a so-called Lagrange multiplier for each such quantum number. This procedure enters a ‘chemical potential’  $\mu_i$  that modifies the partition function via the term  $\exp(-\mu_i/T)$  [38]. This factor modifies the ‘punishment factor’  $\exp(-E/T)$ , where  $E$  is the total particle energy in the vacuum.

The phase diagram of QCD matter in the variables  $T$  and  $\mu_B$  is shown in Fig. 1.2. In a head-on collision of two mass 200 nuclei at  $\sqrt{s_{NN}} = 15 \text{ GeV}$ , the fireball contains equal numbers of  $q - \bar{q}$  pairs (zero net baryon number) and valence quarks. The accommodation of the latter into created hadrons thus requires a formidable redistribution task of the net baryon number, reflecting a high value of  $\mu_B$ . On the other hand, at the LHC energies

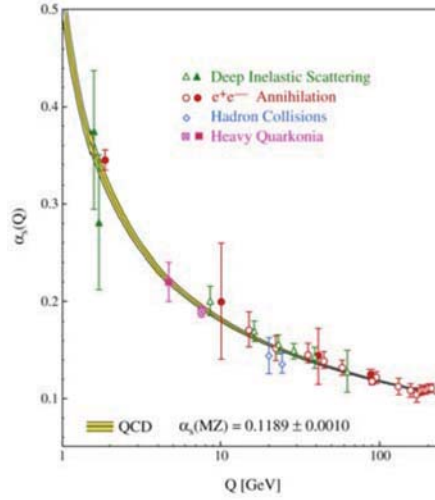


Fig. 1.1 Experimental test of the QCD coupling constant  $\alpha_s$  as a function of the momentum transfer ( $Q$ ). Figure taken from [39].

( $\sqrt{s_{NN}} = 5.02$  TeV in Pb), the initial valence quarks constitute a mere 5% fraction of the total quark density, correspondingly requiring a small value of  $\mu_B$ . In this scenario, QCD matter evolves toward hadronization at  $T \approx 170$  MeV. As matter of fact, this is the ‘situation’ in which ALICE aims to understand the transition from deconfinement to confinement of QCD matter, i. e. , at high  $T$  and low  $\mu_B$ .

## 1.2 Nucleus-nucleus collisions

The different stages of a nucleus-nucleus collision can be schematically classified as follows:

- Initial collision. Occurring during the passage time of the nuclei ( $t_{pass} = 2R/\gamma_{cm}c$ ). Figure 1.3 depicts the scenario before and after an ultrarelativistic nucleus-nucleus collision takes place. Before the collision, the two nuclei are seen from the laboratory frame as contracted objects along the beam direction. In a Pb–Pb head-on collision at the LHC energies, the energy density reached is about  $15 \text{ GeV}/\text{fm}^3$  [40], which is well above the energy density predicted for the phase transition. In order to study the system created in such collisions, the impact parameter ( $\vec{b}$ ) is used to characterize the centrality of the event (see Fig.1.3) and it is defined as the vector connecting the two centers of the colliding nuclei.



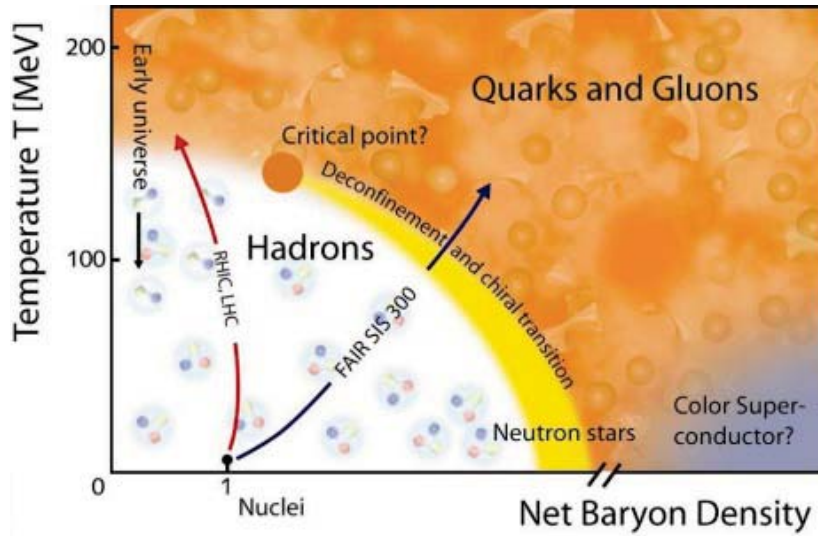


Fig. 1.2 Sketch of the QCD phase diagram in the plane  $T$  vs.  $\mu_B$ . Source: Compressed Baryonic Matter (CBM) Experiment at the Facility for Antiproton and Ion Research (FAIR), GSI, Darmstadt, Germany.

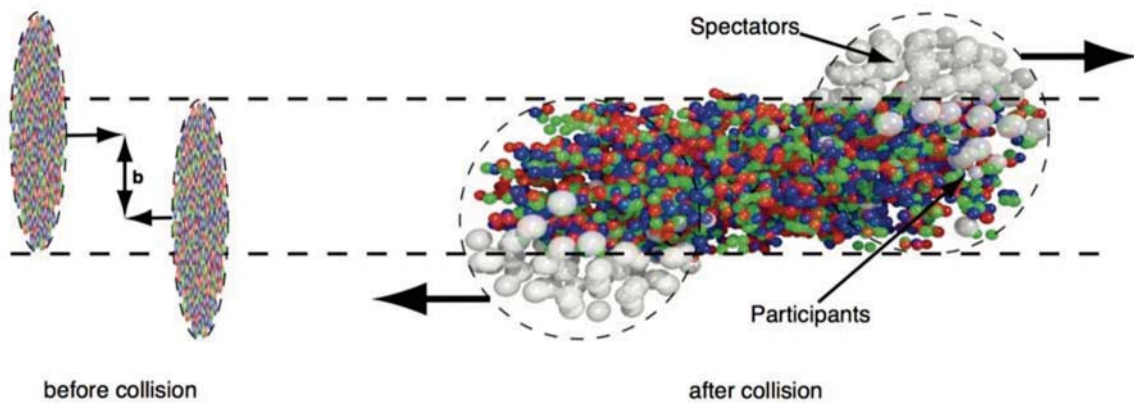


Fig. 1.3 (Left) Two nuclei before colliding. The centrality of the collision is characterized by the impact parameter vector ( $\vec{b}$ ). (Right) The spectators continue unaffected while in the participant region, the formation of the QGP takes place. Figure was taken from [41].

- Expansion and cooling (in a deconfined state). The characterization of the deconfined system (commonly referred as the ‘fireball’) is rather challenging as all the measurements are performed on final-state particles and direct measurements of the deconfined system remain inaccessible. However, assuming that the local thermalization is reached at a characteristic proper time  $\tau_0$  that produces the initial conditions of the system, relativistic hydrodynamic provides a description of the space-time evolution of the hot/dense matter without going into details about any microscopic model, at

all the stages of the expansion of matter, from possibly, the quark-gluon plasma to hadronization transition and freeze-out [42].

- Chemical freeze-out. Figure 1.4 shows a fit to the measured hadrons using the thermal model [43], which is a three-parameter model: temperature ( $T$ ), baryo-chemical potential ( $\mu_B$ ) and a volume ( $V$ ). This model mainly describes the chemical freeze-out in which all the inelastic processes have ceased and presumably is a quasi-instantaneous stage [44]. This model provides a phenomenological link to the QCD phase diagram. This phenomenological link is represented in the right-hand-side plot of Fig. 1.4. Each point in the plot represents a fit to hadron yields from Au–Au or Pb–Pb at a given collision energy. All the tested models agree in the behavior of data. Remarkably,  $T$  increases with increasing energy (decreasing  $\mu_B$ ) from about 50 MeV to about 160 MeV. Furthermore,  $T$  saturates for  $\mu_B \lesssim 300$  MeV. This saturation of  $T$  led to the connection to the QCD phase boundary, via the conjecture that the chemical freeze-out temperature can be the hadronization temperature [45]. The thermodynamic at the freeze-out (for high energies, corresponding to the ‘limiting temperature’) yield  $T_{lim} = 159$  MeV, pressure  $P \approx 60$  MeV/fm<sup>3</sup> and an energy density  $\varepsilon \approx 130$  MeV/fm<sup>3</sup>.

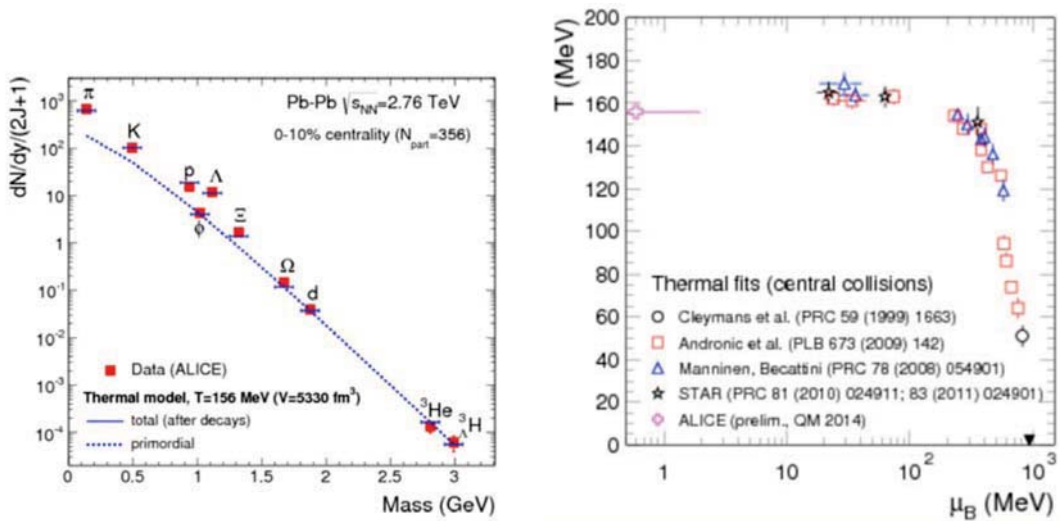
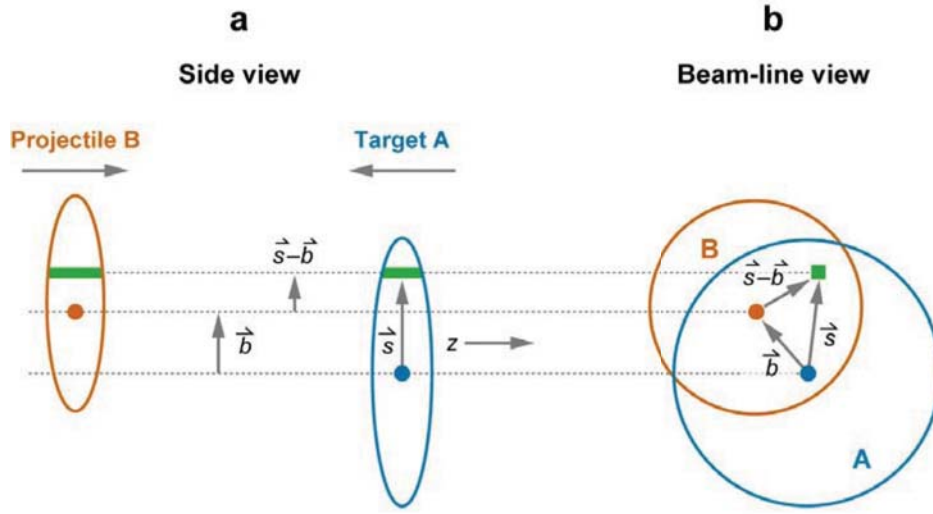


Fig. 1.4 (Left) Measured hadron abundances divided by the spin degeneracy factor ( $2J+1$ ) in comparison with thermal model calculations for the best fit to data [46] in central Pb–Pb collisions at the LHC. (Right) The phase diagram of strongly interacting matter with the points representing the thermal fits of hadron yields at various collision energies. For the LHC,  $\mu_B = 0$  is the outcome of the fit, 0.6 MeV is used here for the sake of proper representation with the logarithmic scale. The down-pointing triangle indicates ground state nuclear matter (atomic nuclei)[44]. Figures taken from [44].

- Kinetic freeze-out. At this stage hadrons decouple from the system and their transverse momentum distributions are fixed. Hadrons undergo collective phenomena [47, 48], which is a relevant signature in nucleus-nucleus collisions. Particularly, in central collisions, radial-flow [9] is a relevant mass dependent effect, which is quantified by fitting the transverse momentum spectra with a Blast-Wave model [14]. Moreover, this model yields the average temperature at the kinetic freeze-out in which elastic interactions cease. The fit-parameters extracted from this model are the temperature at the kinetic freeze-out ( $T_{\text{kin}}$ ), the average transverse velocity ( $\langle\beta_T\rangle$ ) and the exponent of the velocity profile ( $n$ ). In Chapter 4, the correlation  $T_{\text{kin}}$  vs.  $\langle\beta_T\rangle$  for different multiplicity events is discussed for Pb–Pb collisions at  $\sqrt{s_{\text{NN}}} = 5.02$  TeV. At this point, it is worth to mention that further studies on radial-flow-like patterns can be made using the transverse momentum spectra of identified charged particles. Moreover, the hadron transverse momentum spectra above 10 GeV/ $c$  can be used as proxies for jets to try to understand mechanisms for parton energy loss as will be discussed in Chapter 4.

### 1.3 Glauber model

The Glauber model, pioneered by Roy Glauber [49, 50] was developed to address the problem of multiple scattering with composite particles. This is a semi-classical model, which treats nucleus-nucleus collisions as multiple nucleon-nucleon interactions. At sufficiently high energies, nucleons are assumed to carry sufficient momentum to travel in straight lines and are not deflected when nuclei pass through each other. It is also assumed that nucleons move independently in the nucleus and that the size of the nucleus is larger compared to the extent of the nucleon-nucleon interaction. Figure 1.5 depicts the collision of two nuclei, Target A and Projectile B collide with impact parameter  $\vec{b}$ . From the geometry of the collision, two flux tubes are defined. The center of the first tube coincides with the center of A and has a radius equal to the magnitude of  $\mathbf{s}$ , while the second tube flux is located at a distance  $\mathbf{s} - \mathbf{b}$  from the center of B. The probability per unit transverse area for a given nucleon to be found in the target A tube flux is given by  $\hat{T}_A(\vec{s}) = \int dz_A \rho_A(z, \vec{s}_A)$ , where  $\rho_A(z, \vec{s}_A)$  is the probability per unit volume, normalized to unity, to locate a certain nucleon in the  $(z, \vec{s}_A)$  position. An analogous expression is given for the projectile B tube flux. For heavy nucleus, the Wood-Saxon parameterization is a good approximation for  $\rho_A$ :




 Miller ML, et al. 2007.  
Annu. Rev. Nucl. Part. Sci. 57:205–43

Fig. 1.5 Schematic representation of the optical Glauber model geometry, with transverse (*a*) and longitudinal (*b*) views. Figure was taken from [50].

$$\rho_A(r) = \rho_0 \frac{1 + w(r/R)^2}{1 + \exp\left(\frac{r-R}{a}\right)} \quad (1.1)$$

where  $\rho_0$  is the nucleon density at the center and is determined by the overall normalization condition  $\int \rho(r) d^3r = A$ ,  $R$  corresponds to the nuclear radius ( $= 6.62 \pm 0.06$  fm in  $^{208}\text{Pb}$ ),  $a$  is associated to the skin depth, which indicates how rapidly the nuclear density fades out near the edge of the nucleus and  $w$  ( $= 0$  for Pb) characterizes deviations from a spherical shape. The product  $\hat{T}_A(\vec{s}) \hat{T}_B(\vec{s} - \vec{b}) d^2s$  then gives the probability per unit area of nucleons being located in the respective overlapping target and projectile flux tubes of differential area  $d^2s$ . Equation 1.2 then defines the thickness function

$$\hat{T}_{AB}(\vec{b}) = \int d^2s \hat{T}_A(\vec{s}) \hat{T}_B(\vec{s} - \vec{b}) \quad (1.2)$$

Notice that Eq. 1.2 has units of inverse area. The thickness function is interpreted as the effective overlap area for which a nucleon in A can interact with a certain nucleon in B. The probability for this interaction to occur is given by  $\hat{T}_{AB} \sigma_{\text{inel}}^{\text{NN}}$ , where  $\sigma_{\text{inel}}^{\text{NN}}$  is the inelastic nucleon-nucleon cross section. As the inelastic nucleon-nucleon cross section involves processes with low momentum transfer, it cannot be calculated from pQCD. Thus, in Glauber

calculations, the measured  $\sigma_{\text{inel}}^{\text{NN}}$  is used as an input and provides the only non-trivial energy dependence to the model.

Once, the probability for the nucleon-nucleon interaction is known, the probability of  $n$  interactions between nuclei A (with  $A$  nucleons) and B (with  $B$  nucleons) is given as a binomial distribution

$$P(n, \vec{b}) = \binom{AB}{n} \left[ \hat{T}_{\text{AB}}(\vec{b}) \sigma_{\text{inel}}^{\text{NN}} \right]^n \left[ 1 - \hat{T}_{\text{AB}}(\vec{b}) \sigma_{\text{inel}}^{\text{NN}} \right]^{AB-n} \quad (1.3)$$

where the first term represents  $n$  interaction out of  $AB$  possible nucleon-nucleon interactions, the second term yields the probability for exactly  $n$  collisions, while the third term represents the  $AB - n$  missing interactions.

The Glauber model is useful for calculating initial ‘geometric’ quantities such as the mean number of participating nucleons ( $\langle N_{\text{part}} \rangle$ ) and the mean number of binary nucleon-nucleon collisions ( $\langle N_{\text{coll}} \rangle$ ). The total number of nucleon-nucleon collisions is given by [50]

$$N_{\text{coll}}(\vec{b}) = \sum_{n=1}^{AB} n P(n, \vec{b}) = AB \hat{T}_{\text{AB}}(\vec{b}) \sigma_{\text{inel}}^{\text{NN}} \quad (1.4)$$

The number of interacting nucleons from target A and projectile B are known as the participating nucleons and it is given by [50]

$$N_{\text{part}}(\vec{b}) = A \int \hat{T}_{\text{A}}(\vec{s}) \left\{ 1 - \left[ 1 - \hat{T}_{\text{B}}(\vec{s} - \vec{b}) \sigma_{\text{inel}}^{\text{NN}} \right]^B \right\} d^2s + \quad (1.5)$$

$$B \int \hat{T}_{\text{B}}(\vec{s} - \vec{b}) \left\{ 1 - \left[ 1 - \hat{T}_{\text{A}}(\vec{s}) \sigma_{\text{inel}}^{\text{NN}} \right]^A \right\} d^2s \quad (1.6)$$

where the integral over the bracketed terms gives the respective inelastic cross sections for nucleon-nucleon collisions.

### Relating the Glauber model to experimental data

The values of  $N_{\text{part}}$  and  $N_{\text{coll}}$  cannot be measured directly in the experiment. However, the mean values of such quantities can be extracted for classes of measured events via a mapping procedure, i. e. , a measured distribution (e.g.,  $dN_{\text{evt}}/d\eta$ ) is mapped to the corresponding distribution obtained from Glauber calculations. The mapping is done by defining centrality

classes in both, the measured and calculated distributions and then connecting the mean values from the same centrality class in the two distributions. The basic assumption when defining centrality classes is that the impact parameter is monotonically related to the particle multiplicity. For large  $b$  (peripheral collisions), it is expected low multiplicity at midrapidity and a large number of spectator nucleons at forward rapidity whereas for small impact parameter (central collisions), it is expected large multiplicity at midrapidity and less amount of spectator nucleons at forward rapidity. Then, the particle multiplicity ( $dN_{\text{evt}}/dN_{\text{ch}}$ ) per-event in an ensemble of events is measured. Once the total integral of the multiplicity distribution is computed, centrality classes are defined by binning the distribution based upon the fraction of the total integral (see Fig. 1.6). The same procedure is applied to Monte Carlo Glauber multiplicity distributions. For each centrality class, the mean value of Glauber quantities (e.g.,  $N_{\text{part}}$ ) for the Monte Carlo events within the bin (e.g., 5-10%) is calculated. This straightforward procedure conveys potential complications due to event selection, uncertainty in the total measured cross section, fluctuations in both, the measured and calculated distributions and finite kinematic acceptance. Figure 1.6 also shows, that the centrality classes are characterized by percentiles of the total cross section.

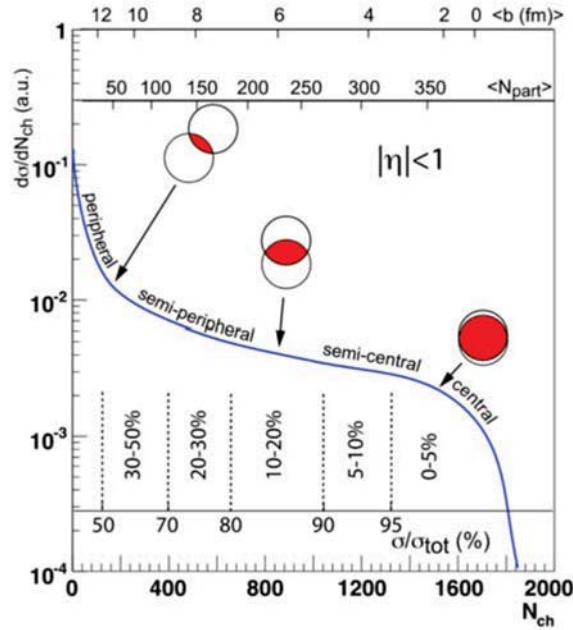


Fig. 1.6 Centrality determination. The figure was taken from [50].



# Chapter 2

## The ALICE experiment at the LHC

In this chapter, an overview of the ALICE experiment is presented. Its main purpose is the study of matter under extreme conditions of temperature and pressure, i. e. the Quark-Gluon plasma in heavy-ion collisions. The most challenging task that a heavy ion experiment faces is the numerous particle production in central nucleus-nucleus collisions, which could be up to three orders of magnitude larger than in typical proton-proton collisions at the same energy. As many phenomena depend either on the particle mass or the particle specie, the precise identification and measurement of the particle production over a wide momentum range is essentially important. The current chapter outlines the unique capabilities to perform particle identification inside the ALICE experiment. The particle identification techniques include energy loss in silicon and gas detectors, Cherenkov and transition radiation, time-of-flight, electromagnetic calorimeters, as well as topological decay reconstruction.

### 2.1 ALICE at the LHC

ALICE (A Large Ion Collider) [7, 8] is one of the four major experiments at the CERN Large Hadron Collider (LHC). In contrast to other experiments at the LHC, ALICE is committed to the study of nuclear matter under extreme conditions of temperature and density.

ALICE has an overall length of 25 m, a diameter of 10 m, and a weight of about 10000 t. It consists of a system of central barrel detectors dedicated to the measurement of event-by-event hadrons, electrons, photons in the midrapidity region ( $|y| < 0.5$ ) and, a forward spectrometer to measure muons. The central barrel, which covers polar angles from  $45^\circ$  to  $135^\circ$  over the full azimuth, is embedded in the L3 solenoidal providing a magnetic field in the interval  $0.2\text{T} \leq B \leq 0.5\text{T}$  (see Fig. 2.1).



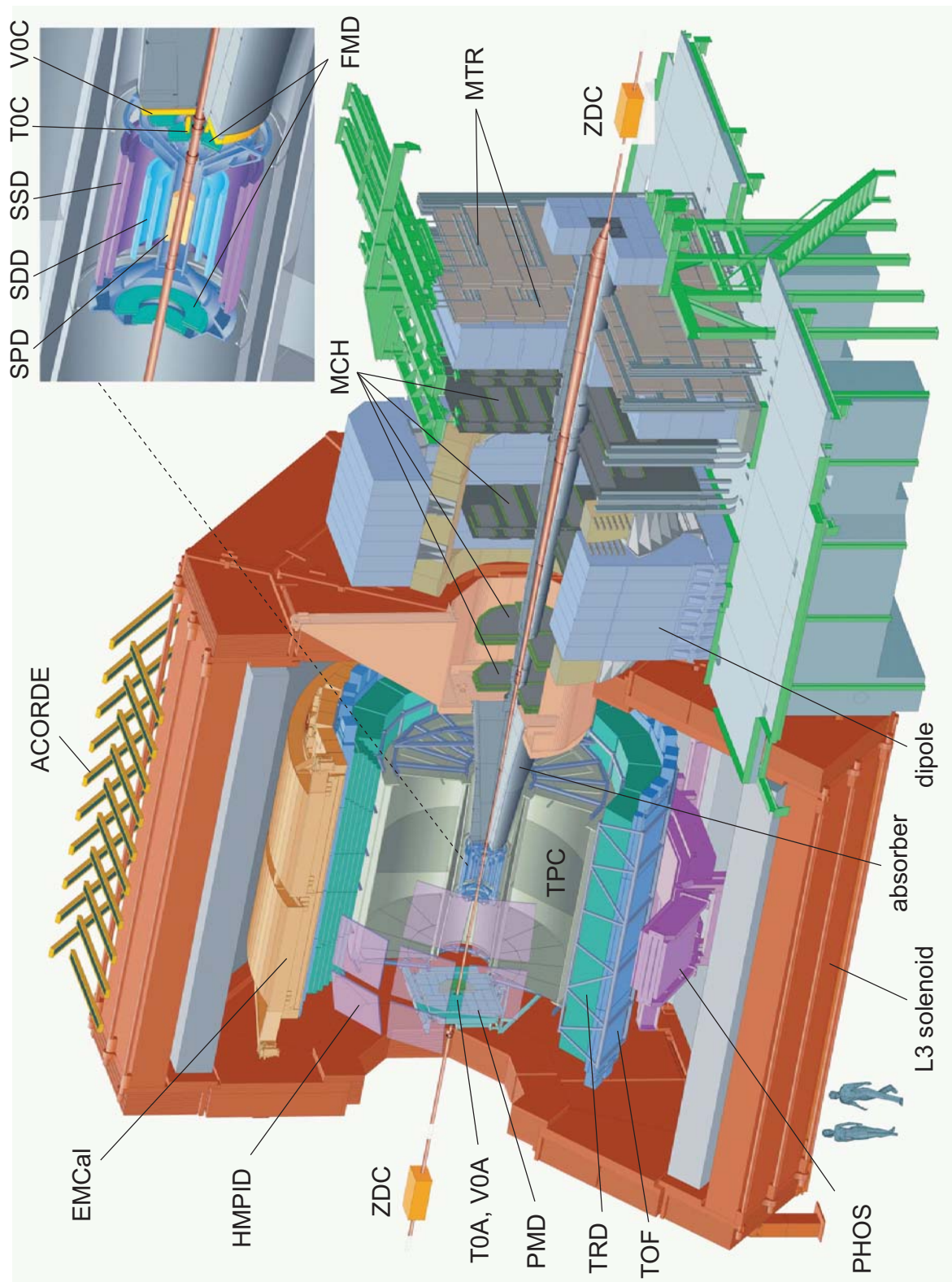


Fig. 2.1 The ALICE apparatus at the CERN LHC. The central barrel embraces the ITS, TOF, TPC, and, HMPID subdetectors used for tracking and particle identification.

### The VZERO system

A detailed explanation of the VZERO system can be found in [51, 52]. The VZERO system is composed of two arrays, VZERO-A and VZERO-C, which cover the pseudorapidity intervals  $2.8 < \eta < 5.1$  and  $-3.7 < \eta < -1.7$  for collisions at the nominal interaction point ( $z = 0$ ), respectively. Each of the VZERO arrays is segmented in four rings in the radial direction, and each ring is divided in eight sections in the azimuthal direction. Both disks are plastic scintillator tiles read out by optical fibres. One of the basic tasks of the VZERO system is to provide the ALICE experiment with a minimum bias (MB) trigger for both, pp and Pb–Pb collisions and for centrality based triggers in Pb–Pb mode.

### Multiplicity and centrality measurements

The VZERO system is to provide measurements of the charged particle multiplicity based on the energy deposited in the scintillators. Using detailed simulations of the VZERO apparatus, a relation between the charge collected inside a VZERO ring and the number of primary charged particles in the corresponding pseudorapidity range is extracted. Hence, it is possible to obtain the pseudorapidity charged particle multiplicity,  $dN_{\text{ch}}/d\eta$ , in eight pseudorapidity bins, corresponding to the coverage of the different rings of the VZERO. Further details on the centrality classes estimation in Pb–Pb collisions at  $\sqrt{s_{\text{NN}}} = 2.76$  TeV can be found in [53].

In the analysis covered by this thesis, MB pp events were analyzed and the Pb–Pb events were divided into ten centrality classes, they are reported below

$$\begin{array}{cccccc} [0 - 5]\% & [5 - 10]\% & [10 - 20]\% & [20 - 30]\% & [30 - 40]\% & \\ [40 - 50]\% & [50 - 60]\% & [60 - 70]\% & [70 - 80]\% & [80 - 90]\% & \end{array}$$

### Inner Tracker System (ITS)

The Inner Tracking System (ITS) [7] consists of six cylindrical layers of silicon detectors, located at radii,  $r = 4, 7, 15, 24, 39,$  and  $44$  cm, respectively. It covers the pseudorapidity interval  $|\eta| < 0.9$ . The determination of both, the primary and secondary vertices of decaying particles is one of the basic functions of the ITS. For the two innermost layers which have a high particle density, up to 80 particles per  $\text{cm}^2$ , Silicon Pixel Detectors (SPD) are used. The two following layers are Silicon Drift Detectors (SDD). The two outer most layers in which the track densities are below 1 particle per  $\text{cm}^2$  are equipped with double-sided Silicon micro-Strip Detectors (SSD). The SSD are meant to satisfy track-matching with the Time

Projection Chamber. Furthermore, as a stand-alone detector, the ITS can perform particle identification (PID) in the  $1/\beta^2$  region of the Bethe-Bloch curve (see App. A) by means of the specific energy loss  $dE/dx$ . Thus, the ITS provides a reliable  $dE/dx$  resolution in the low-momentum region ( $p < 1$  GeV/ $c$ ). The resolution is about 10–12 %. The upper-left panel of Fig. 2.2 shows the correlation between  $dE/dx$  and  $p$ . Particle identification is done in a track-by-track basis. The interval of transverse momentum for identification are reported in Tabs. 3.4, 3.5.

### Time Of Flight (TOF)

The Time-Of-Flight (TOF) detector [7] covers a cylindrical surface in the pseudorapidity region  $|\eta| < 0.9$  and full coverage of the azimuthal angle ( $\varphi$ ). It is Multi-gap Resistive Plate Chamber (MRPC) type detector at a radial distance of 3.7 m from the beam line. Due to its excellent time resolution (tens of pico seconds), it can be used for time-of-flight measurements. An illustrative example of the capabilities to perform particle identification is shown. For a known momentum ( $p$ ), track-length ( $l$ ) ( $p$  and  $l$  measured with the tracking detectors) and the measured time-of-flight  $t^{TOF}$ , the mass ( $m$ ) of a particle is given by:

$$m = \frac{p}{\beta\gamma} = p \sqrt{\frac{(ct^{TOF})^2}{l^2} - 1} \quad (2.1)$$

The overall time-of-flight resolution,  $\sigma = \sqrt{\sigma_{TOF}^2 + \sigma_{reco}^2}$  includes both the time resolution of the TOF system,  $\sigma_{TOF}$ , and the uncertainty  $\sigma_{reco}$  related to the reconstruction of the momentum and of the track length. The latter uncertainty, which depends on the track momentum and on the particle type, is, on average,  $\approx 30$  ps. In practice the measurement provided by the TOF detector is  $\beta (= \frac{v}{c})$  vs.  $p$  as is shown in Fig. 2.2

### High-Momentum Particle Identification Detector (HMPID)

The High-Momentum Particle Identification Detector (HMPID) [7] is devoted to the inclusive measurement of high  $p_T$  identified hadrons. It is a single-arm array with an acceptance of 5% of the overall central barrel phase space. The HMPID is based on proximity-focusing Ring Imaging Cherenkov (RICH) counters. Photon detection is provided by proportional multiwire chambers coupled to pad-segmented CsI photocathode. Particle identification is achieved by means of the measured Cherenkov angle,  $\theta_{ch}$ . This is given by

$$\theta_{\text{ch}} = \arccos \frac{\sqrt{p^2 + m^2}}{np} \quad (2.2)$$

where  $n$  is the refractive index of the radiator used (liquid  $C_6F_{14}$  with  $n = 1.29$  at  $E_{ph} = 6.675$  eV and temperature  $T = 20$  °C ),  $p$  and  $m$  are the momentum and mass of the given particle provided by the tracking detectors, respectively. The correlation between the  $\theta_{\text{ch}}$  vs.  $p$  is depicted in the bottom-right panel of Fig. 2.2

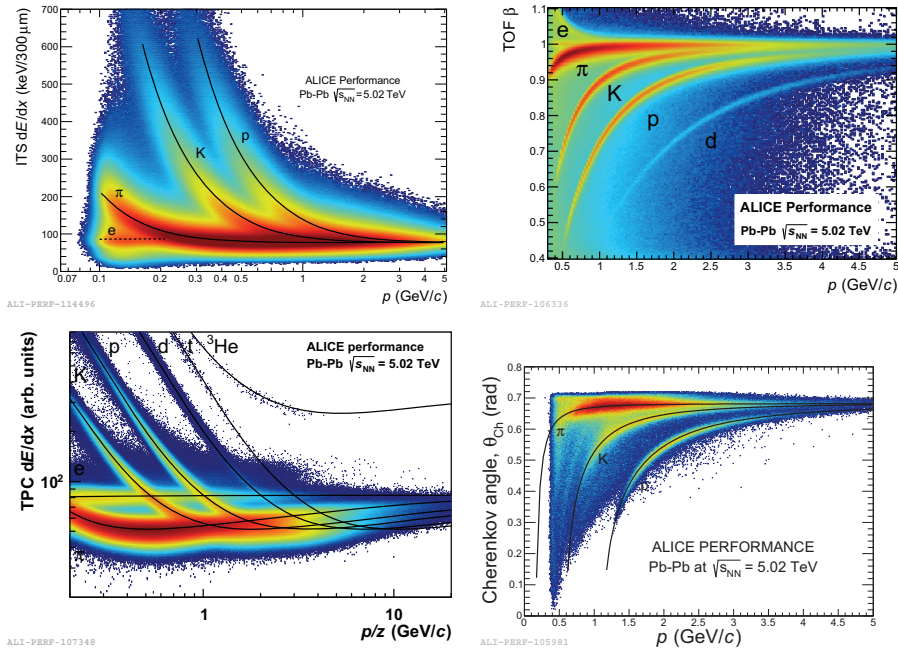


Fig. 2.2 Performance of the different ALICE detectors. ITS (upper-left corner), TOF (upper-right corner), TPC (bottom-left corner), and HMPID (bottom-right corner).

### 2.1.1 The ALICE TPC

The Time Projection Chamber (TPC) [7, 8] is the main device for tracking and particle identification in ALICE. It is a cylindrical drift-chamber with a length of 5100 mm and diameter of 5560 mm. It comprises two parts: the field cage and the read-out plates (see Fig. 2.3). The field cage is to provide a highly uniform electrostatic electric field perpendicular to the read-out chambers in a high-purity gas volume. The gas mixture used in Run1 was changed from Ne(%90):CO<sub>2</sub>(%10) to Ar(90%):CO<sub>2</sub>(%10) in Run2. This allows for a more stable response to the high particle fluxes generated during p–Pb and Pb–Pb running without

	Pad size [mm <sup>2</sup> ]	number of rows	Number of pads
Inner chamber ( $84.1 < r < 132.1$ cm)	$4 \times 7.5$	64	5732
Outer chamber ( $134.6 < r < 198.6$ cm)	$6 \times 10$	64	6038
Outer chamber ( $198.6 < r < 246.6$ cm)	$6 \times 15$	32	4072
TPC total		160	570312

Table 2.1 ALICE TPC read-out pads. Data taken from [7].

significant degradation of momentum resolution at the lowest transverse momenta.

The field is divided into two volumes, back-to-back in a common gas volume, with a common high-voltage (HV) electrode located at the axial center of the cylinder. The central HV electrode and two opposite axial potential degraders provide uniform drift fields of up to 400 V/cm. When charged particles ionize the gas, primary electrons are drifted towards the end-plates. Although, the amount of primary electrons is not plentiful, the signal is magnified by avalanche creation in the vicinity of the anode wires. Parallel to the anode grid, a cathode grid collects the ions produce in the amplification avalanche.

The ALICE read-out chambers are multiwire proportional chambers (MWPC). They are segmented in 18 trapezoidal sectors, each covering 20° in azimuth (see Fig. 2.3). The read-out plane is segmented in inner (IROC) and outer read-out chambers (OROC). The overall pad layout of the inner and outer chambers is shown in Fig. 2.3 and summarized in Tab. 2.1. Each inner chamber has a total of 5732 pads and each pad has a size of  $4 \times 7.5$  mm<sup>2</sup>. The number of pads in each of the outer chambers is of 10110, each pad has a size of  $6 \times 10$  mm<sup>2</sup> (for  $r < 198.6$  cm) and  $6 \times 15$  mm<sup>2</sup> (for  $r > 198$  cm).

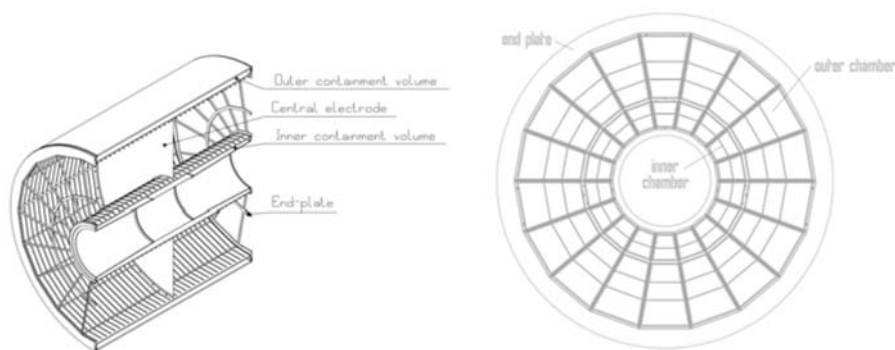


Fig. 2.3 (Left) Assembled field cage without read-out chambers. (Right) Segmentation of the readout chambers.

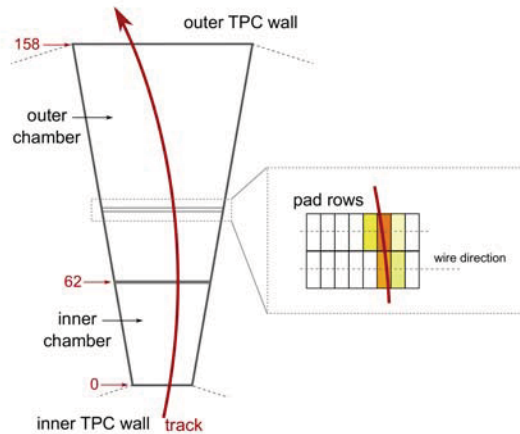


Fig. 2.4 ALICE TPC read-out chambers and pad rows. Figure taken from [54].

### Vertex and track reconstruction

- *Vertex reconstruction.* The  $z$  coordinate (along the beam line) of the interaction point is distributed in a range of several centimeters, while the beam spot size in the transverse plane varies between ten and hundred microns. Two algorithms are employed to reconstruct the primary vertex position [55]. The first one uses tracklets (line segments built from correlations between pairs of clusters in the two layers of the SPD within a small azimuthal window of 0.01 rad). The vertex reconstruction efficiency when the tracklet multiplicity is above 8, approaches 100%. The second algorithm is based on the straight line approximation of fully reconstructed tracks in the vicinity of the vertex. With a tracklet multiplicity of 3 and taking into account information of the beam spot position and size an efficiency of 80% is achieved, otherwise, 100% is approached at higher multiplicity.
- *Track reconstruction.* The reconstruction of tracks and cluster finding in the ITS, TPC, and TRD detectors share a common convention on the coordinate system used. The position of both, clusters and tracks in three-dimensional space are expressed in some local coordinate system associated to a given sub-detector and it is defined as follows [7, 8]
  - It is a right-handed cartesian coordinate system
  - Its origin and the  $z$  axis coincide with those of the global ALICE coordinate system
  - The  $x$  axis is perpendicular to the sub-detector's 'sensitive plane' (TPC pad row)

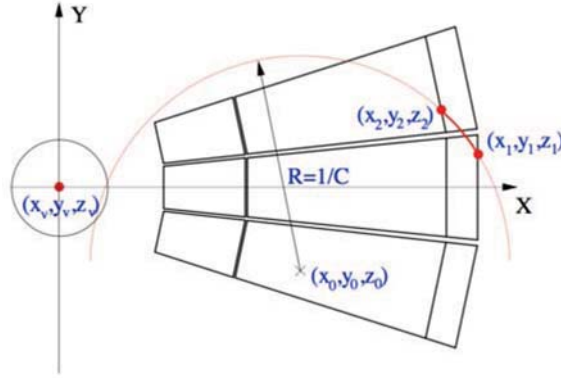


Fig. 2.5 Local TPC coordinate system and track parameters. Figure taken from [8].

When a charged particle traverses the gas volume, a signal is induced in a given pad-row. If the charge investigated in a  $5 \times 5$  bins in  $z$  (drift time) and  $y$  (pad) exceeds a threshold and fulfill a quality criteria, respectively, it is called a *cluster*. Before track reconstruction, two-dimensional clusters are found in pad-row-time planes [7]. This action is done pad-row by pad-row. Then, the reconstruction of the positions of space points take place. These space points are interpreted as the crossing points between the tracks and the centers of the pad rows. The track of a charged particle traveling bends due to the action of the magnetic field. Track finding is based on the Kalman-filtering approach [7, 56]. It takes into account variations of the kinematic variables of the particle (due to energy loss and multiple scattering) to parameterize a continuous track trajectory. Using the local coordinate system (see Fig. 2.5), the track state vector used in the Kalman-filter is given by,  $X^T \equiv (y, z, C, \tan(\lambda), \eta)$ , where  $C$  is the curvature of the track projection on the pad plane,  $\lambda$  is the angle between the track and the pad plane, and,  $\eta \equiv Cx_0$ . This procedure is repeated as many times as the track is propagated from one pad row to another. As a matter of fact, the Kalman-filter track finding relies on the determination of good initial approximations of the track parameters and their covariance matrix (so call track *seeds*). Two different seed finding approaches are used: seed finding with the vertex constraint and without any constraint. The former approach commences by finding pairs of points at the  $i$  pad-row (outer) and a pad-row  $j$ , both closer at the interaction points ( $i - j \approx 20$ ). For each point at the outer pad-row, points at the inner pad row are checked only within a given window in the  $(x, y)$  plane, defined by some  $p_T$  cut-off, and a given window in the  $z$  direction defined by the requirement of pointing to the primary vertex. When a reasonable pair of clusters is found, parameters of a helix going through these points and the primary vertex are calculated, and an occurrence of a cluster near the crossing point of this

helix and a ‘middle’ pad row  $k = j + (i - j)/2$  is checked. If such a cluster is found, the parameters of this helix are taken as an initial approximation of the parameters of the potential track. Using the calculated helix parameters and their covariance matrix, the Kalman-filter is started. If at least half of the possible points between the initial ones are successfully associated with this track candidate, it is saved as a seed.

### **$dE/dx$ measurement**

It would be reasonable to use the overall charge deposited in the clusters. However, this is less sensitive for overlapping clusters. For each cluster associated to a track, the amplitude at the local maximum is divided by the length of the corresponding track segment, and then the overall  $dE/dx$  value is estimated using the truncated mean method. Tracks which share clusters are not used for the  $dE/dx$  calculation. In Pb–Pb collisions a  $dE/dx$  resolution around the value of 6.5% is achieved while in pp collisions where almost all the clusters are associated to tracks, it is about 5.5%. The bottom-left panel of Fig. 2.2 shows the correlation between  $dE/dx$  and  $p$ . Further details on the evaluation of the  $dE/dx$  in the TPC are found in [7, 8].





# Chapter 3

## Measurement of identified particle production using the ALICE TPC

This chapter has to do with the analysis to extract the particle yields of ‘primary’ charged pions, kaons, and (anti)protons using the ALICE TPC. Primary charged particles are defined as prompt particles produced in the collision, including decay products, except those from weak decays of strange particles. Firstly, the assortments of data, event, and track selection are presented. The track selection is a general selection in the sense that it is applied to both, low and high  $p_T$  tracks.

Firstly, the low  $p_T$  ( $p_T < 1 \text{ GeV}/c$ ) analysis (see Sec. 3.1) is presented. The characteristic behavior of the  $dE/dx$  in this region has the functional form of  $1/\beta^2$  (see Fig. 2.2 and App. A). In this region, particle identification (PID) is doable for the  $p_T$  bins where the signal among the different species is well separated.

The analysis of PID includes also the relativistic rise region ( $3 < p_T < 20 \text{ GeV}/c$ ) (see Sec. 3.2). In this region, the behavior to the  $\langle dE/dx \rangle$  is proportional to  $\log(\beta\gamma)$  ( $3 < \beta\gamma < 1000$ ). The parameterization of the  $\langle dE/dx \rangle$  as a function of  $p$  by means of a two-dimensional fit to the correlation,  $dE/dx$  vs.  $p$ , in the relativistic rise region will allow to use a four-Gaussian function to describe the relative abundances of pions, kaons, protons and electrons.

### 3.0.1 Event selection and normalization

- Events whose vertex  $z$  coordinate is within  $\pm 10 \text{ cm}$  ( $|V_z| < 10 \text{ cm}$ ) from the interaction point (IP) were accepted.
- $Z_{SPD}$  (vertex coordinate reconstructed with the SPD) reconstruction resolution better than  $0.25 \text{ cm}$  and dispersion less than  $0.04$  were required.

- $|Z_{track} - Z_{SPD}| < 0.5$  cm, where  $Z_{track}$  is reconstructed using the information from global tracks (tracks reconstructed with the ITS and TPC detectors).
- *Pile-up events*: events with more than one primary vertex reconstructed were rejected.
- *Background events*: events coming from beam-gas were rejected. Background events come from interactions between the beams and the residual gas within the beam pipe and from interactions between the beam halo and various components of the accelerator such as collimators. Measuring the time-of-flight of particles detected by each VZERO array, particles coming from collisions and particles coming from beam-gas background can be distinguished.

The  $p_T$  spectra were normalized by the  $N_{ev}$  (number of events) as follows.

- In the Pb–Pb analysis,  $N_{ev}$  is defined as the number of events that pass the cut on the physics selection ( $N_{Phys,slec}$ , including the cut on background and pileup) and satisfying,  $|V_z| < 10$  cm.

$$N_{ev} = N_{vtx < 10 \text{ cm}} \quad (3.1)$$

- In the pp analysis,  $N_{ev}$  is defined as the number of events that pass the cut on the physics selection ( $N_{Phys,slec}$ ) multiplied by  $N_{vtx < 10 \text{ cm}}$  and divided by the number of events having a reconstructed vertex  $N_{rec-vtx}$ .

$$N_{ev} = \frac{N_{Phys,slec} \times N_{vtx < 10 \text{ cm}}}{N_{rec-vtx}} \quad (3.2)$$

### 3.0.2 Track selection

This subsection lists the cuts applied to the tracks, commonly it is referred as the track selection. A brief definition of each cut is given as well as the value used in each cut.

- *The Number of Crossed Rows* is defined as the ratio of number of clusters associated to a track to the number of pad-rows crossed by this track. For the case of pp collisions this distribution peaks around 100. For high-track-multiplicity events (e.g., central Pb–Pb collisions), tracks start losing their clusters, however, this ratio is still rather high, close to 80 [8]. The default value was set to 70.

– SetMinNCrossedRowsTPC(70)

- 
- *Findable clusters* are defined as the number of geometrically possible clusters assigned to a track [8]. In this analysis the threshold value for the crossed-rows to findable clusters ratio was set to 0.8.
    - SetMinRatioCrossedRowsOverFindableClustersTPC(0.8)
  - *The geometrical cut* imposes the following conditions on tracks to be accepted
    - Tracks are required to have a length ( $L$ ) larger than the  $p_T$  dependent cut;  $L = 130 - \frac{1}{p_T^{1.5}}$ .
    - Tracks within 3 cm from the sector edges are excluded.
    - Track lengths expressed in the number of crossed TPC read-out pad rows has to be larger than  $0.85 \times L$  while track lengths expressed in the number of TPC clusters (one cluster per pad row) have to be larger than  $0.7 \times L$ .
    - SetCutGeoNcrNcl(2., 130., 1.5, 0.0, 0.0)
  - *Maximum  $\chi^2$  per cluster.* The Kalman filter minimizes the track-to-cluster residuals in pad and drift direction [7]. The  $\chi^2$  per cluster describes the performance of the Kalman filter. For track reconstruction in the TPC, a threshold of 4 in the value of  $\chi^2$  per cluster is imposed.
    - SetMaxChi2PerClusterTPC(4)
  - *Maximum  $\chi^2$  per cluster.* For track reconstruction in the ITS, a threshold of 36 in the value of  $\chi^2$  per cluster is imposed.
    - SetMaxChi2PerClusterITS(36)
  - Kink-daughter particles were rejected.
    - SetAcceptKinkDaughters(kFALSE)
  - Matching between track finding when reconstructing from the inner radius layer to the outer radius layer of the TPC and backwards was required.
    - SetRequireTPCRefit(kTRUE)
  - Matching between track finding when reconstructing from the inner layer to the outer layer of the ITS and backwards.
    - SetRequireITSRefit(kTRUE)

- The distance of closest approach in the transverse plane ( $DCA_{xy}$ ) is defined as the distance between tracks projected in the transverse plane ( $xy$ ) to the primary vertex in the beam direction ( $z$ ). Tracks with a distance larger than the  $p_T$ -dependent cut  $0.0105 + \frac{0.0350}{p_T^{1.1}}$  were rejected.
  - `SetMaxDCAToVertexXYPtDep("0.0105 + \frac{0.0350}{p_T^{1.1}}")`

## Data sets

The Pb–Pb and pp data sample at  $\sqrt{s_{NN}} = 5.02$  TeV was collected with the ALICE detector during the LHC Run2 in 2015 data taking. The measurement of the  $p_T$  spectra was accomplished using about 9.5 and 120 million of events in Pb-Pb and pp collisions, respectively. The events were recorded at low interaction rate.

The Pb–Pb data set correspond to the period LHC15o pass4. A total of 13 runs were used: 244917, 244918, 244975, 244980, 244982, 244983, 245061, 245064, 245066, 245068, 246390, 246391, 246392.

The data set used in the pp analysis corresponds to the period LHC15n pass3. A total of 25 runs were used: 244628, 244627, 244619, 244618, 244617, 244542, 244540, 244531, 244484, 244483, 244482, 244481, 244480, 244456, 244453, 244421, 244416, 244377, 244364, 244359, 244355, 244351, 244343, 244340.

## Trigger selection

For selecting MB pp events the trigger, `AliVEvent::kINT7` was used. This selection requires a hit in both, VZERO-A and VZERO-C detectors. The event is accepted if the trigger conditions are fulfilled.

## 3.1 Low $p_T$

The interval of transverse momentum reported for each particle specie is listed in Tab. 3.1

### 3.1.1 Fits to $N_\sigma$

The production of  $\pi^+$ ,  $\pi^-$ ,  $K^+$ ,  $K^-$ , p and  $\bar{p}$  in bins of  $p_T$  are obtained from fits to the number of sigmas distributions  $N_\sigma^i$  where the superindex  $i$  denotes the particle species.  $N_\sigma^i$  is constructed for all the particle species as follows

	$\pi$	K	p
Pb-Pb	0.25–0.7	0.25–0.45	0.45–0.8
pp	0.3–0.7	0.25–0.45	0.45–0.8

Table 3.1 Intervals of transverse momentum explored in the low- $p_T$  analysis for pions, kaons, and (anti)protons. Units are reported in GeV/c.

$$N_{\sigma}^i = \frac{dE/dx_{\text{expected},i} - dE/dx_{\text{measured}}}{\sigma_{dE/dx_{\text{measured}}}} \quad (3.3)$$

where  $dE/dx_{\text{measured}}$  ( $dE/dx_{\text{expected},i}$ ) is the measured energy loss (expected from the Bethe-Bloch parameterization). The particle production was studied in four different pseudorapidity intervals:  $|\eta| < 0.2$ ,  $0.2 < |\eta| < 0.4$ ,  $0.4 < |\eta| < 0.6$ ,  $0.6 < |\eta| < 0.8$ . As it will be seen, the measurements of the particle abundances made in the different pseudorapidity intervals as a function of  $p_T$  were found consistent among each other. Consequently, the particle abundances in the pseudorapidity window  $|\eta| < 0.8$  correspond to the weighted average value among the different intervals.

In the  $1/\beta^2$  region of the  $dE/dx$ , the relative separation among the different species allows to perform track-by-track identification. In the momentum region where the signals are well separated, the extraction of the yields is performed by fitting a single-function to the  $N_{\sigma}$  distributions in each  $p_T$  interval. While in regions where there is contribution from a different specie, the sum of two functions was used. The used functions correspond to a Gaussian distribution  $G$  convoluted with an exponential function  $e$ :

$$G(x; \mu, \sigma) \equiv \frac{C}{\sqrt{2\pi}\sigma} \exp\left(-\frac{(x-\mu)^2}{2\sigma^2}\right) \quad (3.4)$$

$$e \equiv \exp\left(-x\frac{\lambda}{\sigma}\right) \quad (3.5)$$

$$(G \otimes e)(x; \mu, \sigma, \lambda) \equiv \int_0^{\infty} d\tau G(x-\tau; \mu, \sigma) e(\tau, \sigma, \lambda) \quad (3.6)$$

where  $C$  corresponds to the amplitude,  $\mu > 0$  is the expected  $dE/dx$ ,  $\sigma > 0$  is associated with the width of the distribution and  $\lambda$  is an extra parameter, which controls the strength of

the tail and it was varied within the interval  $(0, 1]$ . The usage of Eq. 3.6 is motivated from the Landau distribution of the energy loss. For Pb–Pb collisions, Fig. 3.1 illustrates the quality of the fits to the  $N_\sigma$  distributions of antipions, antikaons and antiprotons. Similar results were obtained for positive charged particles.

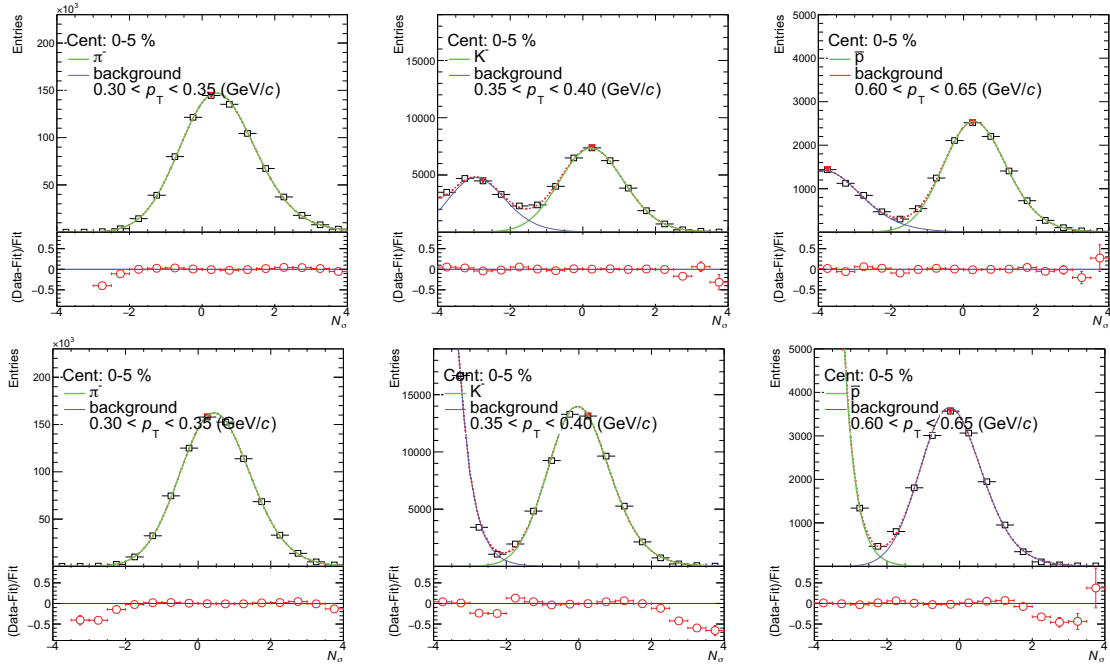


Fig. 3.1 Global fit (red-dashed-line) to  $N_\sigma$  distributions (markers). Left column correspond to  $\pi^-$  with  $p_T$  in the interval  $(0.3, 0.35)$  GeV/c. Middle column correspond to  $K^-$  with  $p_T$  in the interval  $(0.3, 0.35)$  GeV/c and the right column correspond to  $\bar{p}$  with  $p_T$  in the interval  $(0.65, 0.7)$  GeV/c. The upper-row corresponds to tracks within the pseudorapidity interval  $|\eta| < 0.2$  while the bottom-row corresponds to tracks within the interval  $0.6 < |\eta| < 0.8$ . These results correspond to the centrality class 0-5%.

### 3.1.2 Particle abundances

Particle abundances ( $f_{i,j}$ ,  $j = |\eta| < 0.2, \dots, 0.6 < |\eta| < 0.8$ ) are defined as the fractional area of the  $N_\sigma^i$  distribution, which corresponds to the integral of the curve that describes the yield of the specific particle specie, i. e. the area below the green curves (see Fig. 3.1) normalized to the respective pseudorapidity dependent inclusive charged spectrum. The accordance among the different  $f_{i,j}$  is within 5% and can be seen in Fig. 3.3. Using  $f_{i,j}$ , the weighted average was computed and it can be regarded as the particle abundances in the interval,  $|\eta| < 0.8$ . Figure 3.2 shows the abundances of  $\pi^-$ ,  $K^-$  and  $\bar{p}$  as a function of  $p_T$  for different centrality classes as well as the case for MB pp. In the remaining of the description of the

low- $p_T$  analysis, it will be referred as *particle abundance* to the quantity obtained from the weighted average.

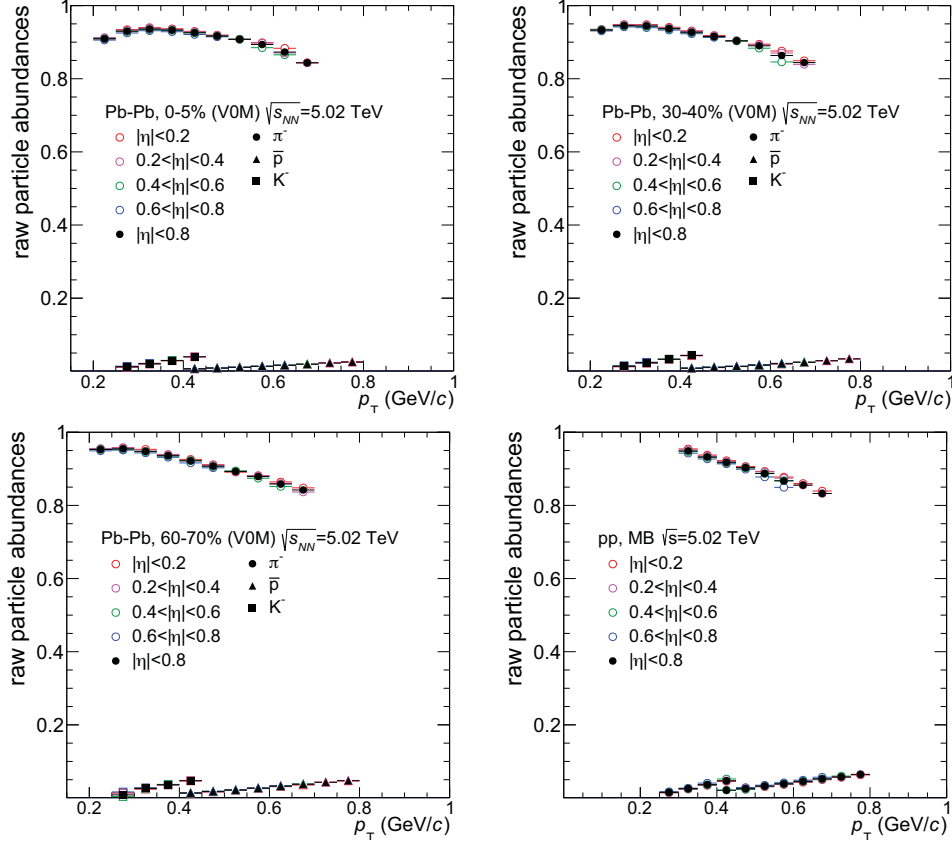


Fig. 3.2 Particle abundances for three centrality classes: 0-5% (upper-left) , 30-40% (upper-right) and 60-70% (bottom-left). The case for MB pp collisions is also shown (bottom-right). Black markers represent the weighted average.

### 3.1.3 Uncorrected $p_T$ spectra

The transverse momentum distributions for identified particles can be derived from the particle abundances as follows

$$\frac{d^2 N_{id}}{d\eta dp_T} = f_{id} \times \frac{d^2 N_{ch}}{d\eta dp_T} \quad (3.7)$$

where,  $f_{id}$  are the particle abundances, ‘id’ refers to the specie and  $\frac{d^2 N_{ch}}{d\eta dp_T}$  is the inclusive charged  $p_T$  spectrum in the pseudorapidity interval  $|\eta| < 0.8$ .



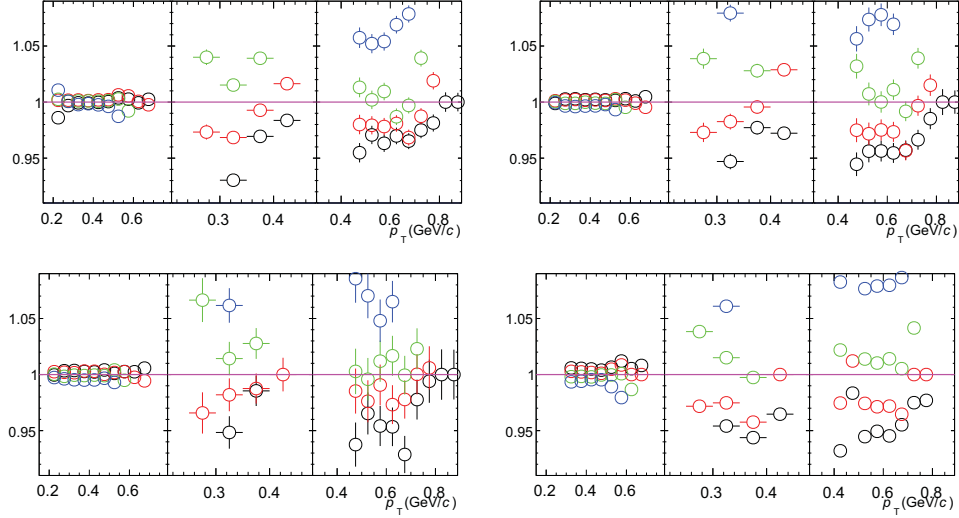


Fig. 3.3 Ratio of particle abundances in the pseudorapidity intervals;  $|\eta| < 0.2$  (black),  $0.2 < |\eta| < 0.4$  (red),  $0.4 < |\eta| < 0.6$  (green),  $0.6 < |\eta| < 0.8$  (blue) to the weighted average ( $|\eta| < 0.8$ ). Results are shown for the centrality classes, 0-5% (upper-left), 30-40% (upper-right), 60-70% (bottom-left) and pp MB (bottom-right). Results are shown for negative charged particles. Inside each panel, pions, kaons and protons are displayed from left to right. Similar results are obtained for positive charged particles.

### Building up the final $p_T$ spectra

As it will be useful in further sections, it is appropriate to give a notion on the technique adopted to build up the corrected spectra. The  $\bar{p}$  spectrum is taken as an example.

$$\frac{d^2 N_{\bar{p}}}{dp_T dy} = \left( J f_{\bar{p}} C_{FD} \frac{\epsilon_{ch}}{\epsilon_{\bar{p}}} \right) \times \frac{d^2 N_{ch}}{d\eta dp_T} \frac{1}{\epsilon_{ch}} \quad (3.8)$$

The different components are defined as follows:

- $J$ : Jacobian
- $f_{\bar{p}}$ : uncorrected abundance of anti-protons
- $C_{FD}$ : feed-down correction
- $\frac{\epsilon_{ch}}{\epsilon_{\bar{p}}}$ : relative efficiency correction
- $\frac{d^2 N_{ch}}{d\eta dp_T}$ : inclusive charged particle  $p_T$  spectrum

The set of corrections is described in Sec. 3.1.5. The advantage of the proposed form relies on the easiness to factorize the systematic uncertainties. The factorization is divided into two

components. The systematic uncertainties associated to the PID correspond to the enclosed term and the non-enclosed term is associated to the uncertainties on the event and track selection. Systematic uncertainties are discussed in Sec. 3.1.7.

### 3.1.4 Transformation of the pseudorapidity to rapidity dependence of the yields

So far, the measured quantity has been the transverse momentum and pseudorapidity dependent differential uncorrected spectra  $\left(\frac{d^2N_{id}}{dp_T d\eta}\right)$ . In order to go from pseudorapidity to rapidity dependence, Eq. 3.9. has been used

$$\frac{d^2N_{id}}{dp_T dy} = \frac{d\eta}{dy} \frac{d^2N_{id}}{dp_T d\eta} \equiv f(m_0, p_T, \eta) \frac{d^2N_{id}}{dp_T d\eta} \quad (3.9)$$

using,

$$y(m_0, p_T, \eta) = \frac{1}{2} \ln \left[ \frac{\sqrt{p_T^2 \cosh^2 \eta + m_0^2} + p_T \sinh \eta}{\sqrt{p_T^2 \cosh^2 \eta + m_0^2} - p_T \sinh \eta} \right] \quad (3.10)$$

where,  $m_0$  is the rest mass,  $p_T$  (taken as the central value of the  $i$ -th bin) and  $\eta$  are the kinematic variables of a single particle. Differentiating Eq. 3.10 with respect to  $\eta$  keeping constant  $m_0$  and  $p_T$ , Eq. 3.11 was obtained. To calculate the Jacobians, Eq. 3.11 was integrated over the  $\eta$  variable in the interval  $[-0.8, 0.8]$  keeping  $m_0$  and  $p_T$  fixed. The reason for integrating in the interval  $[-0.8, 0.8]$  and further divided by 1.6 is due to the fact that instead of using a random value of  $\eta$  in  $|\eta| \leq 0.8$  for the calculation of the rapidity, it is rather assumed that the value of  $\eta$  is an average one inside the cone limited by  $|\eta| \leq 0.8$ . As expected, the contribution of the Jacobian is largest for heavy particles and  $p_T$  below 1 GeV/c (see Fig. 3.4).

$$\frac{dy}{d\eta} = \sqrt{1 + \left(\frac{m_0}{p_T \cosh \eta}\right)^2} \quad (3.11)$$

### 3.1.5 Corrections

The invariant yields have been corrected as follows:

- **Efficiency correction:** For the Pb-Pb analysis, the efficiency correction were calculated using the HIJING Monte Carlo (inside the ALICE collaboration, such Monte Carlo production was labeled as LHC16j7a, which is anchored to LHC15o pass4

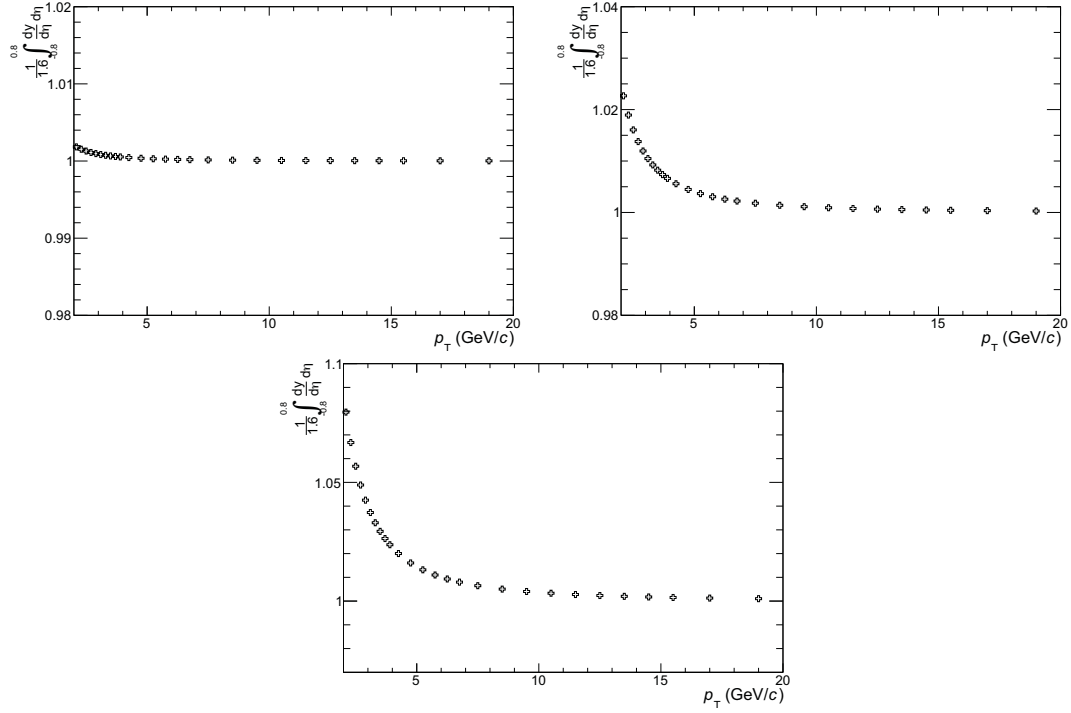


Fig. 3.4 Jacobian factors for pions (upper-left), kaons (upper-right) and protons (bottom).

period) while for the pp analysis, the Pythia 8 - Monash Monte Carlo (LHC16k5a production anchored to the LHC15n pass3 period) was used. Figure 3.5 shows the efficiency times acceptance correction for each particle specie. Results for particles and anti-particles are compared for a fixed centrality class. The efficiencies are presented for a wide  $p_T$  interval (up to 20 GeV/c), the jump at 2 GeV/c is due to an extra cut which is implemented in the relativistic rise analysis, details on this cut are presented in Sec. 3.2. From the plots a small centrality dependence was observed, in fact, it can be quantified by plotting the ratios of the centrality dependent efficiencies to those for MB events (0-90%). The ratios to MB efficiencies are shown in Fig. 3.6. For pions and kaons the maximum difference reaches 3% for  $p_T > 0.3$  GeV/c, while for (anti)protons, a similar level of agreement is observed for  $p_T > 0.4$  GeV/c. Each centrality dependent  $p_T$  spectrum has been corrected using the respective efficiency.

- **Geant/Fluka correction:** Is an absorption correction and has been applied to correct the  $K^-$  efficiency. The same corrections was applied to the Pb-Pb and pp analysis.
- **Geant3/Geant4 correction:** It corrects for anihilation and material interactions. It has been applied to correct the  $\bar{p}$  efficiency. The same correction was applied to the Pb-Pb and pp analysis.

- **Feed-down correction:** The contamination of secondary particles to the pion(proton) yield by weak decays of  $K_S^0(\Lambda)$  or interactions with the material is typically underestimated in current event generators. Hence, the contamination was estimated from data. In fact, the transverse distance-of-closest-approach ( $DCA_{xy}$ ) distribution for selected tracks was fitted with three distributions (‘templates’ in the following) corresponding to the expected shapes of primary particles, secondaries from material and secondaries from weak decays, as extracted from Monte Carlo. To generate the  $DCA_{xy}$  distributions, a  $3\text{-}\sigma$  cut was implemented to ensure tracks with the desired identity (see Eq. 3.3). For example, Fig. 3.7 shows the  $DCA_{xy}$  distributions of  $\pi^-$  ( $\pi^+$ ), which were obtained from tracks with  $0.3 < p_T < 0.35$  GeV/c,  $|\eta| < 0.8$ , and the  $|N_{\sigma}^{\pi^-}| < 3$  ( $|N_{\sigma}^{\pi^+}| < 3$ ) cut. The performance of the template fit is illustrated in Fig. 3.7 for  $\pi^+$  ( $\pi^-$ ). Similarly, the performance of the fit for  $p$  ( $\bar{p}$ ) is illustrated in Fig. 3.8. The performance for MB pp collisions is illustrated in Fig. 3.9.

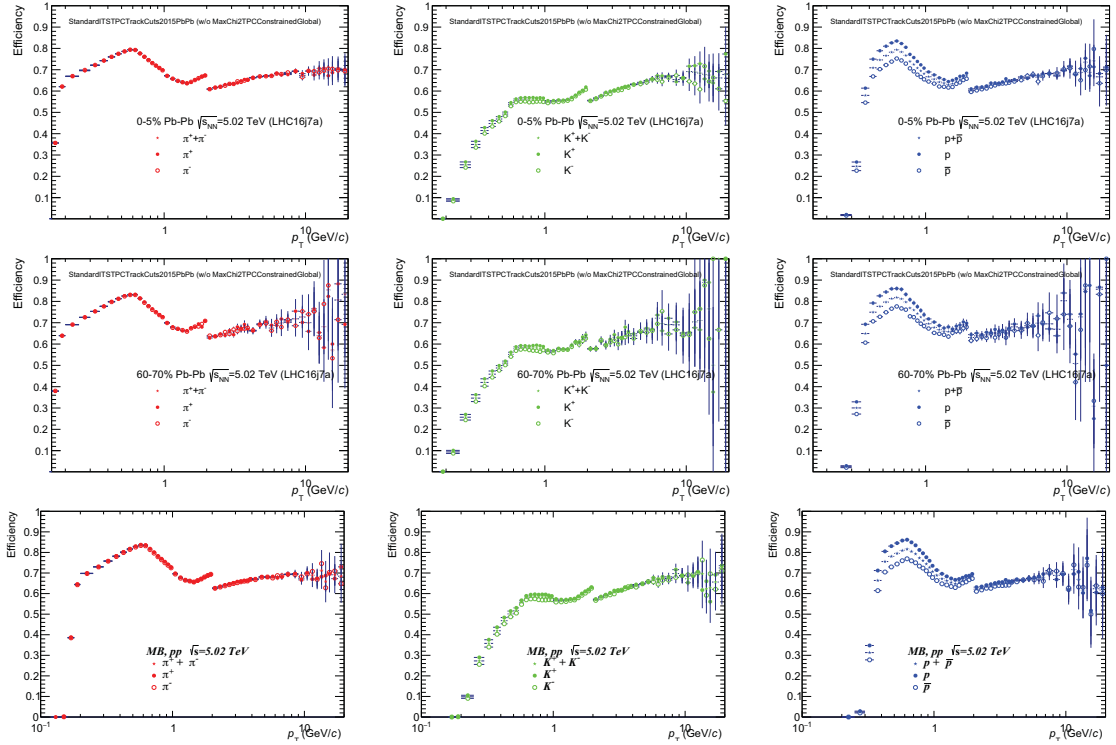


Fig. 3.5 Tracking efficiency for pions (left), kaons (middle) and protons (right) as a function of  $p_T$ . The efficiency of inclusive identified charged particles for positive and negative(stars) are compared to positive(negative) charged particles in bold(empty) circles. Two centrality classes are shown: 0-5% (top) and 60-70% (middle), the case for pp MB is also shown.

Once the  $DCA_{xy}$  distributions are fitted, and the contributions from secondaries are determined, the  $p_T$ -dependent DCA cut for primary track selection is implemented

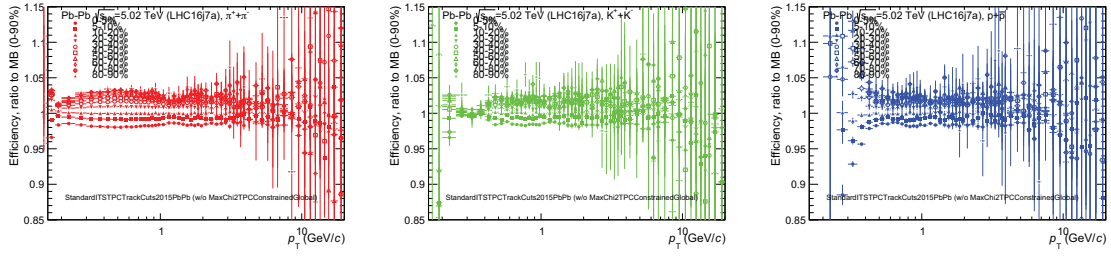


Fig. 3.6 The centrality dependent tracking efficiency is normalized to that for MB (0-90%). Results for charged pions (left), kaons (middle) and (anti)protons (right) are presented.

$$|DCA_{xy}| < 0.015 + \frac{0.0350}{p_T^{1.1}} \quad (3.12)$$

Then, the area below the curve is considered to determine the final contribution of primary particles. The estimation of primary particles before and after the  $DCA_{xy}$  cut are presented in Fig. 3.10 and Fig. 3.11 for Pb–Pb (two centralities) and MB pp collisions, respectively. For the Pb–Pb results, there is an obvious centrality dependence. The correction factor is larger for central than for peripheral collisions. Moreover, for  $p_T < 0.6 \text{ GeV}/c$  the correction factor is higher for protons than for anti-protons, a similar effect was observed in MC.

### 3.1.6 Crosschecks

- **Comparison of the fully corrected particle to anti-particle spectrum.** After the implementation of all the corrections as discussed in Sec. 3.1.5, the anti-particle to particle  $p_T$  spectrum ratio for each specie was computed. Overall, the agreement between negative and positive charged particles is within 3% (see Fig. 3.12).
- **Check the pseudorapidity dependence of the efficiency.** The ratio between  $|\eta| < 0.4$  and  $|\eta| < 0.8$  efficiencies was computed for different centrality classes. A consistency of about 2% was found (see Fig. 3.13).

### 3.1.7 Systematic uncertainties

The systematic error associated to each  $p_T$  spectrum was factorized into two different and independent components (see Sec. 3.1.3). The two different sources of uncertainties are associated to PID and event/track selection. In the following, the different sources are discussed.

#### 1. PID

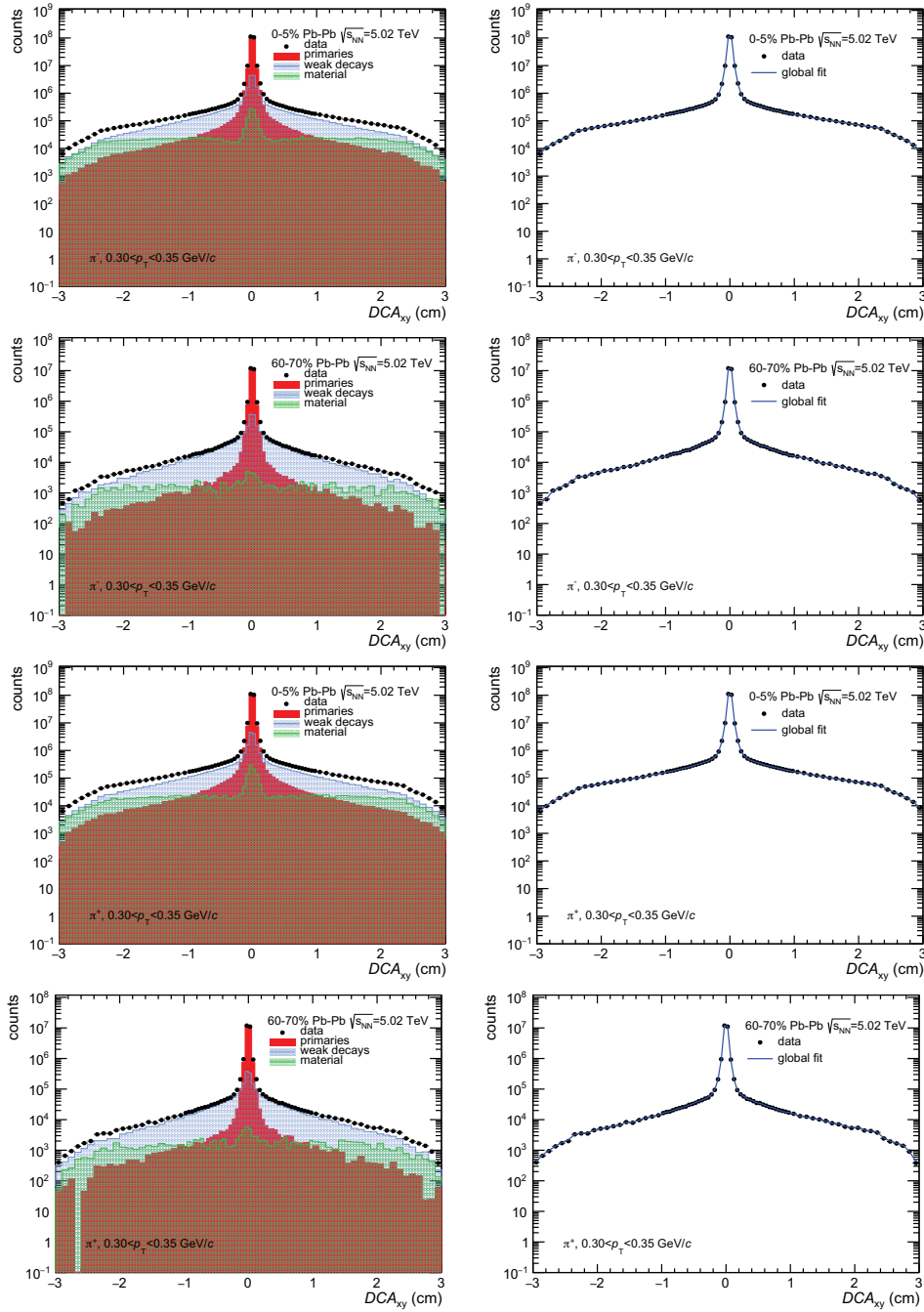


Fig. 3.7  $DCA_{xy}$  template fit for  $\pi^-$  (first two rows) and  $\pi^+$  (last two rows) with  $p_T$  within  $(0.3, 0.35)$  GeV/c. Results are shown for Pb-Pb central collisions in the first and third column. The case for Pb-Pb peripheral collisions is shown in the second and fourth rows. The individual components: primary (red area), weak decays (blue area) and material (green area) are displayed in the left-hand side plots, while, the right-hand side plots show how well the fitted function (blue line) describes the data (full markers).

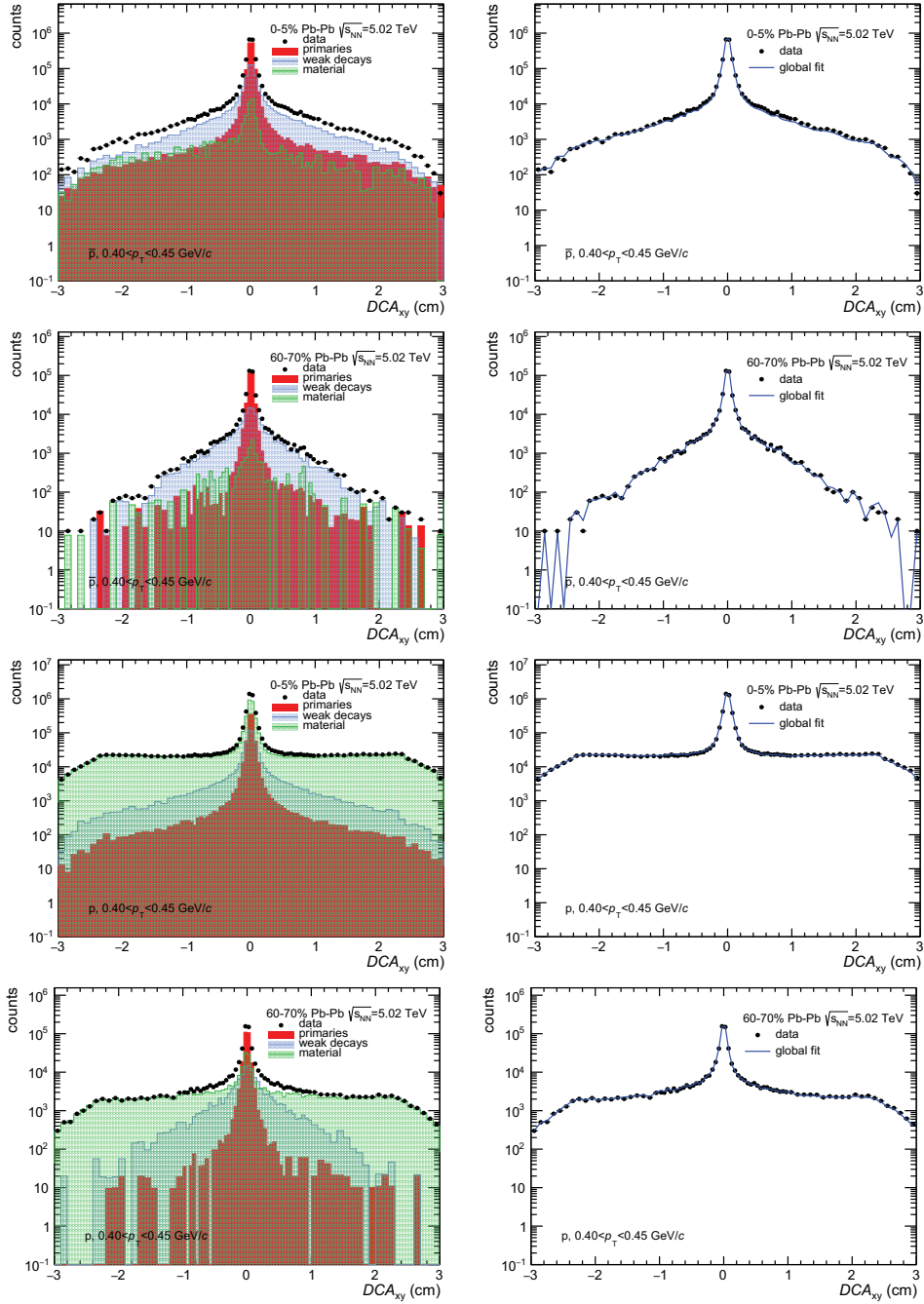


Fig. 3.8  $DCA_{xy}$  template fit for  $p$  and  $\bar{p}$  with  $p_T$  within  $(0.4, 0.45)$  GeV/c. Results are shown for Pb-Pb central collisions in the first and third column. The case for Pb-Pb peripheral collisions is shown in the second and fourth rows. The individual components: primary (red area), weak decays (blue area) and material (green area) are displayed in the left-hand side plots, while, the right-hand side plots show how well the fitted function (blue line) describes the data (full markers).

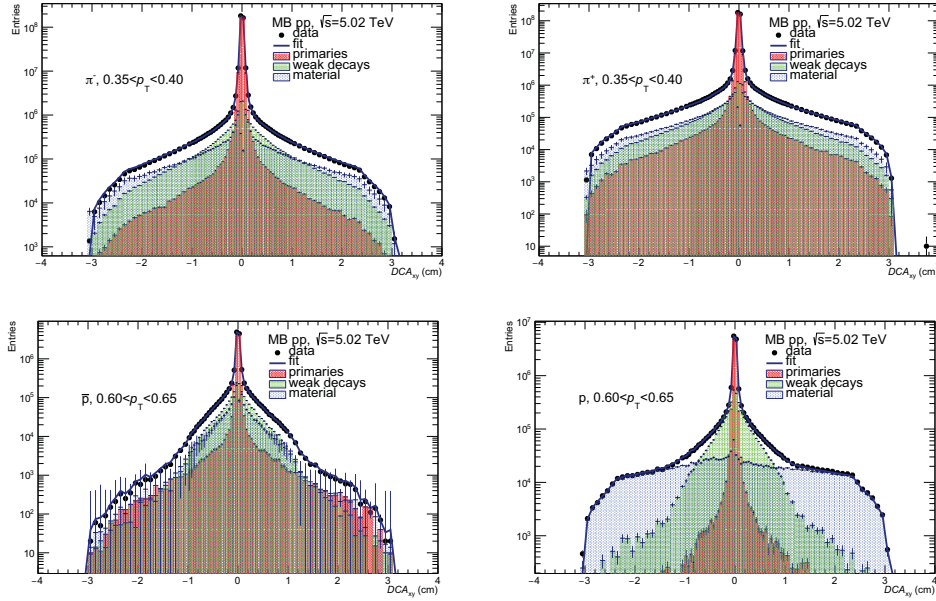


Fig. 3.9  $DCA_{xy}$  template fit for  $\pi^-$  ( $\pi^+$ ) with  $p_T$  within (0.35, 0.40) GeV/c is shown in the upper-row. The case for  $p$  ( $\bar{p}$ ) with  $p_T$  within (0.60, 0.65) is shown in the bottom-row. These results correspond to MB pp collisions.

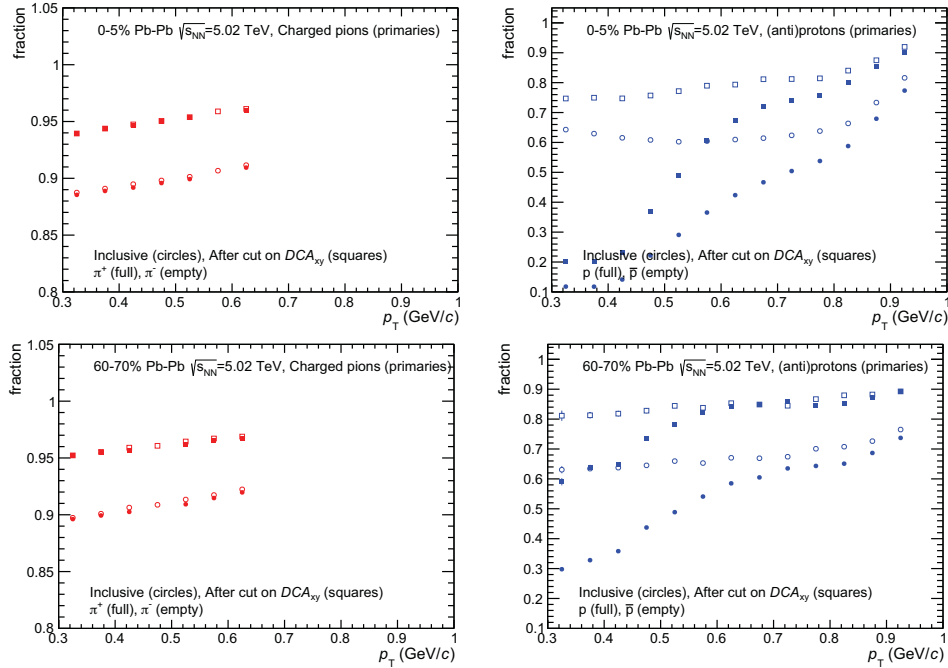


Fig. 3.10 Fraction of primary charged pions (left) and (anti)protons (right) as a function of  $p_T$  for central (top) and peripheral (bottom) Pb-Pb collisions. The fractions are presented for the cases before (circles) and after (squares) the  $p_T$  dependent  $DCA_{xy}$  cut.



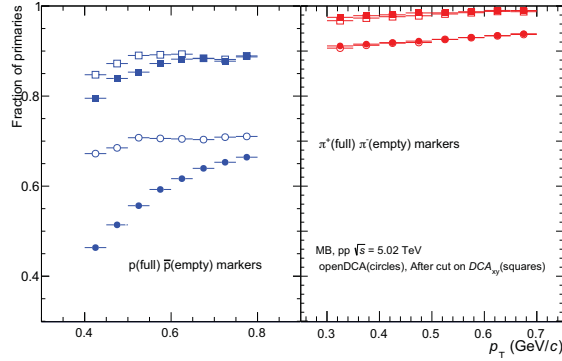


Fig. 3.11 Fraction of primary particles as a function of  $p_T$  before and after the  $DCA_{xy}$  cut. Left panel shows the case for p( $\bar{p}$ ), while right panel shows the case for  $\pi^+$  ( $\pi^-$ ). These results correspond to MB pp collisions.

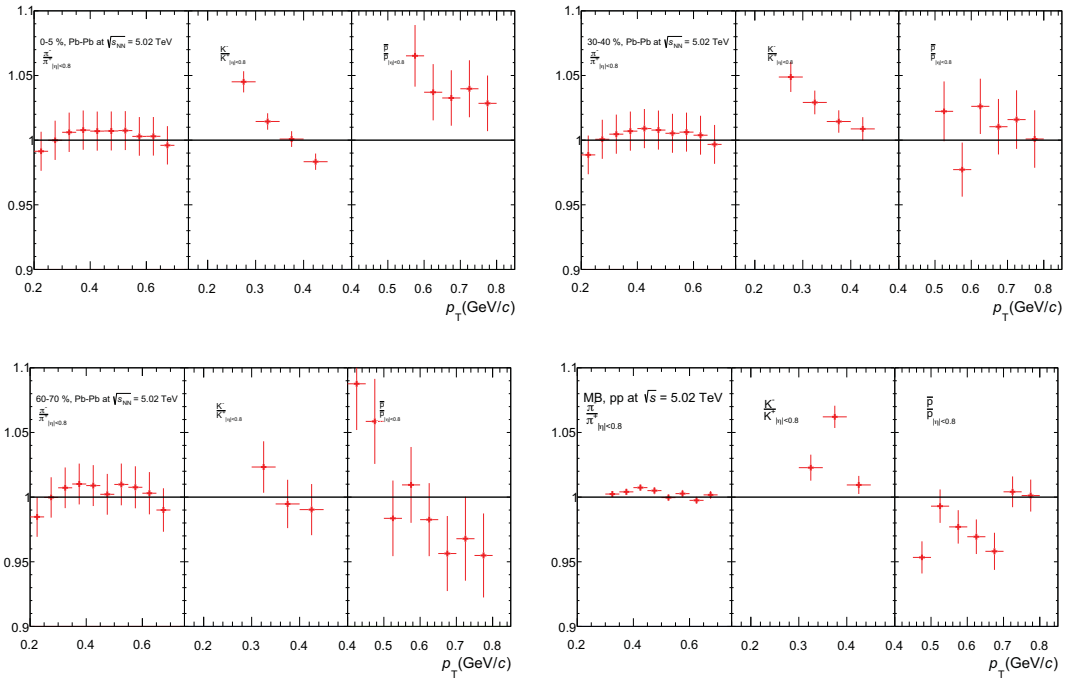


Fig. 3.12 Fully corrected anti-particle to particle spectra ratios. Three centrality classes are shown: 0-5% (upper-right corner), 30-40% (upper-left corner), 60-70% (lower-left corner) and MB pp collisions (lower-right corner).

- The effect of changing the number of clusters ( $N_{cl}$ ) used for the reconstruction of  $dE/dx$  in the TPC was studied. The maximum deviation in the particle ratios (among the different pseudorapidity intervals defined in Sec. 3.1.2) when using

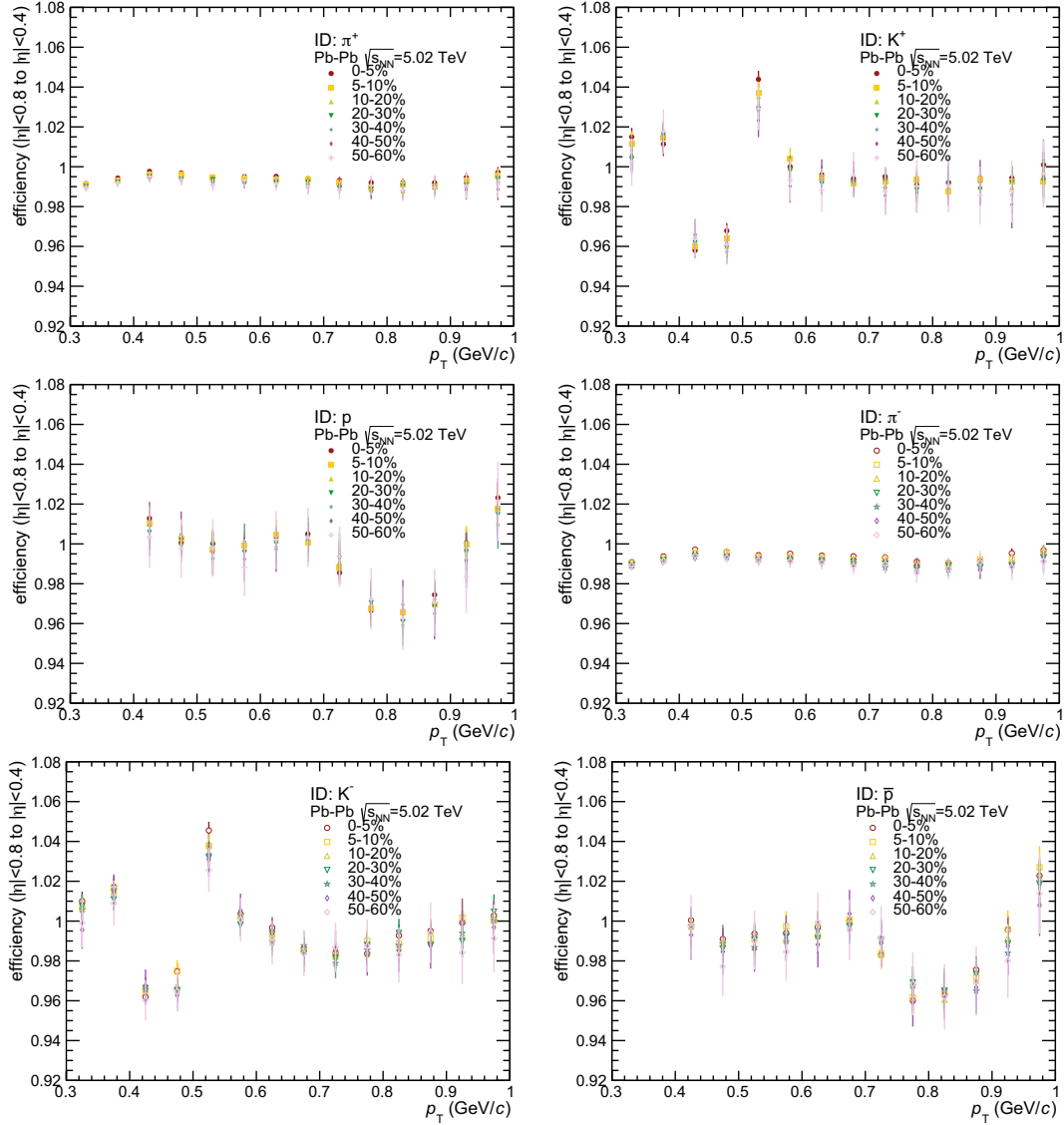


Fig. 3.13 Efficiency calculated at  $|\eta| < 0.8$  normalized to that obtained at  $|\eta| < 0.4$ . Results for pions (left), kaons (middle) and protons (right) are presented for different collision centralities.

$N_{cl} = 70$  and  $N_{cl} = 90$  was assigned as a contribution to the PID systematic uncertainty

- The strategy used to obtain the raw particle ratios was changed. Instead of fitting the  $N_\sigma$  distributions, the particle abundances were obtained by bin counting in the interval:  $[-3\sigma, +3\sigma]$
- Correction factors obtained using different MC agree within 1%, this difference is assigned as systematic uncertainty

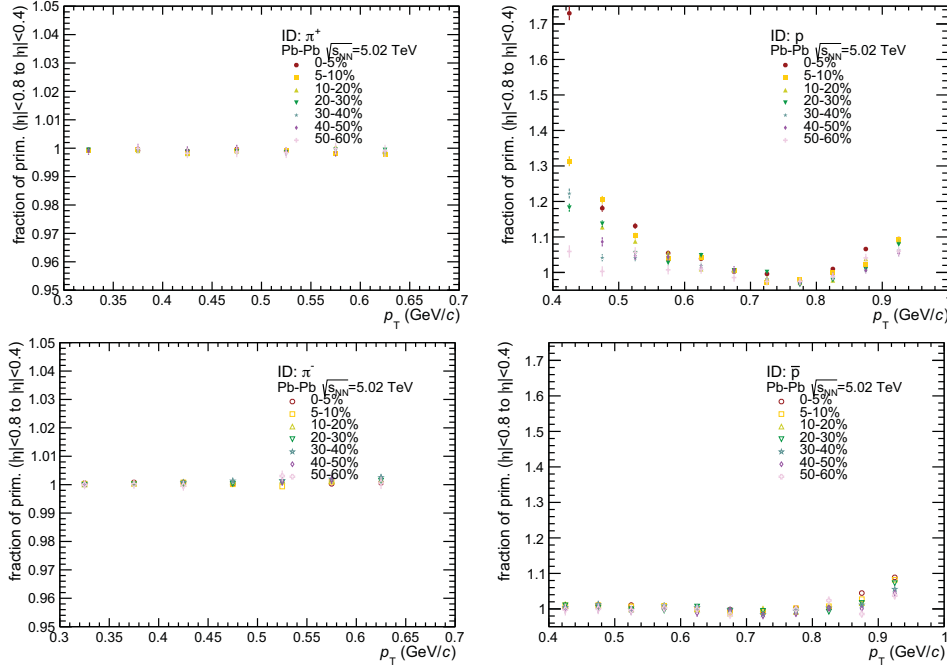


Fig. 3.14 Feed-down correction measured at  $|\eta| < 0.8$  normalized to that obtained at  $|\eta| < 0.4$ . Results for pions (left) and protons (right) are presented for different collision centralities.

- The interval for the template fit of the  $DCA_{xy}$  distributions was varied from  $[-3\text{cm}, +3\text{cm}]$  to  $[-1\text{cm}, +1\text{cm}]$ , the difference was assigned as systematic uncertainty

## 2. Track and event selection

- **Track cuts** The track cuts were varied in both raw  $p_T$  spectra and efficiency (see Tab. 3.2), the maximum difference on the (efficiency corrected) inclusive charged particle  $p_T$  yield was assigned as systematic uncertainty. Figure 3.15 shows the systematic uncertainties for central and peripheral Pb–Pb collisions, the total uncertainty is  $p_T$  dependent and below 3%.

- **Matching efficiency and  $p_T$  resolution.** The ratio,  $\text{Unc}(p_T) = \frac{\epsilon_{\text{matching}}^{\text{MC}}(p_T)}{\epsilon_{\text{matching}}^{\text{Data}}(p_T)}$  was used to quantify the uncertainty on the ITS-TPC matching efficiency.  $\epsilon_{\text{matching}}^{\text{MC}}$  ( $\epsilon_{\text{matching}}^{\text{MC}}$ ) is defined as the ratio between tracks reconstructed only with the TPC to tracks reconstructed with the TPC with SPD hits using data (MC), respectively. These values were taken from the  $R_{AA}$  analysis of inclusive charged particles at  $\sqrt{s_{NN}} = 5.02$  TeV.

Track cut	Nominal value	Lower value	Higher value
Min. number of crossed rows	70	60	100
Min. ratio crossed rows over findable TPC clusters	0.8	0.7	0.9
Max. $\chi^2$ per cluster in TPC	4	3	5
Max. $\chi^2$ per cluster in ITS	36	25	49
SPD point	required	not required	not required
$DCA_{xy}$	$7\sigma$	$4\sigma$	$10\sigma$
$DCA_z$	2	1	5

Table 3.2 Track cut variations

- **Event selection.** The systematic uncertainty associated to the event selection is of the order of 0.5%. This value was obtained after varying the cut on the event selection.

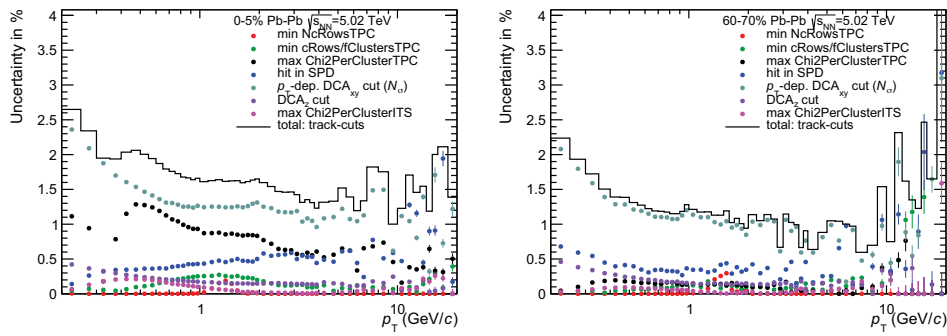


Fig. 3.15 Systematic uncertainties attributed to track selection, results for central (left) and peripheral (right) Pb-Pb collisions are shown. The different contributions are displayed as color markers and the total uncertainty as solid line.

A summary of the systematic uncertainties for three centrality classes are found in Figs. 3.16, 3.17 and 3.18 for pions, kaons and protons, respectively. The results for MB pp can be found in Fig. 3.19

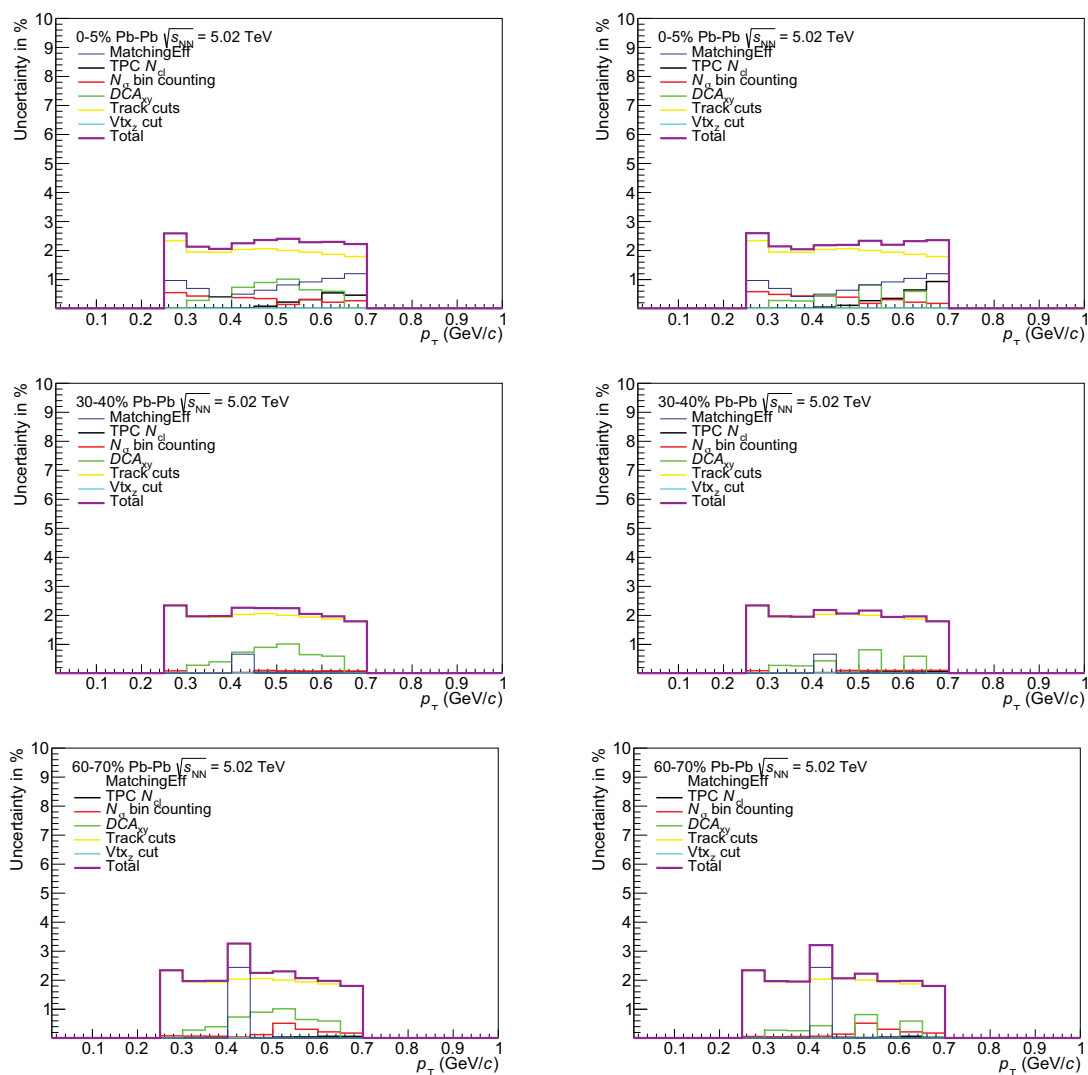


Fig. 3.16 Summary of systematic uncertainties for both,  $\pi^+$  (left-column) and  $\pi^-$  (right-column). Three centrality classes are shown: 0-5% (first row), 30-40% (middle row) and 60-70% (bottom row). The total systematic uncertainty is the quadrature-sum of all the components.

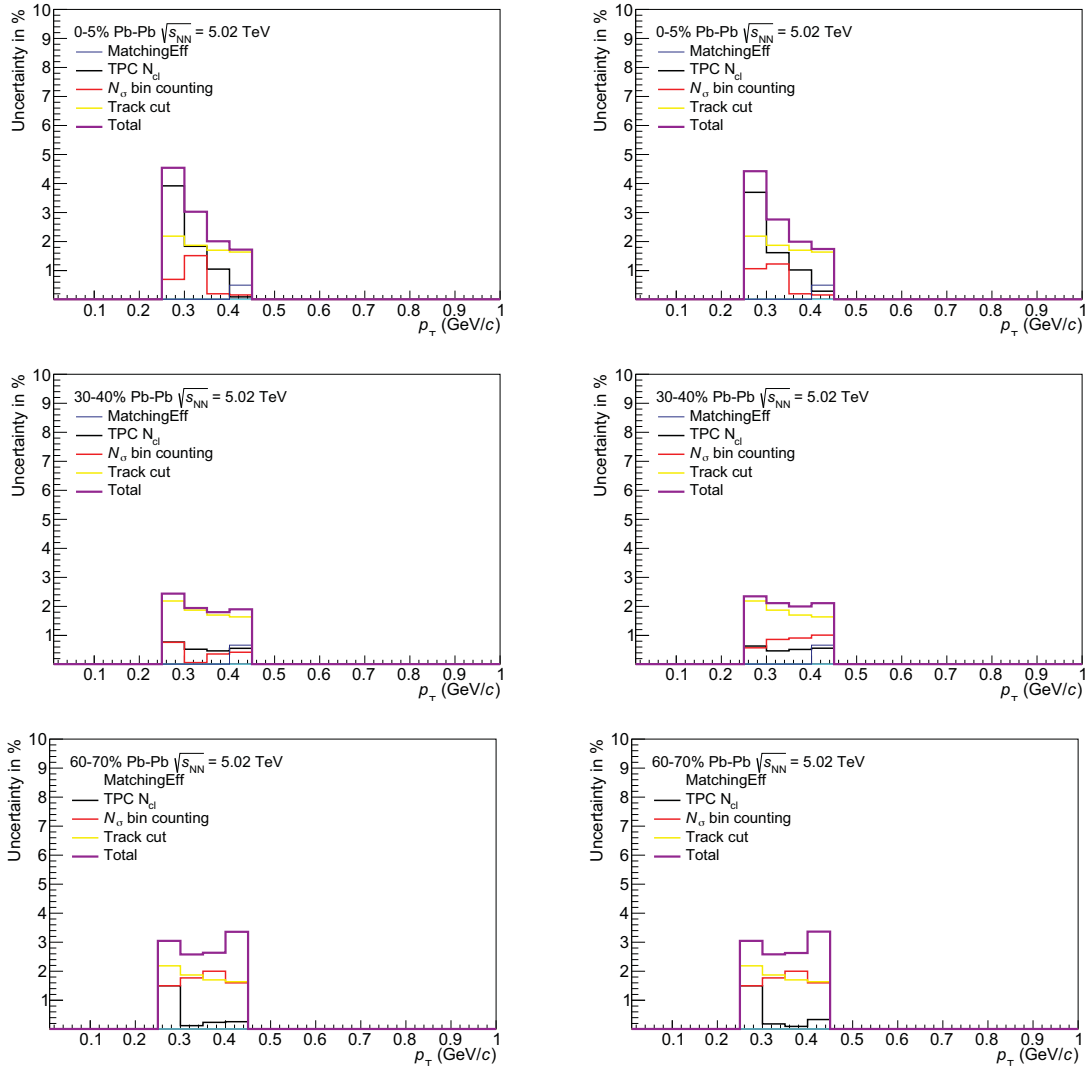


Fig. 3.17 Summary of systematic uncertainties for both,  $K^+$  (left column) and  $K^-$  (right column). Three centrality classes are shown: 0-5% (first row), 30-40% (middle row) and 60-70% (bottom row). The total systematic uncertainty is the quadrature-sum of all the components.

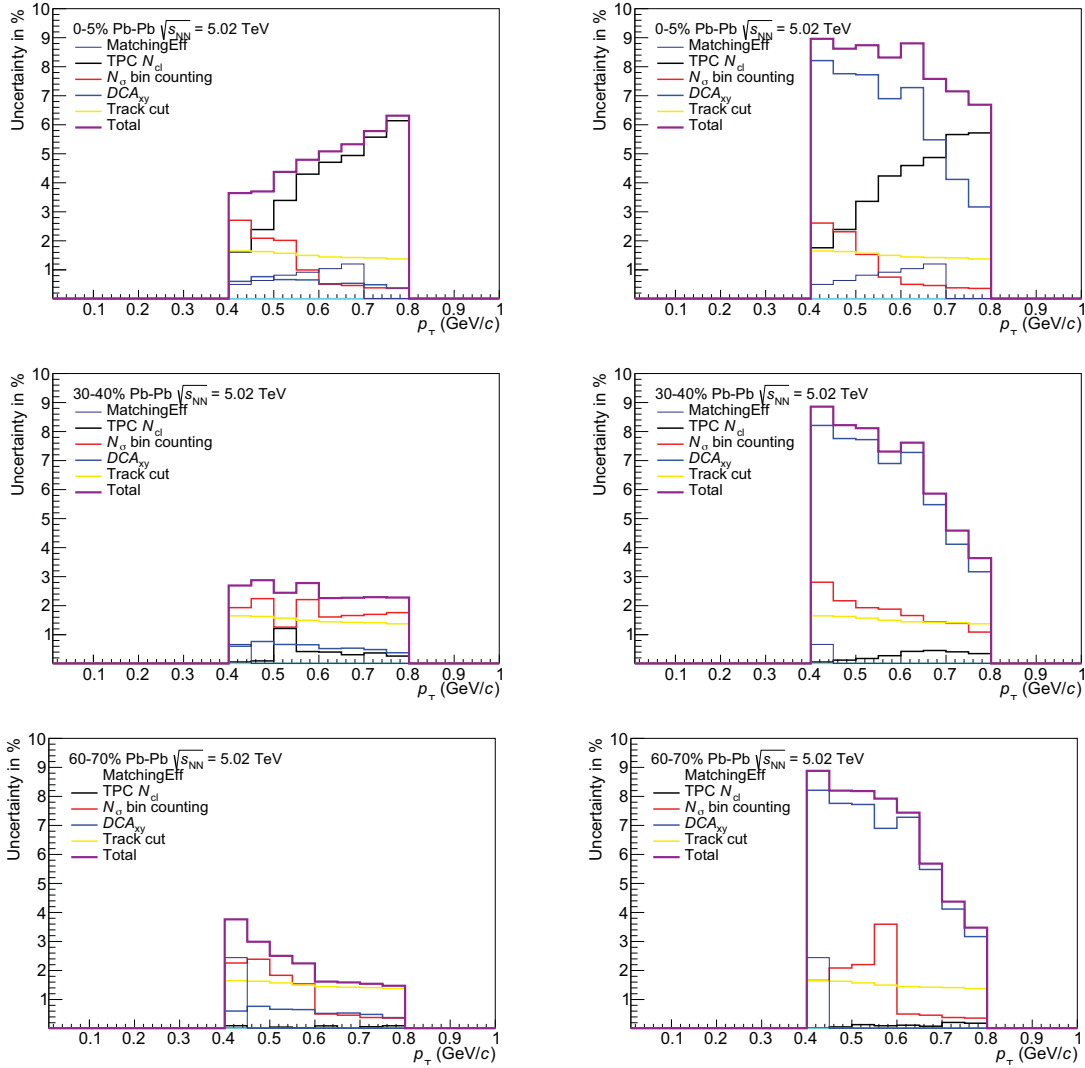


Fig. 3.18 Summary of systematic uncertainties for both,  $p$  (left column) and  $\bar{p}$  (right column). Three centrality classes are shown: 0-5% (first row), 30-40% (middle row) and 60-70% (bottom row). The total systematic uncertainty is the quadrature-sum of all the components.

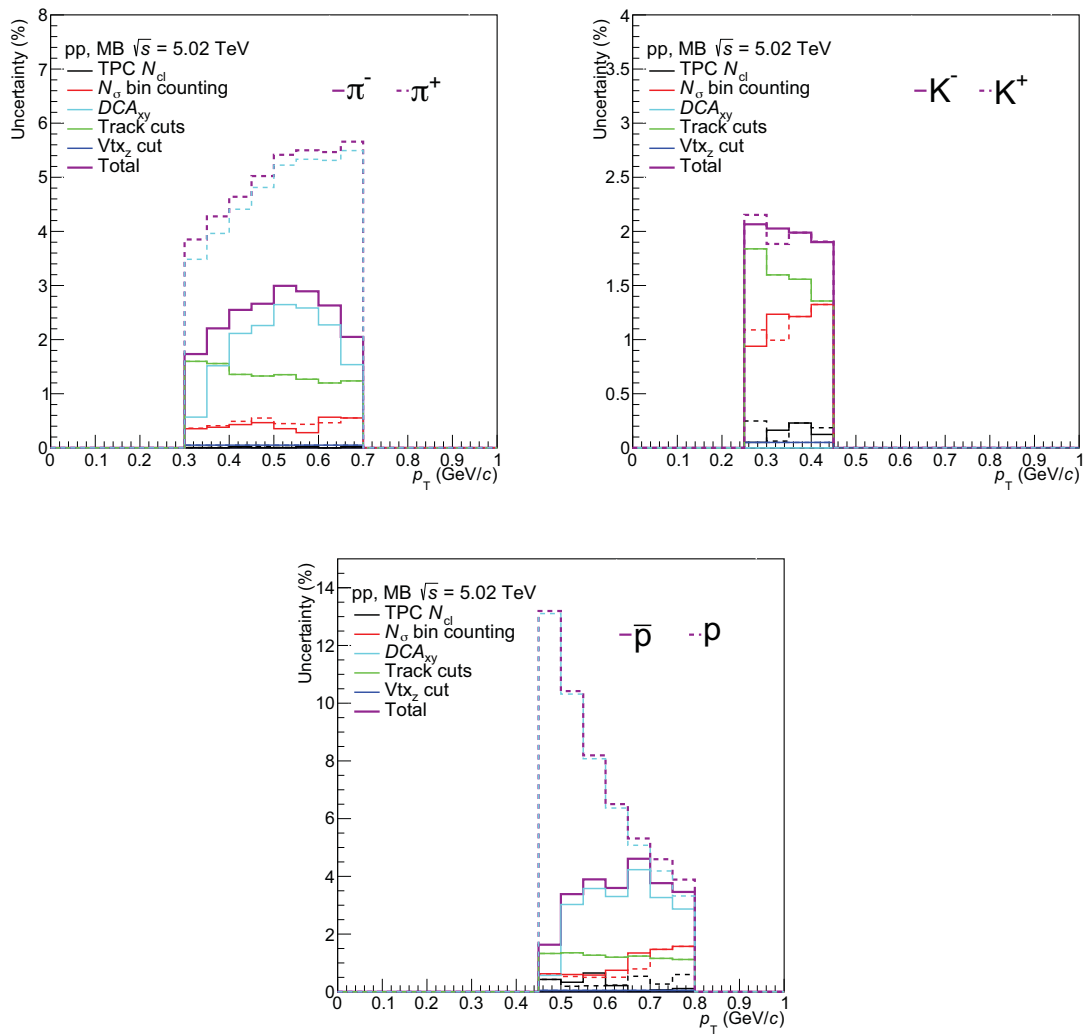


Fig. 3.19 Summary of systematic uncertainties for both, particle (dashed line) and anti-particle (continuous line) for pp collisions. The results for pions, kaons, and protons are shown in the upper-left panel, upper-right panel and bottom panel, respectively. The total systematic uncertainty is the quadrature-sum of all the components.



## 3.2 High $p_T$ analysis

The purpose of this section is to describe the strategy adopted to measure the production of charged pions, kaons and (anti)protons at the relativistic rise of the ALICE TPC. In contrast to the low- $p_T$  analysis, due to statistical limitations, only results for charged particles (sum of positive and negative charged particles) are presented. The  $p_T$  intervals surveyed are listed in Tab. 3.3. The technique adopted was previously reported in [57–59].

	$\pi$	K	p
Pb-Pb	2–20	3–20	3–20
pp	2–20	3–20	3–20

Table 3.3 Intervals of transverse momentum explored in the high- $p_T$  analysis for pions, kaons, and protons. Units are reported in GeV/ $c$ .

### 3.2.1 Additional cut on the $\varphi$ angle

Apart from the track cuts used in the low- $p_T$  analysis, this analysis takes in an additional cut on the azimuthal angle ( $\varphi$ ). It is applied to tracks with  $p_T$  greater than 2 GeV/ $c$ . The reason for this is that tracks that are close to the TPC boundaries are likely to have a bad performance due to cluster losses and because clusters close to the TPC frontiers are not taken into account for the  $dE/dx$  calculation. To incorporate different settings of magnetic polarities, positive and negative charged particles, the cut is thought in terms of  $\varphi'$  variable as:

- $\varphi' = \varphi$
- if  $B < 0$  then  $\varphi' = 2\pi - \varphi$
- if  $q < 0$  then  $\varphi' = 2\pi - \varphi$
- $\varphi' = \varphi + \pi/18$
- $\varphi' = \varphi$  modulo  $\pi/9$  (a TPC sector of 30 degrees)
- if  $\varphi' < \frac{0.12}{p_T} + \frac{\pi}{18.0} + 0.035$  and  $\varphi' > \frac{0.1}{p_T} + \frac{\pi}{18.0} - 0.025$ , the track is rejected

### 3.2.2 Calibration of $dE/dx$ vs $\eta$

Particle identification in the relativistic rise region requires a good knowledge of the detector response. The measured  $dE/dx$  (i.e. the truncated mean of the deposited charge on the TPC pad-row) depends not only on  $\beta\gamma$  but also on the length and inclination angle of the track. This would suggest a dependence of  $\langle dE/dx \rangle$  on  $\eta$ . Hence, a slight recalibration of the TPC signal is needed. The recalibration procedure involves pion MIPs, defined as pions having  $0.4 < p < 0.6 \text{ GeV}/c$  and  $40 < dE/dx < 60$ . Based on the fact that the  $dE/dx$  of pion MIPs is around 50, factors such that make the  $dE/dx$  of pion MIPs in the pseudorapidity interval  $|\eta| < 0.8$  constant are sought. In order to test the quality of the calibration, the same factors were applied to electrons within the same momentum interval but having a  $dE/dx$  in the interval  $70 < dE/dx < 90$ . Figure 3.20 shows the performance of the calibration. Results for central (0-5%) and peripheral (60-70%) Pb–Pb collisions are shown. It was observed that the central collisions are much sensitive to the pseudorapidity dependence than peripheral collisions. Consequently, the calibration procedure has a better performance for peripheral events. As it was done in the low- $p_T$  analysis, the production of identified charged particles is studied in narrow pseudorapidity intervals ( $|\eta| < 0.2$ ,  $0.2 < |\eta| < 0.4$ ,  $0.4 < |\eta| < 0.6$  and  $0.6 < |\eta| < 0.8$ ). By splitting into four different pseudorapidity intervals, it is meant to have flat shapes of the  $dE/dx$  in narrower windows. Any dependence of the  $dE/dx$  on  $\phi$  was negligible.

### 3.2.3 $V^0$ selection and parameterizations of the Bethe-Bloch and resolution curves

The parameterization of the Bethe-Bloch(BB) and resolution curves was achieved using external samples of secondary particles such as primary pions selected with the TOF detector, pions(protons) from weak decays of  $K_s^0(\Lambda)$  and electrons from  $\gamma$ -conversion. Firstly, the  $dE/dx$  distribution of these external samples was studied to extract the mean ( $\langle dE/dx \rangle$ ) and sigma ( $\langle \sigma_{\langle dE/dx \rangle} \rangle$ ) values. Figure 3.21 and Fig. 3.22 show the  $dE/dx$  of external samples for Pb-Pb and MB pp collisions, respectively. This information allows to construct the following correlations:  $\langle dE/dx \rangle$  vs.  $\beta\gamma$  and  $\sigma_{dE/dx}/\langle dE/dx \rangle$  vs.  $\langle dE/dx \rangle$ . Figure 3.23 shows the parameterizations of the previously mentioned correlations for central (0-5%), peripheral (60-70%) Pb-Pb collisions and MB pp collisions. For all the centralities, the Bethe-Bloch parameterizations exhibit a slight pseudorapidity dependence while the resolution is observed to be larger for short ( $|\eta| < 0.2$ ) than for long  $0.6 < |\eta| < 0.8$  tracks. The resolution curves for pp collisions seem to be in agreement. In addition, the largest relative resolution ( $\approx 7.5\%$ )

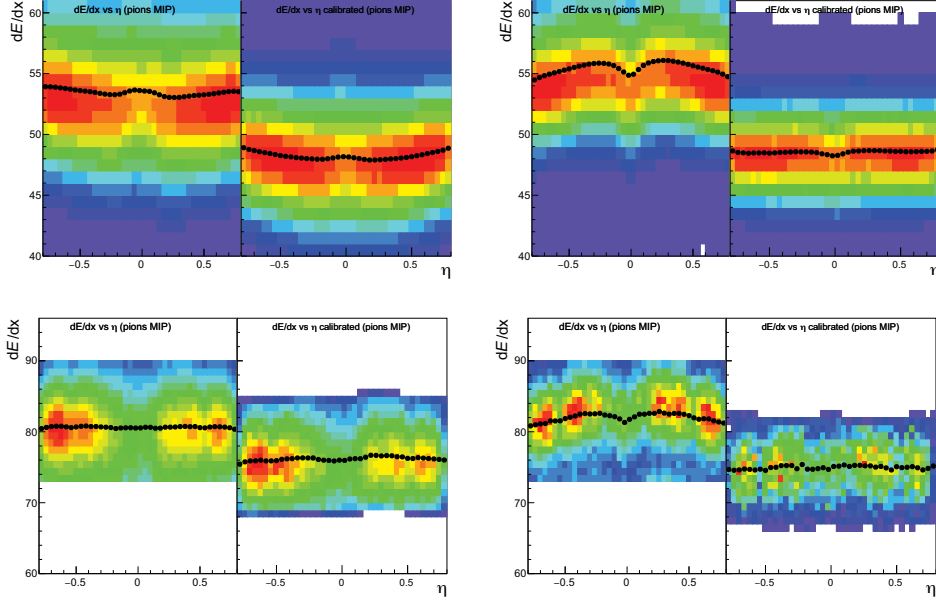


Fig. 3.20  $dE/dx$  vs.  $\eta$  before and after the calibration. Tracks having momentum in the interval,  $0.4 < p < 0.6$  GeV/c were used. Results are shown for pions (upper-row) and electrons (bottom-row) for two different centrality classes, 0-5% (left-column) and 60-70% (right-column). Each panel shows the result before and after the calibration.

is achieved for short tracks in central collisions, while for peripheral collisions it amounts to 5 – 5.5%.

### 3.2.4 Fits to $dE/dx$

The parameterizations from Fig.3.23 were used to perform a two-dimensional fit to the primary particles  $dE/dx$  vs.  $p$  correlation. All of the parameters obtained from the parameterization of the BB (except the one that describes the approach to the plateau) were fixed. The tuned parameterizations (one for each pseudorapidity interval) were used to fit in momentum intervals the  $dE/dx$  distribution using a sum of four Gaussian distributions, each Gaussian distribution is associated to the pions, kaons, protons, and electrons signal, respectively. The  $\langle dE/dx \rangle$  and  $\sigma_{\langle dE/dx \rangle}$  for each Gaussian distribution were retrieved from the parameterizations just described. The only extracted fit-parameters were the amplitudes of the Gaussian distributions. Figures 3.24 and 3.25 show examples of fits to Pb–Pb data and Fig. 3.26 shows the performance of the fits on MB pp data.

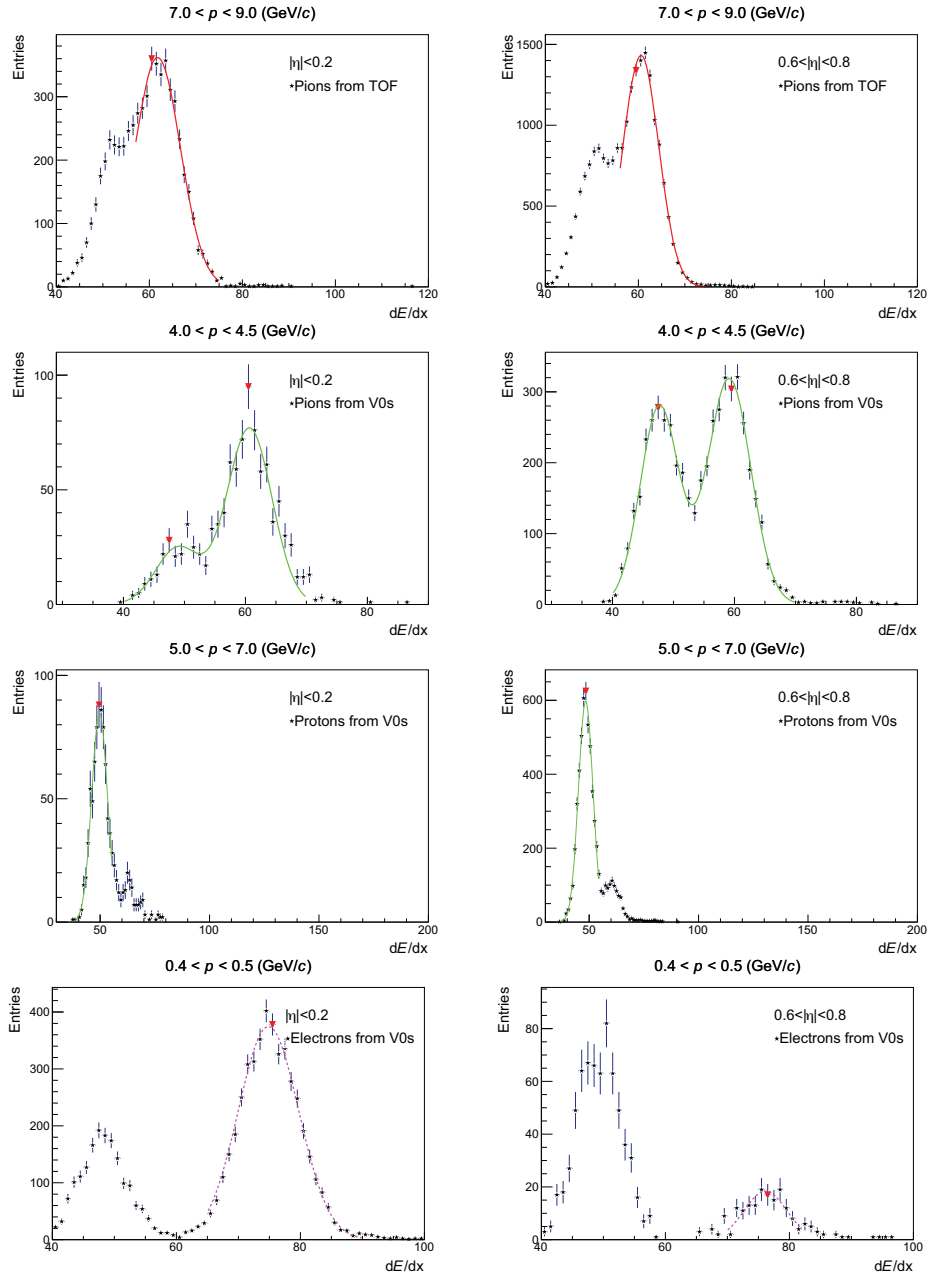


Fig. 3.21 Fit to external particle samples. High momentum pions detected with the TOF,  $dE/dx \approx 60$  (first row). Pions from weak decays of  $K_S^0$ ,  $dE/dx \approx 60$  (second row). Protons from weak decays of  $\Lambda$ ,  $dE/dx \approx 50$  (third row). Electrons from  $\gamma$ -conversion,  $dE/dx \approx 80$  (fourth row). Left(right) column corresponds to  $|\eta| < 0.2$  ( $0.6 < |\eta| < 0.8$ ). These results correspond to a centrality class of 0-5%.

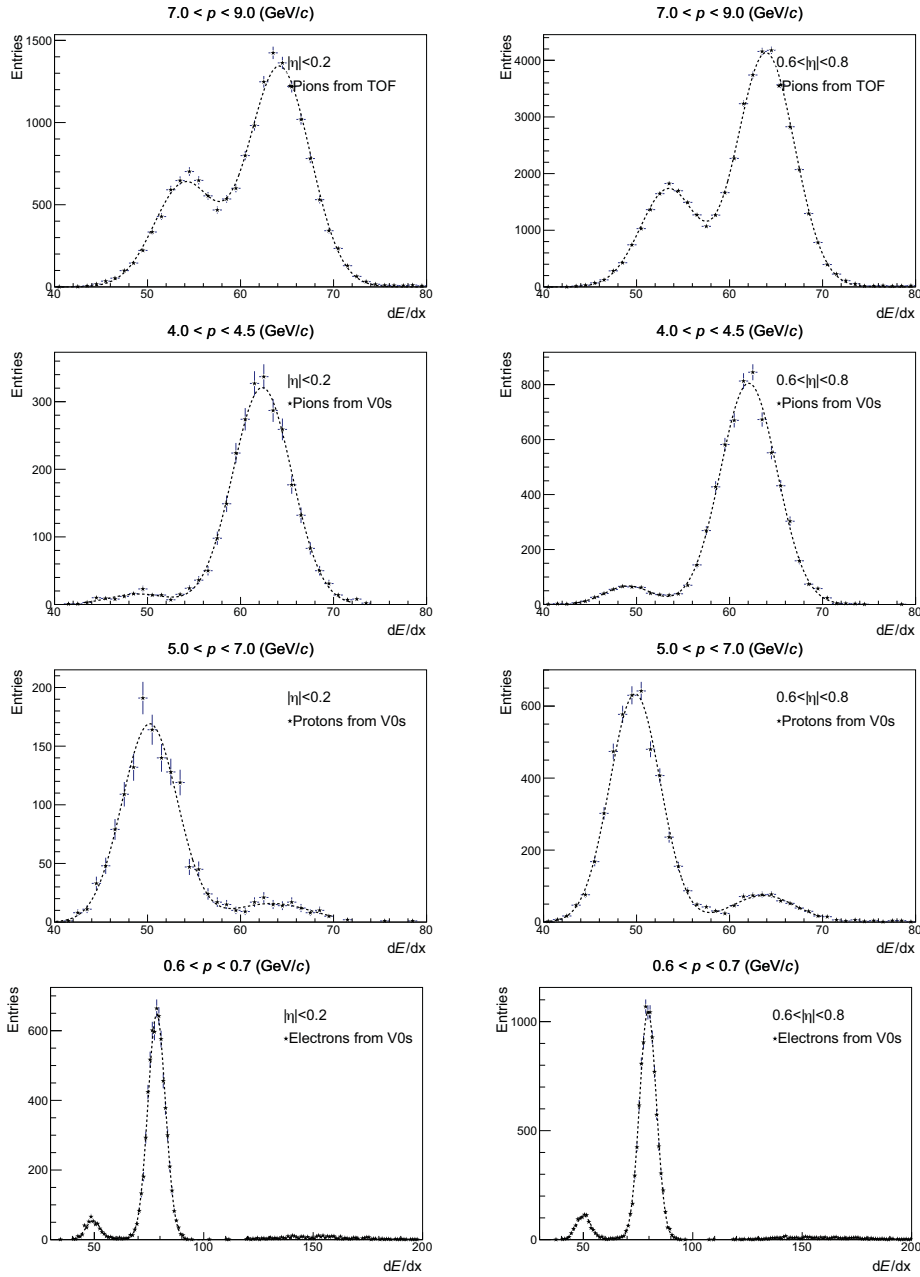


Fig. 3.22 Fit to external particle samples. High momentum pions detected with the TOF,  $dE/dx \approx 60$  (first row). Pions from weak decays of  $K_s^0$ ,  $dE/dx \approx 60$  (second row). Protons from weak decays of  $\Lambda$ ,  $dE/dx \approx 50$  (third row). Electrons from  $\gamma$ -conversion,  $dE/dx \approx 80$  (fourth row). Left(right) column corresponds to  $|\eta| < 0.2$  ( $0.6 < |\eta| < 0.8$ ). These results correspond to MB pp collisions.

### 3.2.5 Particle abundances vs $p$

Just as discussed in Sec. 3.1.2, particle abundances were measured in four different pseudorapidity intervals and a weighted average was computed. In contrast to the low-pt analysis, this

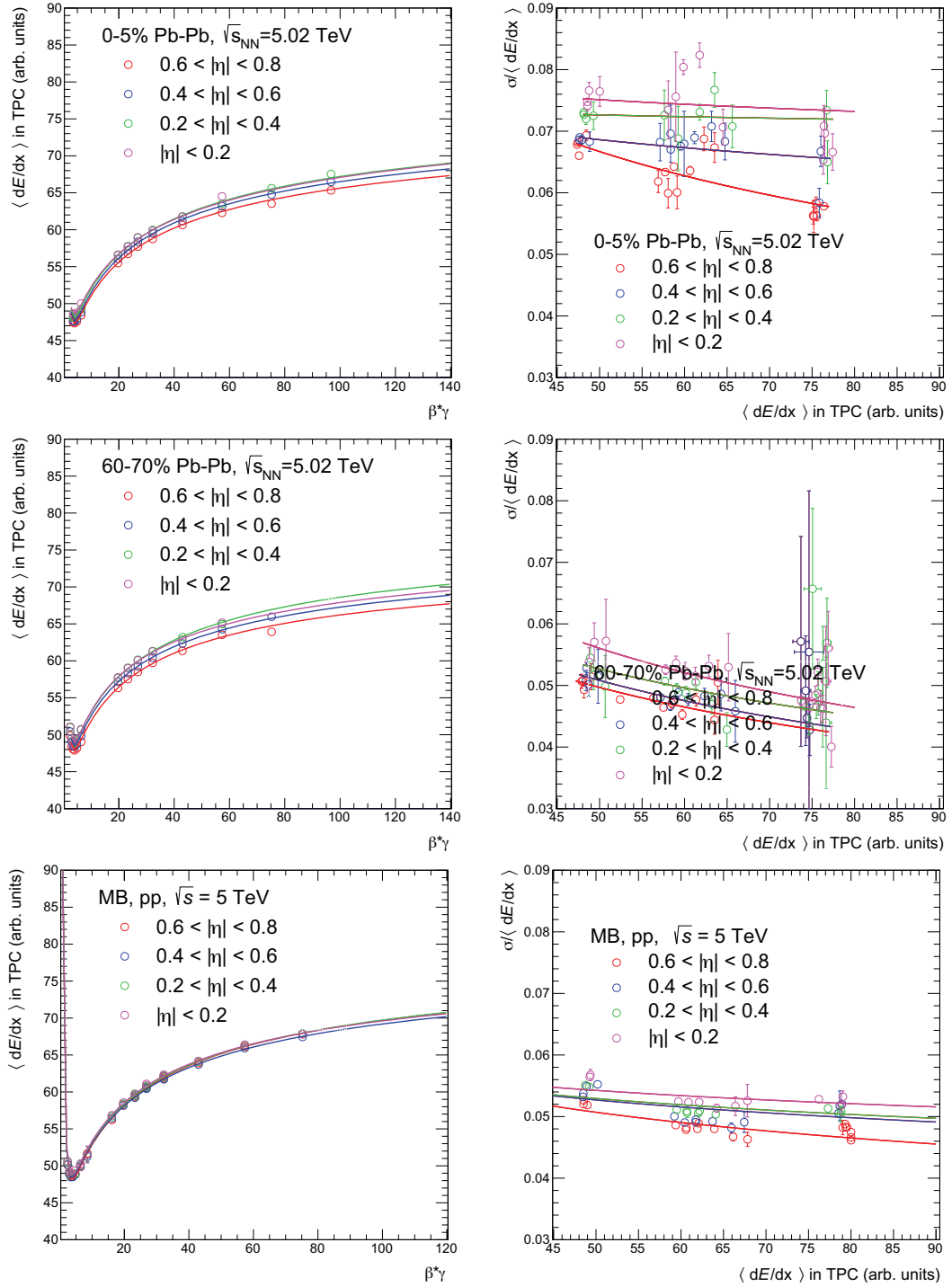


Fig. 3.23 Bethe-Bloch (left) and relative resolution (right) parameterizations for central (top) and peripheral (middle) Pb-Pb collisions. The parameterizations for MB pp collisions are also shown (bottom). Results for the four different pseudorapidity intervals are shown.

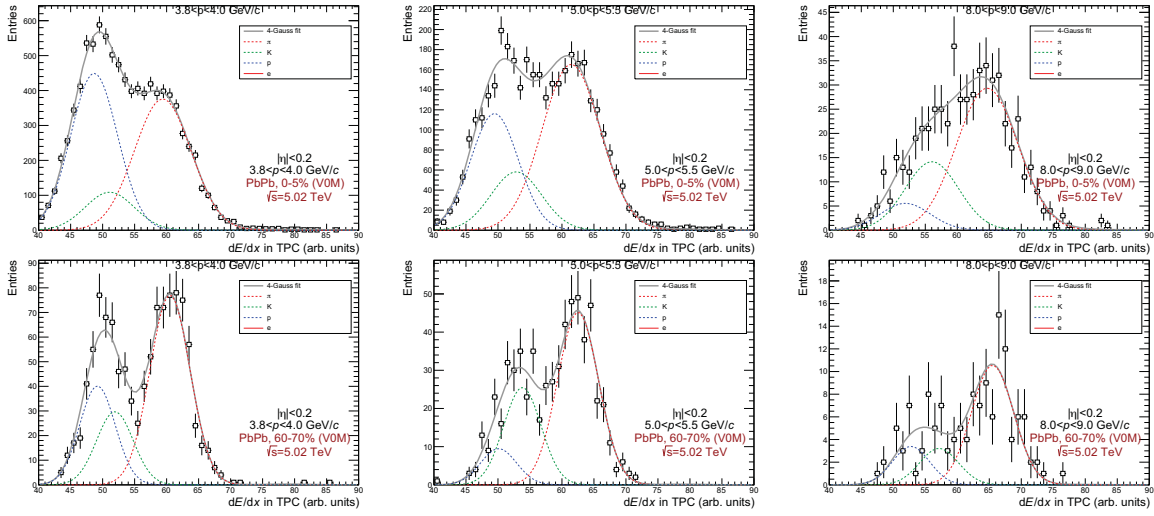


Fig. 3.24 Fit to  $dE/dx$  distributions in Pb–Pb data. Results are shown for tracks within  $|\eta| < 0.2$  and three different momentum intervals (shown in each column). Central collisions (0-5%) and peripheral collisions (60-70%) are displayed in the top-row and bottom-row, respectively.

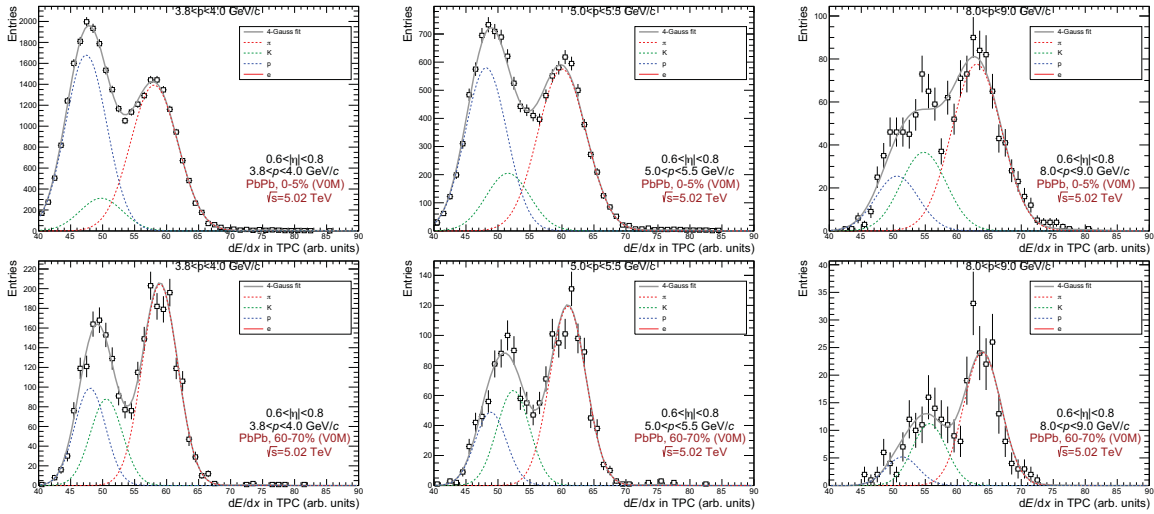


Fig. 3.25 Fit to  $dE/dx$  distributions in Pb–Pb data. Results are shown for tracks within  $0.6 < |\eta| < 0.8$  and three different momentum intervals (shown in each column). Central collisions (0-5%) and peripheral collisions (60-70%) are displayed in the top-row and bottom-row, respectively.

analysis measures the particle abundances as a function of momentum. Consequently, the abundances are further converted to be plotted as a function of  $p_T$ . The results for Pb–Pb and MB pp collisions are found in Fig. 3.27. Albeit previous measurements of identified

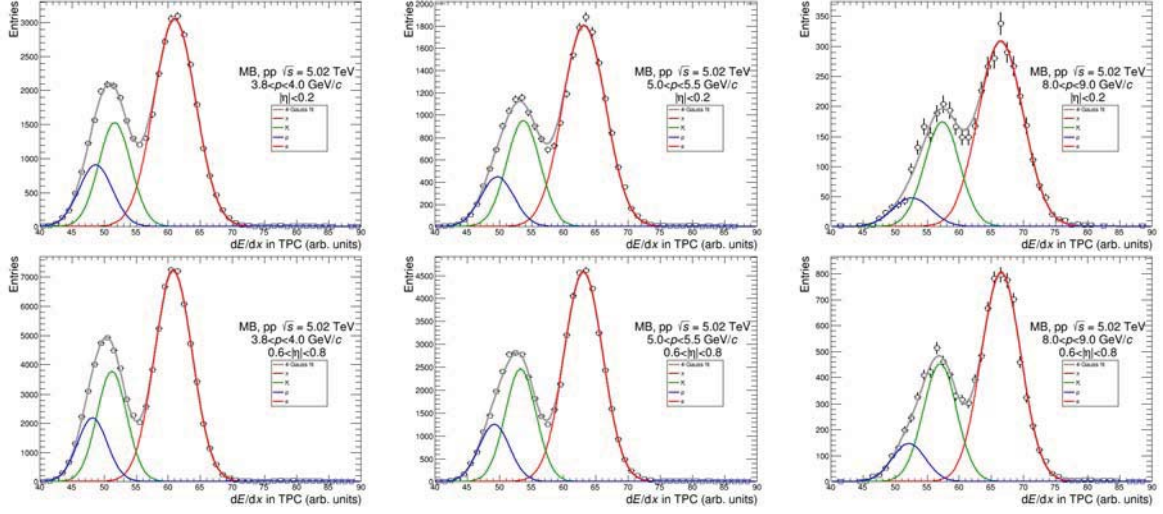


Fig. 3.26 A sum of four Gaussian distributions was used to fit the  $dE/dx$  distribution. Results for two pseudorapidity intervals are shown,  $|\eta| < 0.2$  (top-row) and  $0.6 < |\eta| < 0.8$  (bottom-row) and three different momentum intervals. These results correspond to MB pp collisions.

charged particles in Pb–Pb collisions at  $\sqrt{s_{NN}} = 2.76$  TeV went up to 20 GeV/c, this study is limited up to 12 GeV/c in order to avoid large statistical fluctuations. Within statistical uncertainties, the results for the different pseudorapidity intervals are consistent. It is important to mention that for the analysis of Run1 Pb–Pb data, the parameterization of the BB used extra constraints given by the  $K_S^0$  yields, this information significantly improved the description of the  $dE/dx$  spectra in the region close to the proton MIPs (protons with momentum around 3 GeV/c) where for central events radial flow or recombination may increase the proton yield with respect to pions. In Run1 results, it was reported that the inclusion of  $K_S^0$  information affected the measurements of kaons and protons with momentum below 6 GeV/c and that this effect is large for the most central collisions. Following the ideas reported in [57, 58], Fig. 3.29 shows the particle abundances for central collisions before and after the inclusion of the  $K_S^0$  information.

### 3.2.6 Particle abundances vs $p_T$

Since the identification is done in the variable of particle momentum it is necessary to transform the results to the transverse momentum variable. This is achieved by means of the following equation

$$f_{\pi/K/p}(p_T^j) = \sum_i f_{\pi/K/p}(p^i) R_{p_T^j p^i} \quad (3.13)$$



where,  $p_T^j(p^i)$  is the  $j(i)$ -th transverse momentum(momentum) value.  $R_{p_T^j p^i}$ , is a response matrix and provides a measure of the probability that a track with a given  $p_T^j$  value corresponds to a measured value of  $p^i$ .  $f_{\pi/K/p}(p^i)$  corresponds to the fraction of  $\pi/K/p$  at the given value of  $p^i$ . The effect of the conversion can be seen in Fig. 3.27. In addition Fig. 3.28, shows two examples of the employed response matrices ( $R_{p_T^j p^i}$ ) for the centrality class 0-5%.

### 3.2.7 Uncorrected $p_T$ spectra

The process to obtain the  $p_T$  spectra was accomplished as discussed in Sec. 3.1.3. The exchange of the pseudorapidity dependence for a rapidity dependence was done as explained in Sec. 3.1.4.

### 3.2.8 Corrections

The  $\pi/K/p$   $p_T$  spectra were only corrected for tracking efficiency. Such correction is the same as the one applied to correct the low- $p_T$  spectra (see Sec. 3.1.5). Further corrections, such as GEANT3/GEANT4 and Geant-Fluka are negligible in the high  $p_T$  region.

### 3.2.9 Systematic uncertainties

As it was discussed in Sec. 3.1.3, the systematic uncertainties associated with the PID and the ones associated with the event/track selection can be factorized into two different components (see Eq. 3.8). The systematic errors associated with the event/track selection were described in Sec. 3.1.7. In the following, a discussion about systematic errors associated with the PID is developed.

### 3.2.10 Systematic uncertainty on the extraction of the particle abundances

It was mentioned in Sec. 3.2.3 that the final parameterizations of the BB and resolution curves were obtained from external particle samples plus a two-dimensional fit of the  $dE/dx$  vs.  $p$  distribution of primary particles. Actually, for each system, Pb–Pb (9 centrality bins) and MB pp collisions, 4 parameterizations corresponding to each  $\eta$ -interval were constructed. Consequently, the imprecise knowledge of both curves accounts for the most significant source of the overall systematic uncertainty. In fact, the imprecise knowledge has repercussions on the description of the  $dE/dx$  for a given momentum interval since the values of  $\langle dE/dx \rangle$  and  $\sigma_{\langle dE/dx \rangle}$  were fixed (see Sec. 3.2.4). Therefore, to quantify the magnitude

of the uncertainty, the relative variations of the  $\langle dE/dx \rangle$  ( $\sigma_{\langle dE/dx \rangle}$ ) with respect to the final parameterizations as a function of  $\beta\gamma$  ( $\langle dE/dx \rangle$ ) for the four  $\eta$ -intervals were measured. These results are summarized in Fig. 3.31 (for the Pb–Pb analysis, the relative variations for all the centrality classes have been superimposed). For both quantities, the projections along the  $y$ -axis of the relative variations in intervals of  $\beta\gamma$  and  $\langle dE/dx \rangle$ , respectively, were obtained. For each projection, the RMS values give a measure of the dispersion and they were used to parameterize the overall relative deviation. The parameterization was accomplished with a fit to the RMS values. Figure 3.30 (Fig. 3.31) shows the results for Pb–Pb (MB pp). For both systems, Pb–Pb and MB pp collisions, the region between 2 and 6 of  $\beta\gamma$  corresponds to that of the proton MIPs where the maximum deviations are seen, for such reason, the region between 2 and 20 of  $\beta\gamma$  was parameterized using a second-degree polynomial while in the interval above 20, an exponential function was used. To describe the overall range of the resolution in both systems, an exponential function was used. In general, the employed parameterizations are capable to describe the relative deviations.

Using the parameterizations just mentioned, the values of the  $\langle dE/dx \rangle$  and  $\sigma_{\langle dE/dx \rangle}$  were varied randomly in the intervals  $\langle dE/dx \rangle(1 + \alpha \langle dE/dx \rangle_{var})$  and  $\langle \sigma \rangle(1 + \lambda \langle \sigma \rangle_{var})$ , respectively. The values of  $\langle dE/dx \rangle_{var}$  and  $\langle \sigma \rangle_{var}$  were obtained evaluating the respective parameterizations while  $\alpha$  and  $\lambda$  are random numbers in  $[-1, 1]$ . This exercise allowed to variate the values of the  $\langle dE/dx \rangle$  and  $\sigma_{\langle dE/dx \rangle}$  employed to fit the  $dE/dx$  distributions. Actually, the fitting process was repeated 1000 times and therefore the measurement of the particle abundances as a function of transverse momentum was done 1000 times for the four different pseudorapidity intervals (see Sec. 3.2.5 for the technique used to measure the particle abundances). For every transverse momentum bin corresponding to a pseudorapidity interval, the dispersion of the measured particle abundances was quantified with the RMS values. Figures 3.32, 3.33, 3.34 show the 1000-entries abundance distributions for pions, kaons, and protons for selected momentum intervals in the pseudorapidity intervals  $|\eta| < 0.2$  and  $0.6 < |\eta| < 0.8$  for Pb–Pb, respectively. Finally, for every transverse momentum bin, the RMS values among the different pseudorapidity intervals were compared and the PID systematic uncertainty was taken as the maximum.

Figure 3.38 shows the summary of the systematic uncertainties in the relativistic rise analysis for two different centrality classes as well as the results for MB pp collisions.

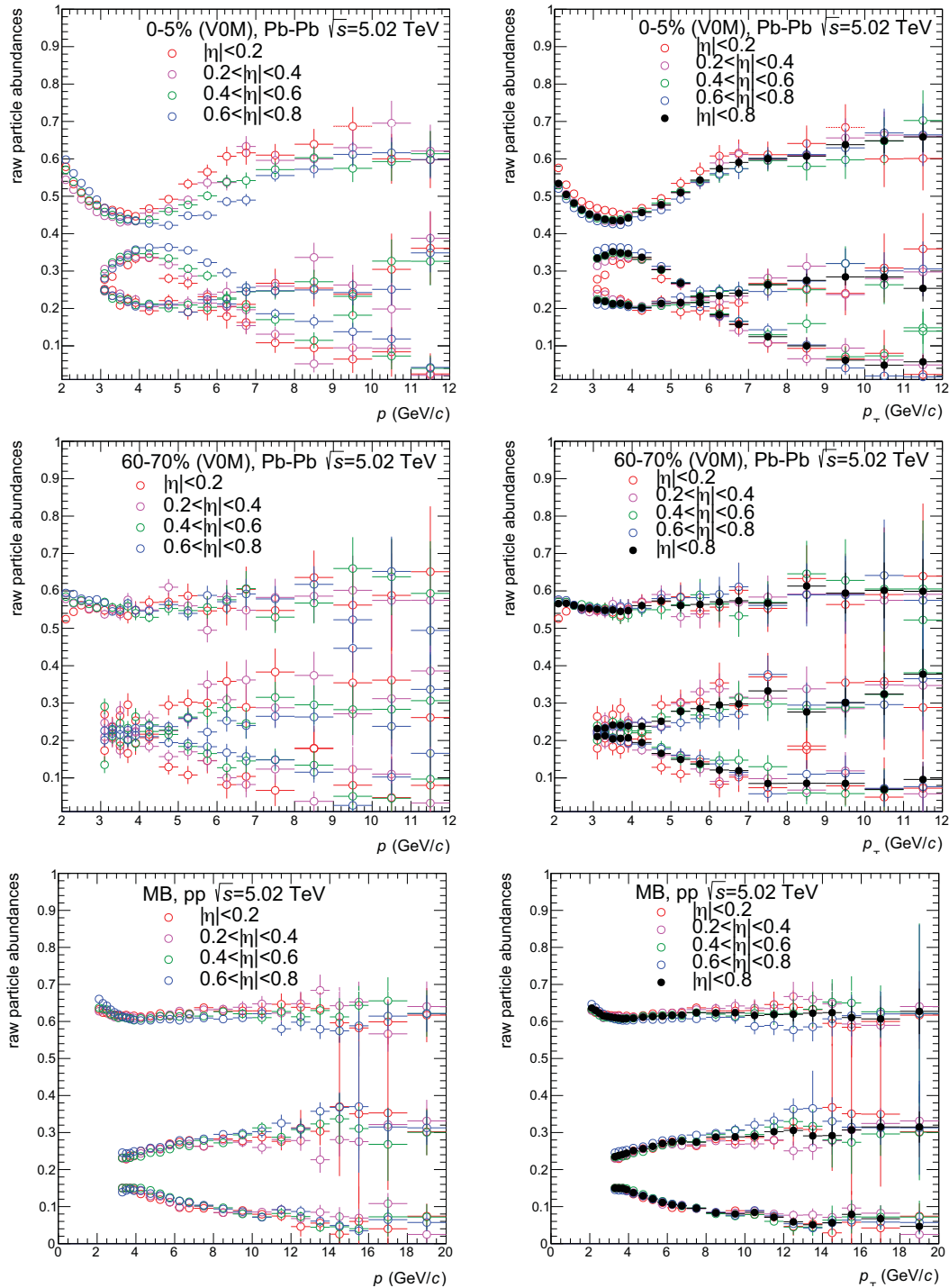


Fig. 3.27 Particle abundances of charged pions, kaons and protons as a function of momentum (left column) and transverse momentum (right column). Two centrality classes are shown: 0-5% (upper-row) and 60-70% (middle-row). Similar plots are shown for MB pp collisions (bottom-row). Results for different pseudorapidity intervals are shown (open circles) as well as the weighted average corresponding to  $|\eta| < 0.8$  (full markers).

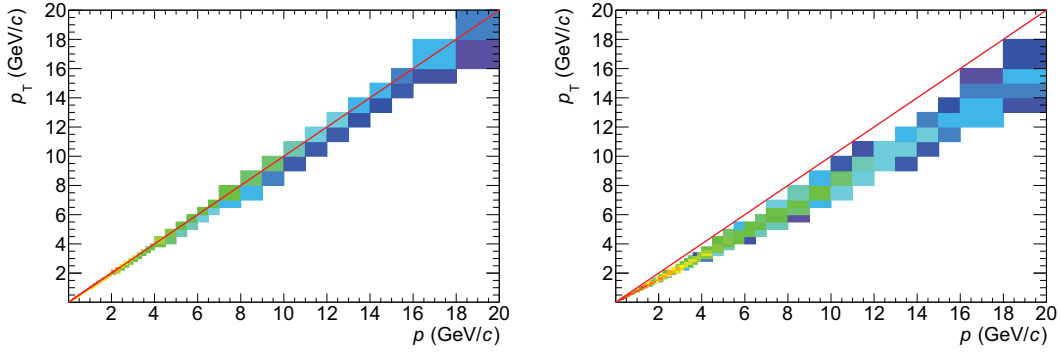


Fig. 3.28 Response matrices. Correlation between transverse momentum and momentum. The examples correspond to central collisions (0-5%). Left(right) plot is associated to tracks in  $|\eta| < 0.2$  ( $0.6 < |\eta| < 0.8$ ).

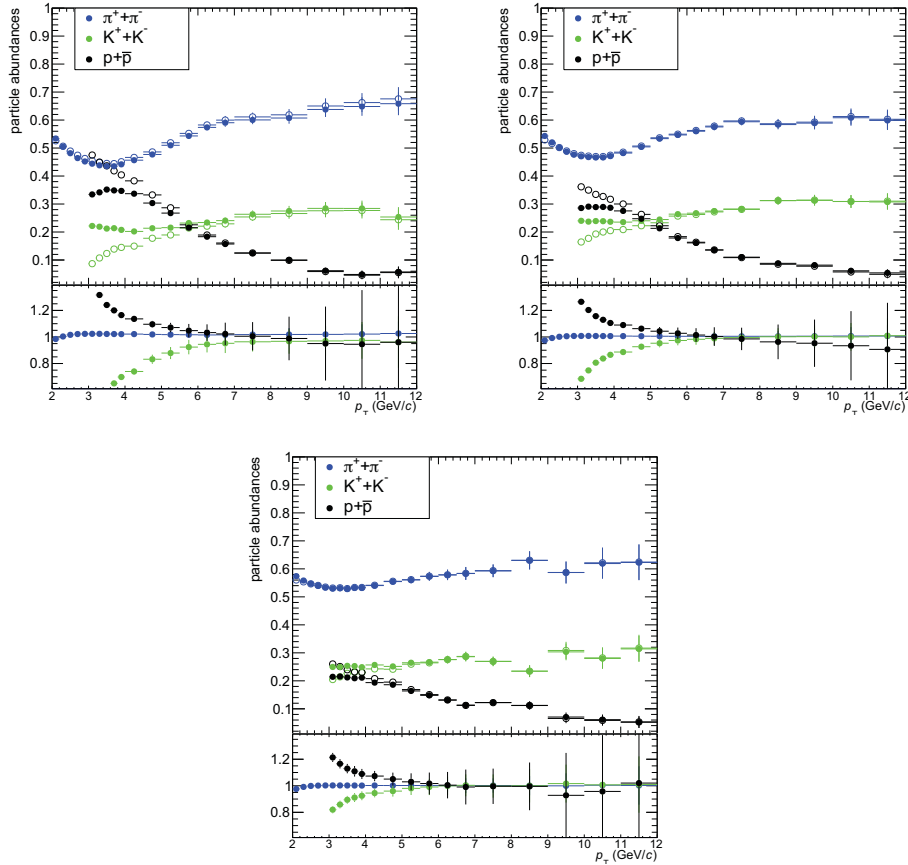


Fig. 3.29 Abundances of charged pions, kaons and protons as a function of  $p_T$  within the pseudorapidity interval  $|\eta| < 0.8$  before(after) the inclusion of  $K_S^0$  are shown as empty(full)markers. In addition, the ratio is plotted. The results are shown for 0-5% (upper-left plot), 20-30% (upper-right plot) and 50-60% (bottom) centrality classes. It was observed that the effect of the inclusion of external samples is about 20% for the most central collisions.

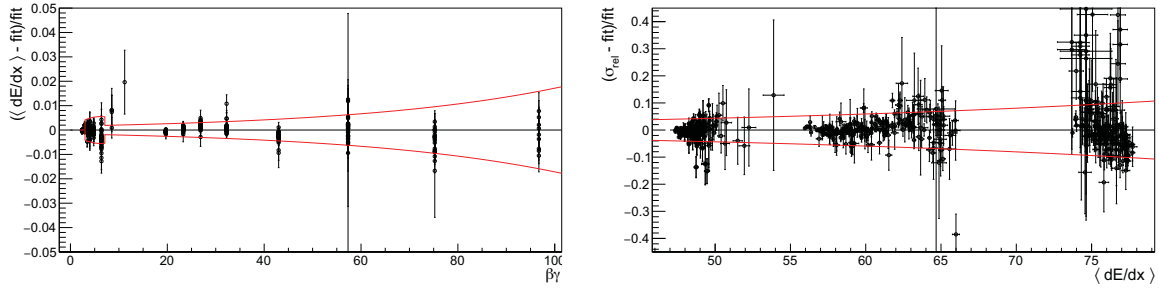


Fig. 3.30 Relative variation of  $\langle dE/dx \rangle$  ( $\sigma$ ) with respect to the original parameterizations as a function of  $\beta\gamma$  ( $\langle dE/dx \rangle$ ). The red solid lines indicate the fits to the RMS used to describe the overall variation. The same variations (red curves) were used for estimating the PID uncertainty in all the centrality classes for Pb–Pb collisions.

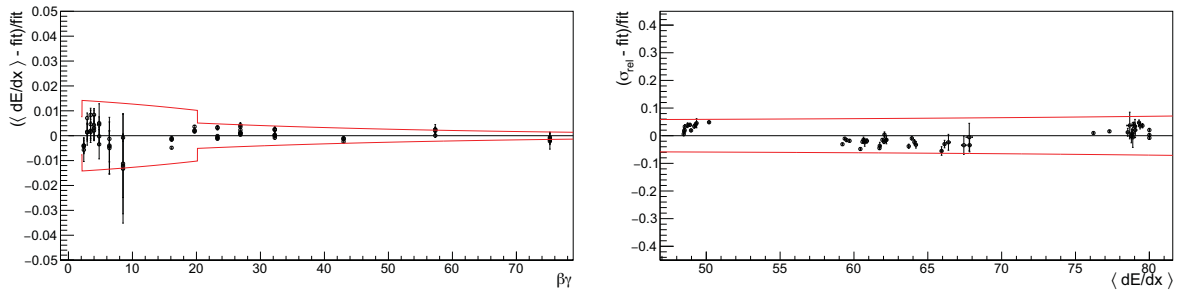


Fig. 3.31 Relative variation of  $\langle dE/dx \rangle$  ( $\sigma$ ) with respect to the original parameterizations as a function of  $\beta\gamma$  ( $\langle dE/dx \rangle$ ). The red solid lines indicate the fits to the RMS used to describe the overall variation. The results shown correspond to MB pp collisions.

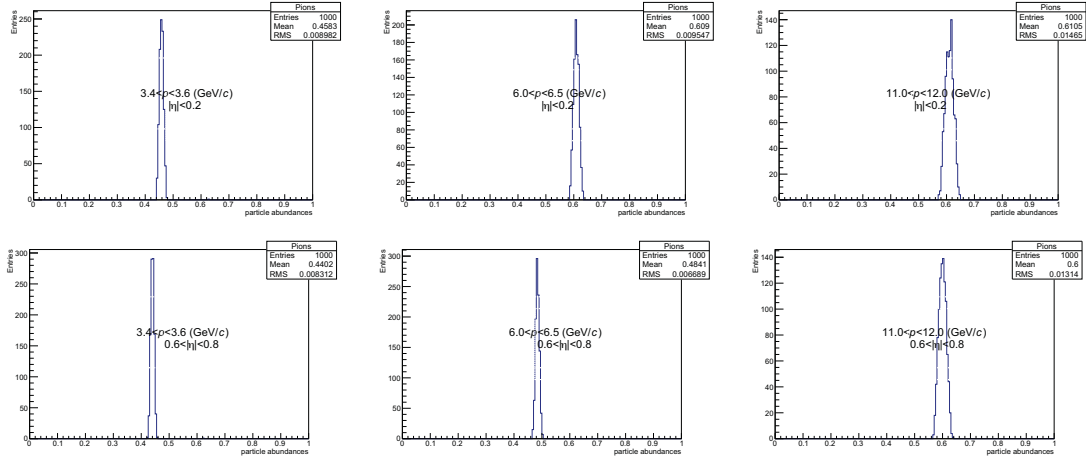


Fig. 3.32 Distribution of particle abundances for pions. Tracks for  $|\eta| < 0.2$  (upper-row),  $0.6 < |\eta| < 0.8$  (bottom-row) and three momentum intervals and are shown. The results correspond to the centrality class 0-5 %, Pb-Pb.

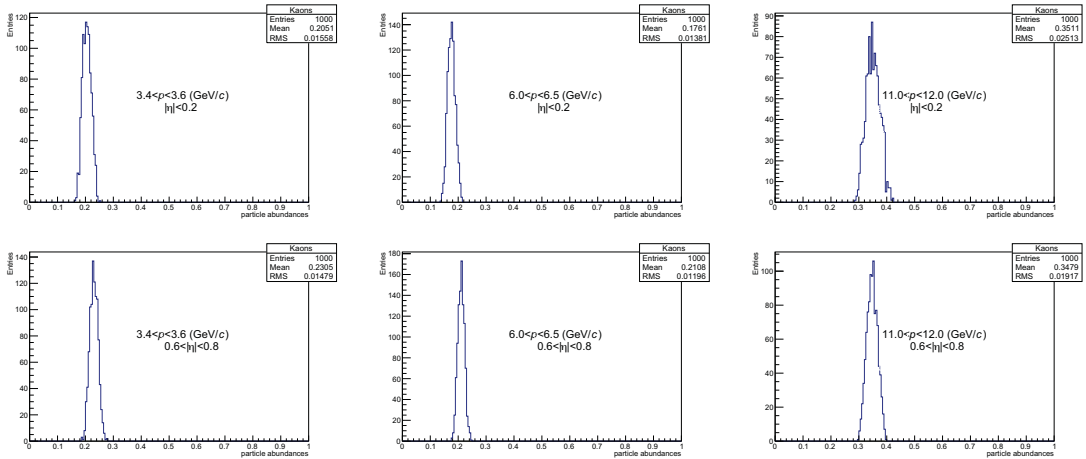


Fig. 3.33 Distribution of particle abundances for kaons. Tracks for  $|\eta| < 0.2$  (upper-row),  $0.6 < |\eta| < 0.8$  (bottom-row) and three momentum intervals and are shown. The results correspond to the centrality class 0-5 %, Pb-Pb.

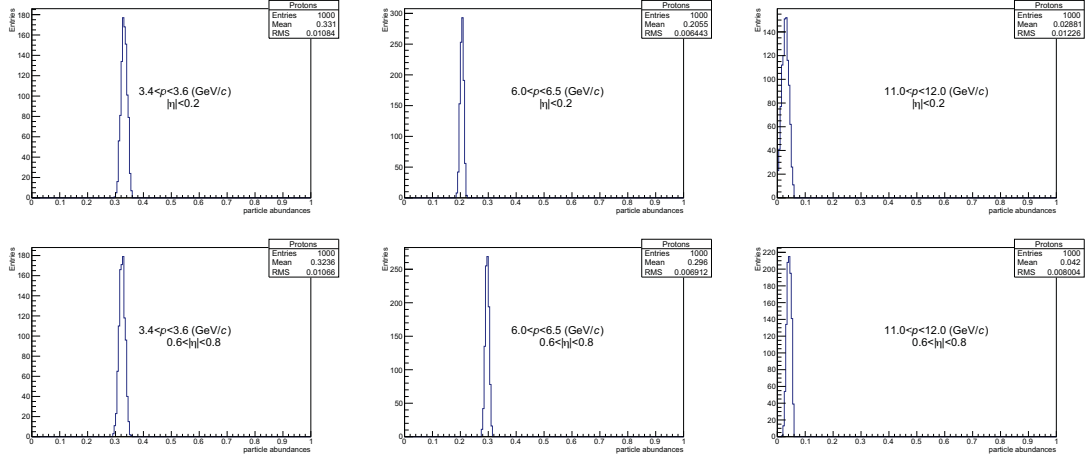


Fig. 3.34 Distribution of particle abundances for protons. Tracks for  $|\eta| < 0.2$  (upper-row),  $0.6 < |\eta| < 0.8$  (bottom-row) and three momentum intervals and are shown. The results correspond to the centrality class 0-5 %, Pb-Pb.

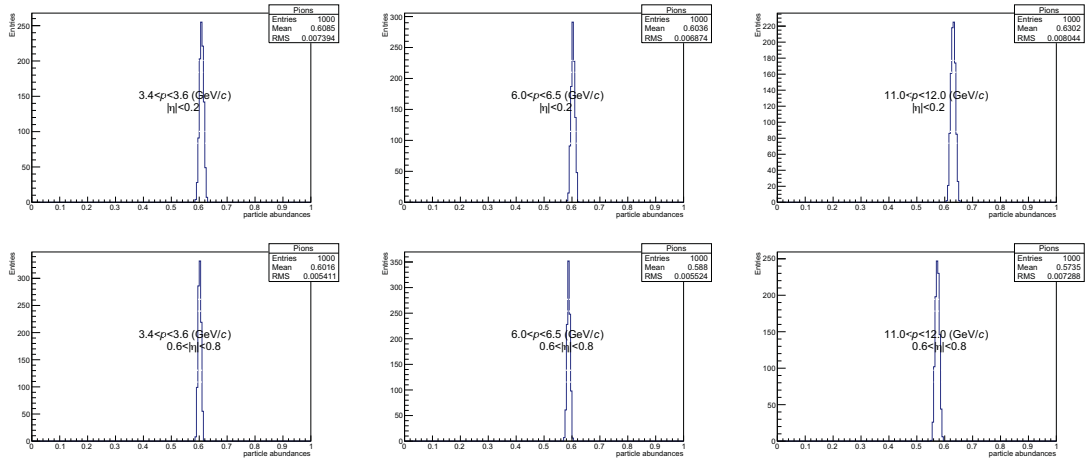


Fig. 3.35 Distribution of particle abundances for pions. Tracks for  $|\eta| < 0.2$  (upper-row),  $0.6 < |\eta| < 0.8$  (bottom-row) and three momentum intervals and are shown. The results correspond to MB pp.

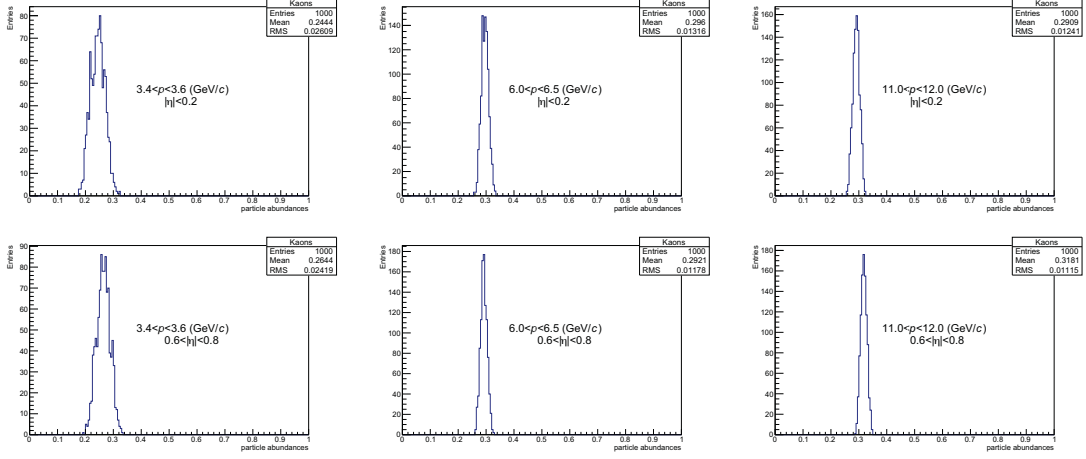


Fig. 3.36 Distribution of particle abundances for kaons. Tracks for  $|\eta| < 0.2$  (upper-row),  $0.6 < |\eta| < 0.8$  (bottom-row) and three momentum intervals and are shown. The results correspond to MB pp.

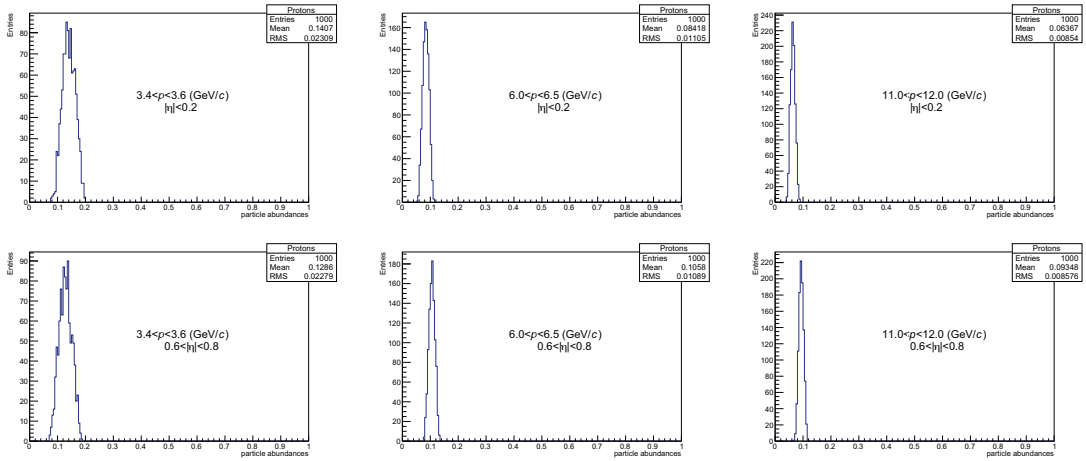


Fig. 3.37 Distribution of particle abundances for protons. Tracks for  $|\eta| < 0.2$  (upper-row),  $0.6 < |\eta| < 0.8$  (bottom-row) and three momentum intervals and are shown. The results correspond to MB pp.



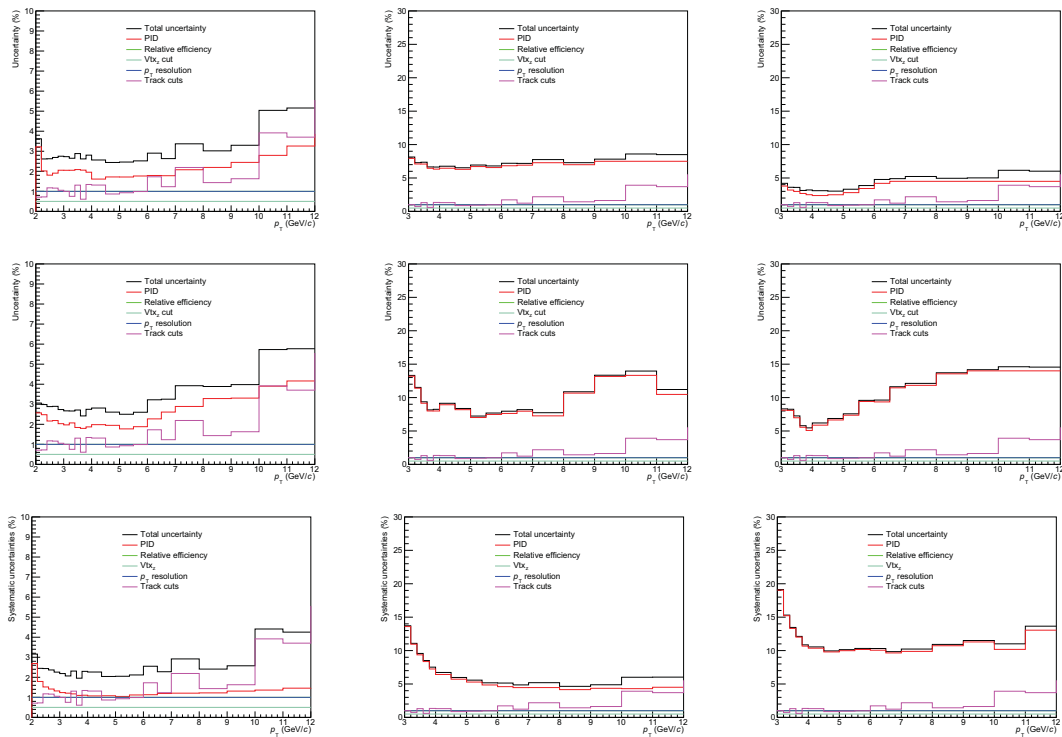


Fig. 3.38 Summary of systematic uncertainties for pions(left), kaons(middle) and protons(right). All the contributions were added in quadrature. Upper-row correspond to the centrality class 0-5%, middle-row to the centrality class 60-70% while the bottom-row is associated to MB pp collisions.

### 3.3 Combined results

The measurement of the production of pions, kaons and (anti)protons in Pb–Pb and pp collisions at  $\sqrt{s_{\text{NN}}} = 5.02$  TeV in ALICE comprises six different and independent analyses. For the combination, the  $p_{\text{T}}$  ranges listed in Tab. 3.4 and Tab. 3.5 have been used for the different Pb–Pb and pp analyses, respectively. The techniques used by the different analyses were previously reported in [17].

<b>Analysis</b>	$\pi$	<b>K</b>	<b>p</b>
<b>ITSsa</b>	0.10–0.70	0.20–0.50	0.30–0.60
<b>TOF</b>	0.60–2.50	1.0–2.50	0.80–4.0
<b>TPC</b>	0.25–0.70	0.25–0.45	0.45–0.80
<b>rTPC</b>	2.0–12.0	3.0–12.0	3.0–12.0
<b>kinks</b>	–	0.20–5.0	–
<b>HMPID</b>	1.50–4.0	1.50–4.0	1.50–6.0

Table 3.4 Transverse momentum ranges in GeV/c for pions, kaons, and protons used in the different Pb–Pb analyses.

<b>Analysis</b>	$\pi$	<b>K</b>	<b>p</b>
<b>ITSsa</b>	0.10–0.70	0.20–0.60	0.30–0.65
<b>TOF</b>	0.60–3.50	0.65–3.50	0.80–4.50
<b>TPC</b>	0.30–0.70	0.30–0.45	0.45–0.80
<b>rTPC</b>	2.0–12.0	3.0–12.0	3.0–12.0
<b>kinks</b>	–	0.45–4.0	–
<b>HMPID</b>	1.50–4.0	1.50–4.0	1.50–6.0

Table 3.5 Transverse momentum ranges in GeV/c for pions, kaons, and protons used in the different pp analyses.

The weighted average has been computed for the superimposed spectrum points in  $p_{\text{T}}$  taking into account only the uncommon systematic and statistical uncertainties (summed in quadrature) as weights. The common systematic uncertainties are associated to the ITS-TPC matching efficiency and to the  $|V_z| < 10$  cm event selection cut. These two common uncertainties were summed in quadrature once the combining procedure finished. In addition, points with statistical uncertainty larger than 30% have been cut off. This means, points above 10 GeV/c and 7 GeV/c for the 70–80% and 80–90% centrality classes have been removed, respectively. Figure 3.39 and Fig. 3.40 show the ratio to the combined measurement for the different analyses. Overall, there is good agreement among the different analyses.

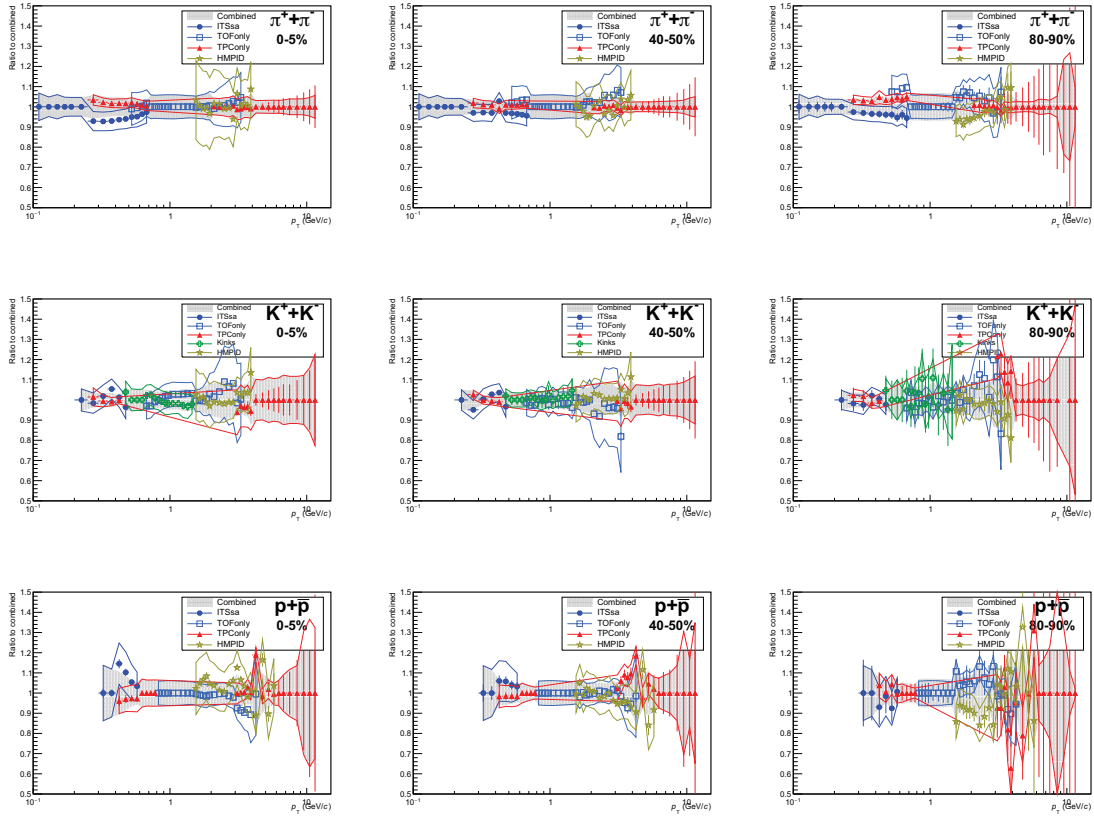


Fig. 3.39 Ratio to combined spectra for all the analyses. Results are shown for central (0-5%), semi-peripheral (40-50%), and peripheral (80-90%) Pb–Pb collisions.

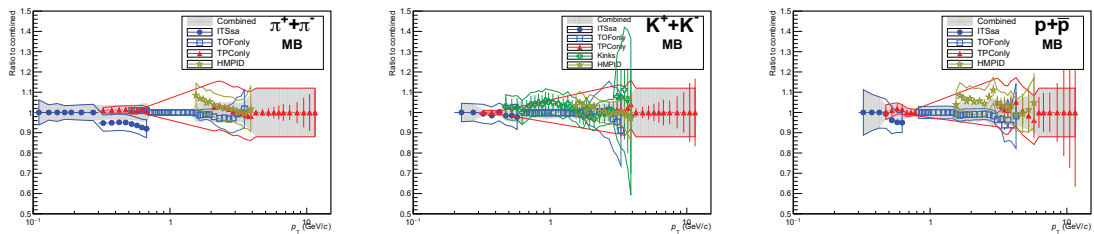


Fig. 3.40 Ratio to combined spectra for all the analyses. Results are shown for MB pp collisions.

# Chapter 4

## Results and discussions

The present chapter is devoted to discussing a set of results, which have been derived from the measurement of the transverse momentum spectra of pions, kaons, and protons. The overall discussion has been divided into two sections. The former, aimed to review the so-called *soft physics* grounds, focussing on the bulk matter properties and the dynamical evolution of the system in Pb–Pb collisions. The latter section concentrates on testing the *hard probes*, results on particle suppression and the scaling properties of the fractional momentum loss with energy density and path-length are presented.

### 4.1 Soft physic

Ultrarelativistic heavy-ion collisions create a state of matter featured by the deconfinement of hadrons into a strongly-interacting quark-gluon-plasma (sQGP) [3, 4], which rapidly expands and thermalizes [60]. As the thermalized QGP system continues to expand it cools down till its temperature drops down below the *critical temperature* of the QCD transition  $\approx 160$  MeV [61, 62], at which point it hadronizes. The *chemical freezeout* [9] is presumably the stage in which the overall particle composition is approximately fixed. Although particle composition is relatively fixed and hadrons continue to interact, their energy is below the inelastic production threshold and only their momentum distributions are modified. The stage in which the final hadrons cease interacting and decouple from the system is characterized by the *kinetic freezeout temperature*. At the kinetic freezeout, the momenta of the hadrons is fixed. The initial state of the heavy-ion collision can be described using the so-called Color Glass Condensate (CGC) framework [63]. However, as it is not possible to directly detect the QGP, the investigation of the properties of the QGP relies mostly on observables based on the measurement of final state hadrons and comparisons with models. Such observables include the centrality dependence of the transverse momentum distributions of identified charged

particles and the proton-to-pion ratio, which are used to quantify radial flow effects [9]. In contrast to central collisions, where radial flow effects are relevant, anisotropic flow in non-central collisions, which is quantified by the elliptic ( $v_2$ ), triangular ( $v_3$ ) and quadrangular ( $v_4$ ) flow coefficients becomes significant for hadrons having transverse momentum below 5 GeV/c [47]. Anisotropic flow, which is caused by the presecense of anisotropic pressure gradients, developed in the initial spatial anisotropy of the two colliding nuclei then transforms into an observed momentum anisotropy, leading to an anisotropic particle distribution  $dN/d\phi$  [48].

### 4.1.1 Transverse momentum spectra

Figure 4.1 shows the transverse momentum spectra of charged pions, kaons, and protons for ten centrality classes. Going from peripheral to central collisions, a hardening of the spectral shapes is observed at  $p_T < 2$  GeV/c. This is a mass-dependent effect, which is more significant for protons. The observed behavior is consistent with the expected effects due to radial flow [9]. A similar example of a behaviour dominated by radial flow is visualized in Fig. 4.2 where the centrality dependence of the proton-to-pion ratio as a function of transverse momentum in Pb–Pb collisions at  $\sqrt{s_{NN}} = 5.02$  TeV is shown. The ratio exhibits a maximum of  $\approx 0.85$  ( $\approx 0.38$ ) around the value of 3 GeV/c for central(peripheral) collisions and then decreases with increasing  $p_T$ . Furthermore, at the LHC energies, these values are approximately 20% above the maximums observed by RHIC experiments [64, 5]. In the intermediate  $p_T$  region ( $2 \lesssim p_T \lesssim 8$  GeV/c), the enhancement of the proton-to-pion ratio in Pb–Pb collisions at  $\sqrt{s_{NN}} = 5.02$  TeV is similar to the observed in Pb–Pb collisions at  $\sqrt{s_{NN}} = 2.76$  TeV, however, in the former case, the peak around 3 GeV/c is shifted toward higher values of  $p_T$  for the most central collisions, which could be attributed to stronger radial flow effects. In the letter [10], it was reported that models based on parton recombination [11–13] could describe the shape and strength of the baryon-to-meson ratio. Moreover, the baryon-to-meson ratio follows the same trend for all the centrality classes, hence, to elucidate the rank of suppression, the  $p_T$ -integrated particle ratios as a function of  $\langle dN_{ch}/d\eta \rangle$  for pions, kaons, and protons is computed. Figure 4.3 shows that within uncertainties, weak centrality dependence of the  $p_T$ -integrated kaon-to-pion and proton-to-pion ratio is observed. Similar results were observed in Pb–Pb collisions at  $\sqrt{s_{NN}} = 2.76$  TeV [59].

In order to quantify the radial flow strength, a Blast-Wave model introduced by Schnederman *et al.* [14] was employed. A combined fit with a blast-wave function has been performed. The functional form of the model is given by

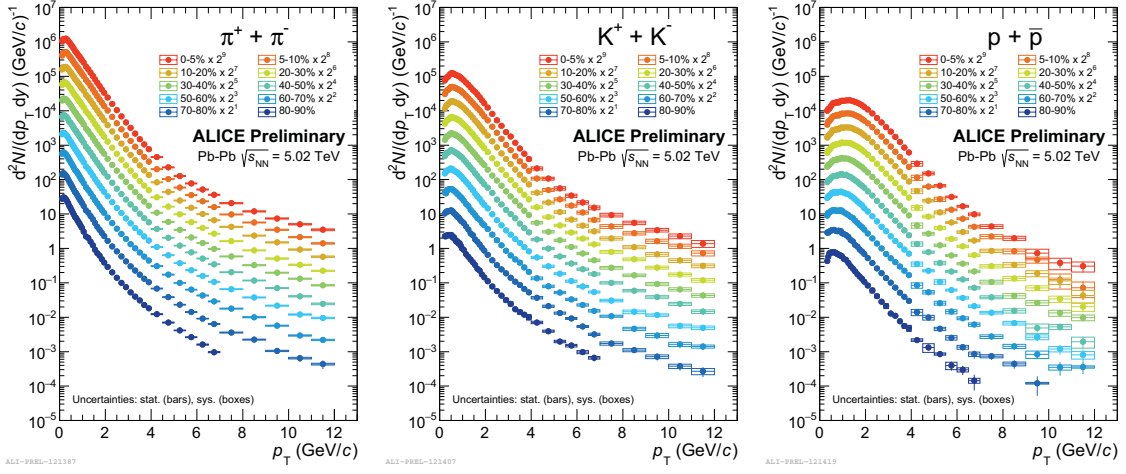


Fig. 4.1 Transverse momentum spectra of pions (left), kaons (middle), and protons (right) from Pb–Pb collisions at  $\sqrt{s_{NN}} = 5.02$  TeV for different centrality classes. Statistical and systematic uncertainties are displayed as bars and boxes, respectively.

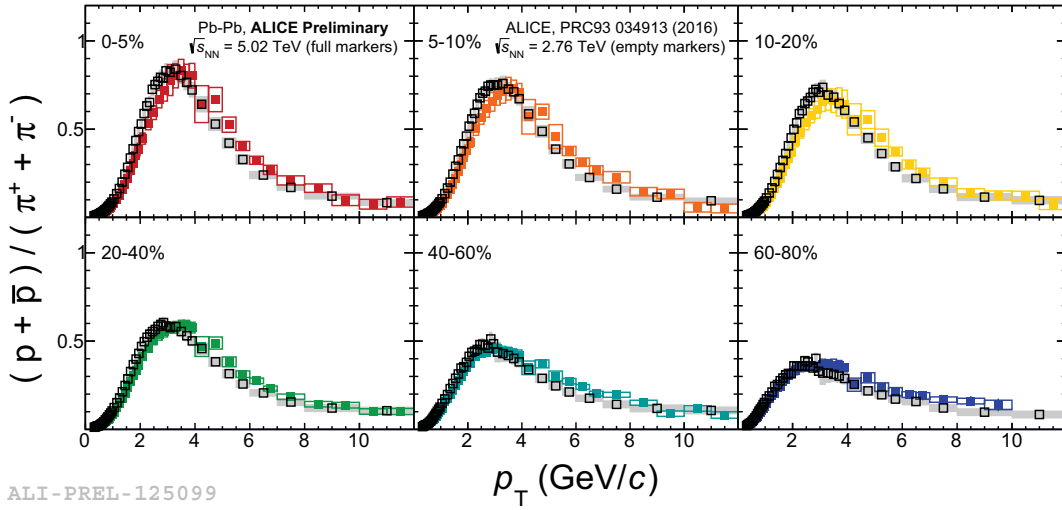


Fig. 4.2 Proton-to-pion ratio of transverse momentum spectra for different centrality classes. The most central (peripheral) collisions are displayed in the top-left (bottom-right) corner. Only PID systematic error are being displayed as the common part cancels out.

$$\frac{1}{p_T} \frac{dN}{dp_T} \propto \int_0^R m_T I_0 \left( \frac{p_T \sinh \rho}{T_{\text{kin}}} \right) K_1 \left( \frac{m_T \cosh \rho}{T_{\text{kin}}} \right) r dr, \quad (4.1)$$

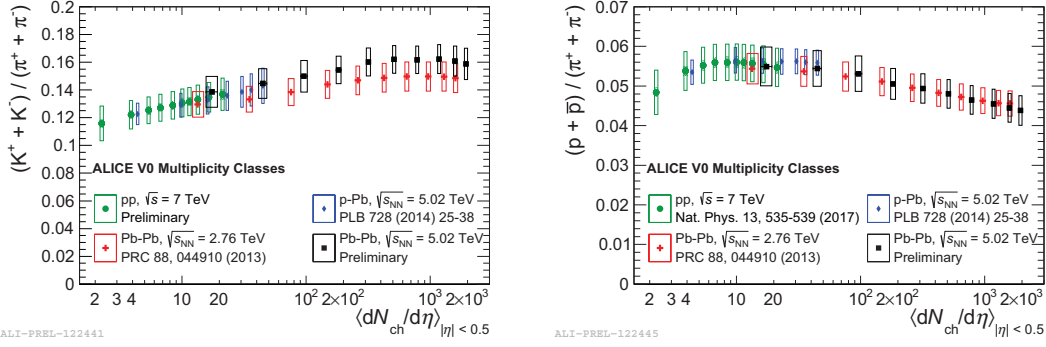


Fig. 4.3 Ratios of the  $p_T$ -integrated yields as function of the mean charged particle density. Left panel: the kaon-to-pion ratio. Right panel: the proton-to-pion ratio. Statistical and PID systematic uncertainties are plotted as vertical error bars and boxes around the points, respectively.

where  $I_0$  and  $K_1$  are the modified Bessel functions,  $\rho = \tanh^{-1}(\beta_T) = \tanh^{-1}\left(\left(\frac{r}{R}\right)^n \beta_s\right)$ , where  $r$  is the radial distance from the center of the fireball in the transverse plane,  $R$  is the radius of the fireball,  $\beta_s$  is the transverse expansion velocity at the surface and  $n$  is the exponent of the velocity profile.  $T_{kin}$ ,  $\beta_T$ , and  $n$  are free parameters of the fit. As the values of the free parameters are sensitive to the fit range for charged pions due to the large contribution from resonance decays (mostly at low  $p_T$ ), which tend to reduce  $T_{kin}$ , the  $p_T$  ranges 0.5-1 GeV/c, 0.2-1.5 GeV/c and 0.3-3 GeV/c were used for pions, kaons, and protons, respectively. Figure 4.4 (left) shows the data-fit ratio in which a better agreement is seen for central events. Figure 4.4 (right) shows the correlation between  $\langle\beta_T\rangle$  and  $T_{kin}$ . The color scale is associated with the mean density multiplicity at midrapidity. It can be seen that going from peripheral to central Pb–Pb collisions the  $\langle\beta_T\rangle$  ( $T_{kin}$ ) increases (decreases). This is in agreement with the assumption of a linear dependence of the transverse velocity on the radius of the fireball. Moreover for the most central Pb–Pb collisions the radial flow ( $\langle\beta_T\rangle$ ) is found to be higher in 5.02 TeV than in 2.76 TeV Pb–Pb collisions. For central collisions, the temperature at the kinetic freeze–out is below the expected value for the QCD phase transition ( $\approx 157$  MeV/c)[15]. Therefore, the results could give indirect evidence of the existence of a hadronic gas phase within the severe limitations of the blast-wave model.

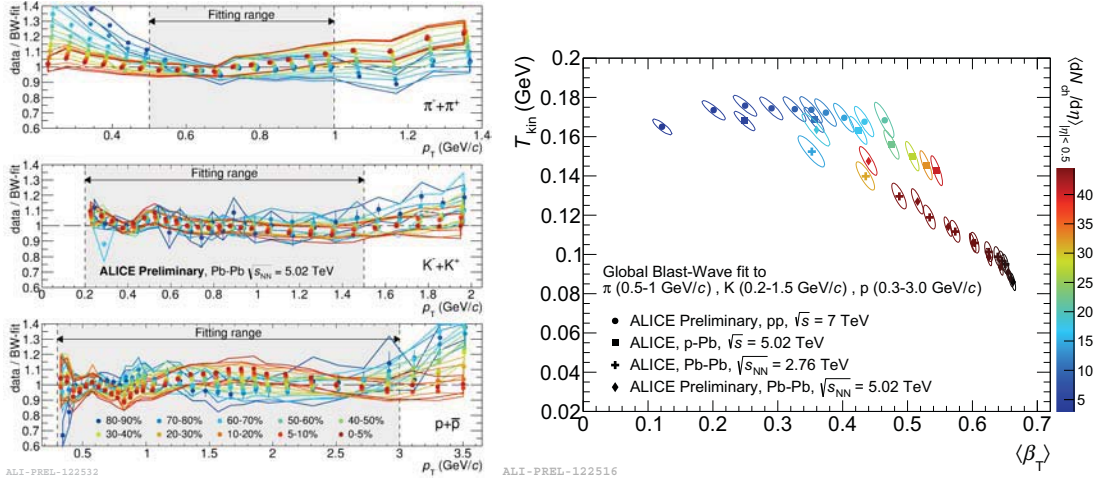


Fig. 4.4 (Left) The transverse momentum distributions of charged pions (top), kaons (middle), and protons (bottom) normalized to the corresponding blast-wave functions, different centralities are shown. (Right)  $T_{\text{kin}}$  vs  $\langle\beta_T\rangle$  results of the Blast-Wave analysis, results for Pb-Pb at  $\sqrt{s_{\text{NN}}} = 5.02$  TeV are represented as rhombs for different collision centralities. The color scale represents the mean multiplicity density in  $|\eta| < 0.5$  for different colliding systems.

## 4.2 Hard processes

### 4.2.1 Nuclear modification factor

Effects such as energy loss or jet quenching of a hard probe [16] induced by its propagation throughout the QGP can be experimentally addressed by means of the nuclear modification factor  $R_{AA}$  [17]. It implies that if medium effects were absent in nuclei collisions (A-A), such interactions would be explained as superposition of a certain number of binary nucleon-nucleon interactions. The functional form of the nuclear modification factor reads [17]

$$R_{AA} = \frac{d^2 N_{\text{id}}^{\text{AA}} / dy dp_T}{\langle T_{AA} \rangle d^2 \sigma_{\text{id}}^{\text{pp}} / dy dp_T} \quad (4.2)$$

where  $N_{\text{id}}^{\text{AA}}$  and  $\sigma_{\text{id}}^{\text{pp}}$  are the charged particle yield in nucleus-nucleus (A-A) collisions and the cross section in pp collisions, respectively, and  $\langle T_{AA} \rangle$  is the nuclear overlap function. The nuclear overlap function is obtained from a Glauber model [18] and is related to the average number of binary nucleon-nucleon collisions ( $N_{\text{coll}}$ ) and the inelastic nucleon-nucleon cross section as  $\langle T_{AA} \rangle = \langle N_{\text{coll}} \rangle / \sigma_{\text{inel}}^{\text{NN}}$ . Figure 4.5 shows the centrality dependence of the nuclear modification factor as a function of transverse momentum. Results show that for



any centrality class and  $p_T > 4$  GeV/c, the  $R_{AA}$  of mesons share both, qualitatively and quantitatively behavior while for protons with  $p_T$  below 4 GeV/c, the effects of radial flow and recombination still present. Furthermore in a letter by ALICE [19], it was reported that the  $R_{AA}$  of pions, kaons, and protons with  $p_T$  above 10 GeV/c is the same for all the species and the suppression was largest in the most central collisions.

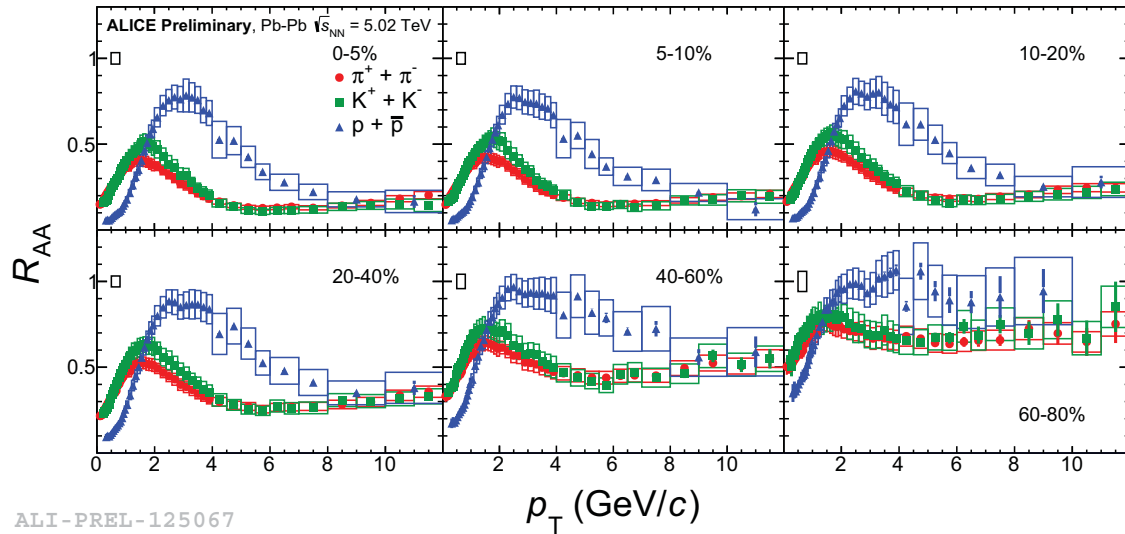


Fig. 4.5 Nuclear modification factor as a function of transverse momentum for pions, kaons, and protons. Going from the upper-left corner to the bottom-right corner, the centrality class goes from the central to peripheral collisions. Statistical and PID systematic uncertainties are plotted as vertical error bars and boxes around the points, respectively.

#### 4.2.2 Energy density and path-length dependence of the fractional momentum loss

The current section is based on the results reported in [25].

In this work, the usage of the inclusive charged particle suppression data to get an alternative estimate of the jet-quenching effects is explored by means of the fractional momentum loss proposed by the PHENIX Collaboration [65]. This because there are some effects which can affect our interpretation of energy loss from  $R_{AA}$  measurements. For instance, while energy loss increases with increasing  $\sqrt{s_{NN}}$  which would tend to decrease

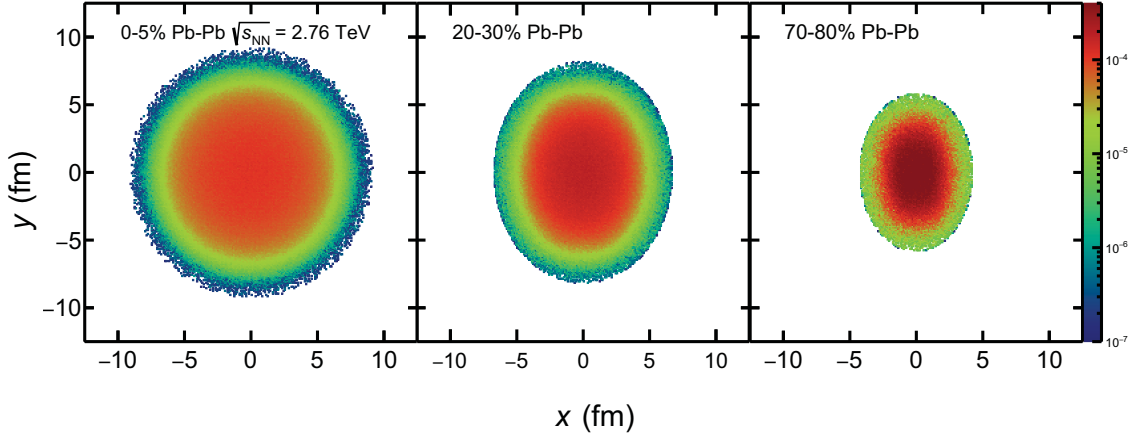


Fig. 4.6 (Color online) Number of participants distributions obtained from Glauber simulations for Pb-Pb collisions at  $\sqrt{s_{\text{NN}}} = 2.76$  TeV. Results for 0-5% (left), 20-30% (middle) and 70-80% (right) are displayed.

$R_{\text{AA}}$ , the pp production cross section of high  $p_{\text{T}}$  particle goes like:

$$\frac{d^2\sigma_{\text{pp}}(p_{\text{T}})}{dydp_{\text{T}}} \propto \frac{1}{p_{\text{T}}^n} \quad (4.3)$$

Therefore, a countervailing effect on  $R_{\text{AA}}$  is expected since the power  $n$  decreases with increasing  $\sqrt{s_{\text{NN}}}$ .

As discussed in [66], at large transverse momenta, yields are mainly suppressed by means of medium induced gluon radiation accompanying multiple scattering. To model energy loss effects, the authors proposed to convolute the vacuum (pp) production cross section of the particle with energy  $p_{\text{T}} + \varepsilon$  with the distribution  $D(\varepsilon)$  that describes specifically the additional energy loss  $\varepsilon$  due to medium induced gluon radiation in the final state. Thus, the minimum bias (centrality integrated) heavy-ion production cross section reads:

$$\frac{d^2\sigma_{\text{AA}}(p_{\text{T}})}{dydp_{\text{T}}} \propto \int_0^\infty d\varepsilon D(\varepsilon) \frac{d^2\sigma_{\text{pp}}(p_{\text{T}} + \varepsilon)}{dydp_{\text{T}}} \quad (4.4)$$

Where  $\varepsilon$  is characterized by the scale  $\omega_{\text{c}} = \hat{q}L^2/2$  being  $\hat{q}$  the transport coefficient which controls the medium dependence of the energy loss and  $L$  the medium length. The quenching effect can be modelled by the substitution:

$$\frac{d^2\sigma_{\text{AA}}(p_{\text{T}})}{dydp_{\text{T}}} = \frac{d^2\sigma_{\text{pp}}(p_{\text{T}} + \delta_{p_{\text{T}}})}{dydp_{\text{T}}} \quad (4.5)$$

Taking into account the interplay between the energy loss and the pp cross section fall-off, the  $p_T$  dependent expression for the shift goes like:

$$\delta_{p_T} \approx (p_T \omega_c)^{1/2} \quad (4.6)$$

Considering  $\omega_c = \hat{q}L^2/2$  and that the ideal estimate from pQCD calculations yields to  $\hat{q} \propto \varepsilon^{3/4}$  [23], being  $\varepsilon$  the energy density of the system. One would expect:

$$\delta_{p_T} \approx p_T^{1/2} \varepsilon^{3/8} L \quad (4.7)$$

Clearly,  $\delta_{p_T}$  does not equal the mean medium induced energy loss,  $\Delta E \propto L^2$ . It has been shown that  $\delta_{p_T}$  can be related with the fractional momentum loss [67] and that a linear relation between fractional momentum loss and  $\varepsilon^{3/8}L$  is required in order to simultaneously describe the azimuthal anisotropies and  $R_{AA}$  at high  $p_T$  [68]. Moreover, a recent work has also exploited these ideas in order to explain scaling properties of  $R_{AA}$  [69].

Inspired by recent data-driven studies, where the parton energy loss has been separately studied as a function of the Bjorken energy density [24] times the formation time ( $\varepsilon_{Bj} \tau_0$ ) [65] and a characteristic path-length [68, 70], in the present work other possibilities are explored. Namely, based on the preceding discussion the fractional momentum loss is studied as a function of  $\varepsilon_{Bj} \tau_0$  and  $L$ . Where, for the estimation of the characteristic path length the different geometry for the trajectories have been taken into account. To this end, the ideas presented in [71, 72] were implemented. Namely, energy density distributions estimated with Glauber simulations [73] were considered as the distributions of the scattering centers. This allows to test the previously discussed energy loss model [66] by means of the fractional momentum loss for several transverse momentum values and for the top energy reached at the LHC,  $\sqrt{s_{NN}} = 5.02$  TeV [26].

### Calculation of path length, Bjorken energy density and fractional momentum loss

Table 4.1 shows the different data and the inelastic nucleon-nucleon cross sections which were used to extract the quantities listed below.

**Characteristic path-length.** For each colliding system (see table 4.1), the nuclear overlap area was estimated from the number of participants ( $N_{part}$ ) distribution obtained from Glauber simulations [73]. The scattering centers were randomly generated following such a distribution which is denser in the middle and decreasing toward the edge. Some examples are shown in Fig. 4.6 which displays the distributions of the location of the scattering centers assumed for central (0-5%), semi-central (20-30%) and peripheral (70-80%) Pb-Pb collisions

System	$\sqrt{s_{\text{NN}}}$ (GeV)	$\sigma_{\text{NN}}^{\text{inel}}$ (mb)
Au-Au	62.4 [65]	36.0
Au-Au	200 [65]	42.3
Cu-Cu	200 [65]	42.3
Pb-Pb	2760 [17]	64.0
Pb-Pb	5020 [26]	70.0

Table 4.1 The inelastic nucleon-nucleon cross section for the different systems considered in this work.

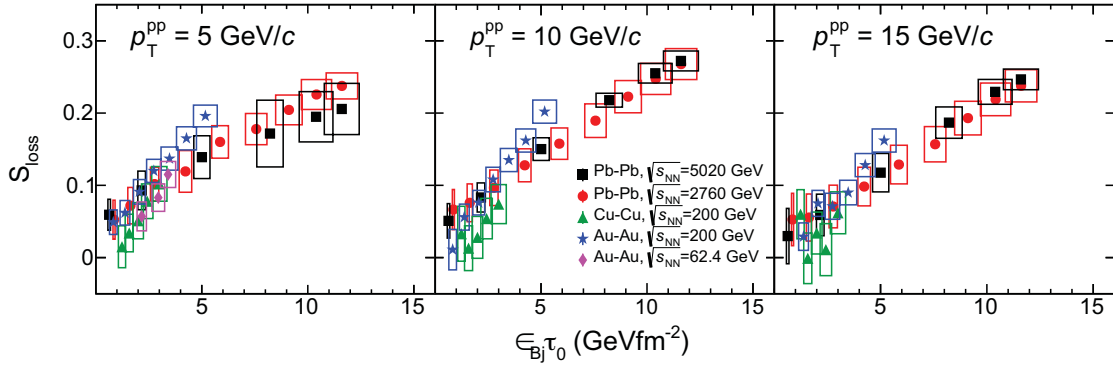


Fig. 4.7 (Color online) Fractional momentum loss ( $S_{\text{loss}}$ ) as a function of  $\epsilon_{\text{Bj}}\tau_0$ . Results for three values of transverse momentum measured in pp collisions are displayed:  $p_T^{\text{pp}} = 5$  GeV/c (left), 10 GeV/c (middle) and 15 GeV/c (right). Data from Pb-Pb at  $\sqrt{s_{\text{NN}}} = 2.76$  [74] and 5.02 TeV [26], Au-Au at 62.4 and 200 GeV, and Cu-Cu at  $\sqrt{s_{\text{NN}}} = 200$  GeV [65] are used for the extraction of the quantities. Systematic uncertainties are displayed as boxes around the data points.

at  $\sqrt{s_{\text{NN}}} = 2.76$  TeV. Then, for each production center the direction was determined by randomly sampling the azimuthal angle using a uniform distribution between 0 and  $2\pi$  rad. With this information the distance from the scattering center to the edge of the area was calculated. The RMS of the distance distribution was considered as the characteristic path-length of the system ( $L$ ). For instance, in the case of  $\sqrt{s_{\text{NN}}} = 2.76$  TeV Pb-Pb collisions the characteristic path-length ranged from 1.73 fm to 3.13 fm going from the most peripheral to the most central collisions, respectively. It is important to recall that the inclusion of more realistic models of initial conditions is not expected to modify the average geometrical properties [75].

**Energy density.** The Bjorken energy density [24] is defined as

$$\epsilon_{\text{Bj}} = \frac{1}{\tau_0 A_{\text{T}}} \left\langle \frac{dE_{\text{T}}}{dy} \right\rangle, \quad (4.8)$$

where  $\tau_0$  is the proper time when the QGP is equilibrated,  $A_T$  is the transverse area of the system and  $\langle \frac{dE_T}{dy} \rangle$  is the mean transverse energy per unit rapidity. As done it by the PHENIX Collaboration the transverse area was approximated using  $\sigma_x$  and  $\sigma_y$  being the RMS of the distributions of the  $x$  and  $y$  positions of the participant nucleons in the transverse plane, respectively. Moreover, since  $\tau_0$  is model dependent,  $\epsilon_{Bj} \tau_0$  is used instead  $\epsilon_{Bj}$  [76]. For heavy-ion collisions at  $\sqrt{s_{NN}} = 62.4$  GeV and 200 GeV, the  $\epsilon_{Bj} \tau_0$  values reported in [65] were used. Energy density values for  $\sqrt{s_{NN}} = 2.76$  TeV Pb-Pb are also available, however, we used our own estimates and they were found to be consistent to those published in [65].

Since no transverse energy data are available for the top LHC energy ( $\sqrt{s_{NN}} = 5.02$  TeV), the corresponding values were extrapolated using the fact that, within 25%,  $\langle dE_T/d\eta \rangle / \langle N_{ch}/d\eta \rangle$  vs.  $\langle N_{part} \rangle$  is nearly energy independent. This has been reported by the ALICE Collaboration, where such a scaling holds for measurements at RHIC and run I LHC energies [77]. Due to this assumption, 15% was assigned as systematic uncertainty to  $dE_T/d\eta$  for Pb-Pb collisions at  $\sqrt{s_{NN}} = 5.02$  TeV. In order to convert from pseudorapidity to rapidity, a factor that compensates the corresponding phase space difference is calculated. For  $\sqrt{s_{NN}} = 5.02$  TeV it amounts to 1.09 with a systematic uncertainty of 3% like in  $\sqrt{s_{NN}} = 2.76$  [65].

**Fractional momentum loss.** The fractional momentum loss ( $S_{loss}$ ) of large transverse momentum hadrons has been explored by the PHENIX Collaboration [65]. Such a quantity is defined as

$$S_{loss} \equiv \frac{\delta p_T}{p_T^{pp}} = \frac{p_T^{pp} - p_T^{A-A}}{p_T^{pp}} p_T \quad (4.9)$$

where  $p_T^{A-A}$  is the  $p_T$  of the A-A measurement and  $p_T^{pp}$  is that of the pp measurement scaled by the average number of binary collisions  $\langle N_{coll} \rangle$  of the corresponding A-A centrality class at the same yield of the A-A measurement. The quantity is calculated as a function of  $p_T^{pp}$  and can be related to the original partonic momentum. Therefore,  $S_{loss}$  can be used to measure the parton energy loss, which should reflect the average fractional energy loss of the initial partons.

The calculation of  $S_{loss}$  is done as follows. The inclusive charged particle  $p_T$  spectrum in pp collisions is scaled by the  $\langle N_{coll} \rangle$  value corresponding to the centrality selection of the A-A measurement. Then, a power-law function is fitted to the scaled pp spectrum. And finally, the  $p_T^{pp}$  corresponding to the scaled pp yield which equals the A-A yield, at the point of interest ( $p_T^{A-A}$ ), is found using the fit to interpolate between scaled pp points.

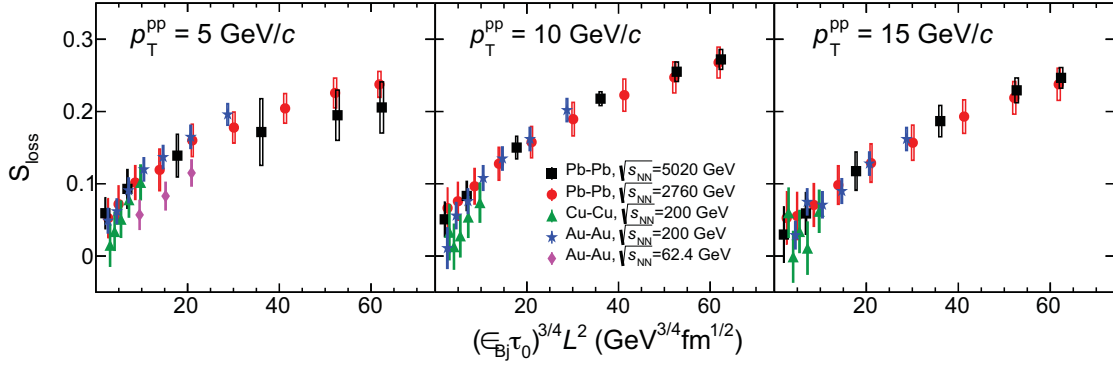


Fig. 4.8 (Color online) Fractional momentum loss ( $S_{\text{loss}}$ ) as a function of  $(\tau_0 \epsilon_{\text{Bj}})^{3/4} L^2$ . Results for three values of transverse momentum measured in pp collisions are displayed:  $p_T^{\text{pp}} = 5 \text{ GeV}/c$  (left),  $10 \text{ GeV}/c$  (middle) and  $15 \text{ GeV}/c$  (right). Data from Pb-Pb at  $\sqrt{s_{\text{NN}}} = 2.76$  [74] and  $5.02 \text{ TeV}$  [26], Au-Au at  $62.4$  and  $200 \text{ GeV}$ , and Cu-Cu at  $\sqrt{s_{\text{NN}}} = 200 \text{ GeV}$  [65] are used for the extraction of the quantities. Systematic uncertainties are displayed as boxes around the data points.

The systematic uncertainties were estimated as follows. The pp (A-A) yield was moved up (down) to the corresponding edges of the systematic uncertainties, this gives the maximum deviation between both transverse momentum spectra which can be used to quantify the maximum effect on the extraction of  $S_{\text{loss}}$ . For the most central Pb-Pb collisions at  $\sqrt{s_{\text{NN}}} = 5.02 \text{ TeV}$  the systematic uncertainties were  $\sim 17\%$ ,  $\sim 5\%$  and  $\sim 6\%$  for  $p_T^{\text{pp}} = 5, 10$  and  $15 \text{ GeV}/c$ , respectively.

## Results and discussion

At the LHC, it has been observed that the effects attributed to flow and new hadronization mechanisms like recombination, if any, are only relevant for transverse momentum below  $10 \text{ GeV}/c$  [19, 78]. Therefore, previous data-driven studies of path-length dependence of parton energy loss obtained using the elliptic flow coefficient ( $v_2$ ) measurements could only provide results for  $p_T > 10 \text{ GeV}/c$  [68]. Because for high  $p_T$ ,  $v_2$  is expected to be entirely attributed to jet quenching reflecting the azimuthal asymmetry of the path-length [70]. However, for jet quenching phenomenology it is also important to explore the intermediate  $p_T$  ( $5$ - $10 \text{ GeV}/c$ ), even if the aforementioned effects (e.g. flow) are present. Since the present work does not rely on  $v_2$  measurements,  $S_{\text{loss}}$  can be studied starting from  $p_T^{\text{pp}} = 5 \text{ GeV}/c$ .

Figure 4.7 shows the fractional momentum loss as a function of  $\epsilon_{\text{Bj}} \tau_0$  for three different  $p_T^{\text{pp}}$  values:  $5 \text{ GeV}/c$  (left),  $10 \text{ GeV}/c$  (middle) and  $15 \text{ GeV}/c$  (right). For  $p_T$  larger than

10 GeV/c the fractional momentum loss increases linearly with energy density. However, the rise of  $S_{\text{loss}}$  with  $\epsilon_{\text{Bj}}\tau_0$  seems to be steeper at RHIC than at LHC energies. For transverse momentum of 5 GeV/c,  $S_{\text{loss}} \propto \epsilon_{\text{Bj}}\tau_0$  is not valid anymore. Therefore, the universality of  $S_{\text{loss}}$  vs.  $\epsilon_{\text{Bj}}\tau_0$  reported in [65] is hard to argue. It is worth noticing that the PHENIX Collaboration reported  $S_{\text{loss}}$  in logarithmic scale, therefore the differences (which are pointed out here) were not obvious.

Now, the present study explores potential scaling properties of  $S_{\text{loss}}$  with energy density and path-length. For this, Fig. 4.8 shows the dependence of  $S_{\text{loss}}$  with  $(\epsilon_{\text{Bj}}\tau_0)^{3/4}L^2$ . The phenomenological motivation of using this variable has been already discussed in the introduction. In contrast with the previous case, the increase of  $S_{\text{loss}}$  is not linear. Moreover, as highlighted in [68] a weak point of this representation is that the extrapolation to  $(\epsilon_{\text{Bj}}\tau_0)^{3/4}L^2 = 0$  does not give a parton energy loss equal to zero. Though, the data from the different energies follow the same trend, which in principle can be attributed to the quadratic path-length which was introduced.

The top panel of Fig. 4.9 shows the  $(\epsilon_{\text{Bj}}\tau_0)^{3/8}L$  dependence of the fractional momentum loss. Within uncertainties,  $S_{\text{loss}}$  increases linearly with  $(\epsilon_{\text{Bj}}\tau_0)^{3/8}L$  for all the  $p_{\text{T}}^{\text{pp}}$  values which were explored. Moreover, the functional form of  $S_{\text{loss}}((\epsilon_{\text{Bj}}\tau_0)^{3/8}L)$  seems to be the same for all the systems which are considered. This is the first time in which an universal scaling of  $S_{\text{loss}}$  vs.  $(\epsilon_{\text{Bj}}\tau_0)^{3/8}L$  is observed for a broad interval of energies ranking from 62.4 up to 5020 GeV. It is important to mention that recent studies combining  $R_{\text{AA}}$  and  $v_n$  at high  $p_{\text{T}}$  in realistic hydrodynamics plus jet quenching simulations seem to favor a linear path length dependence of energy loss [79, 80]. Another important observation is that  $S_{\text{loss}}$  exhibits an overall decrease going from  $p_{\text{T}}^{\text{pp}} = 10$  to  $p_{\text{T}}^{\text{pp}} = 15$  GeV/c which amounts to  $\sim 20\%$ . This is consistent with the expected behavior at high  $p_{\text{T}}$ :  $S_{\text{loss}}(\sim \delta_{p_{\text{T}}}/p_{\text{T}}) \propto 1/\sqrt{p_{\text{T}}}$  which is in agreement with the observation that  $R_{\text{AA}}$  tends to unity at very high  $p_{\text{T}}$  [26].

It is worth noting that for  $p_{\text{T}}^{\text{pp}} = 5$  GeV/c a subtle change in the slope is observed at  $(\epsilon_{\text{Bj}}\tau_0)^{3/8}L \sim 4 \text{ GeV}^{3/8}\text{fm}^{1/4}$ , because there other medium effects like flow could be relevant. Actually, only for the corresponding centrality class (0-40%) the average transverse momentum for different particle species was found to scale with the hadron mass [81]. Moreover, it is well known that at intermediate  $p_{\text{T}}$  (2-10 GeV/c) the baryon-to-meson ratio in heavy-ion collisions is higher than that in pp collisions [19, 78]. In order to study the particle species dependence of  $S_{\text{loss}}$ , the bottom panel of Fig. 4.9 shows the charged pion, kaon and (anti)proton  $S_{\text{loss}}$  as a function of  $(\epsilon_{\text{Bj}}\tau_0)^{3/8}L$  for Pb-Pb collisions at  $\sqrt{s_{\text{NN}}} = 2.76$  TeV.

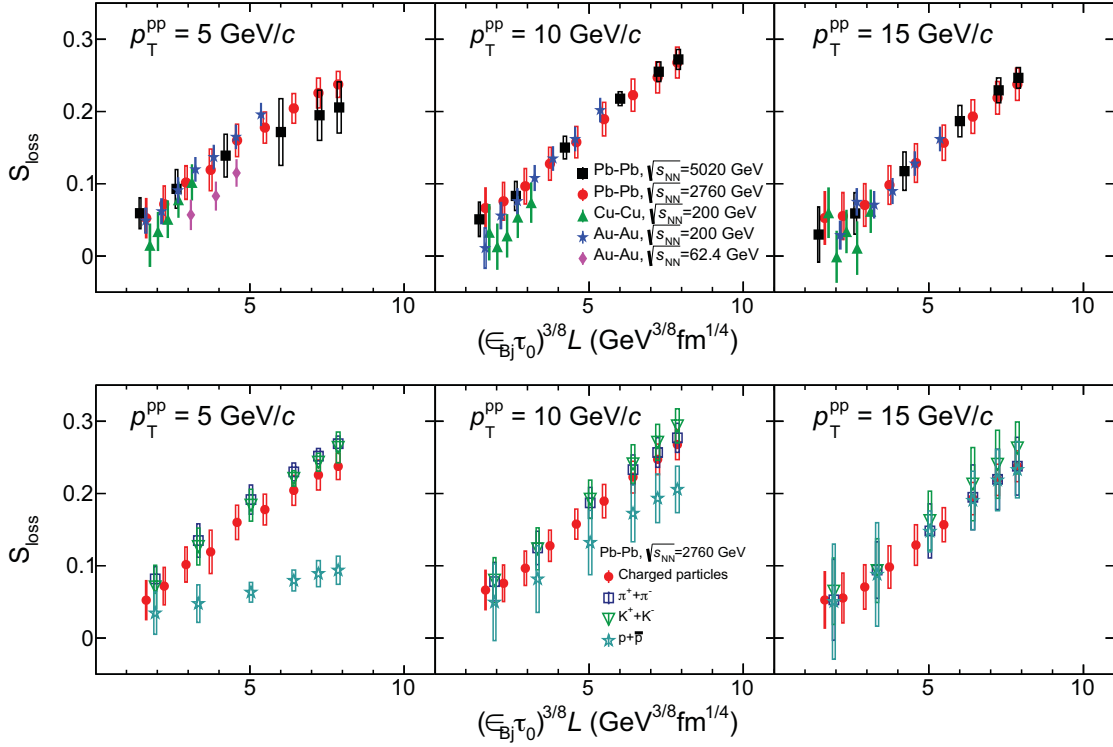


Fig. 4.9 (Color online) Fractional momentum loss ( $S_{\text{loss}}$ ) as a function of  $(\tau_0 \epsilon_{Bj})^{3/8} L$ . Results for three values of transverse momentum measured in pp collisions are displayed:  $p_T^{\text{pp}} = 5$  GeV/c (left), 10 GeV/c (middle) and 15 GeV/c (right). Data from Pb-Pb at  $\sqrt{s_{\text{NN}}} = 2.76$  [74, 78] and 5.02 TeV [26], Au-Au at 62.4 and 200 GeV, and Cu-Cu at  $\sqrt{s_{\text{NN}}} = 200$  GeV [65] are used for the extraction of the quantities. Systematic uncertainties are displayed as boxes around the data points. Results for inclusive charged particles measured at different  $\sqrt{s_{\text{NN}}}$  are displayed in the top panel. The bottom panel shows the results for charged pions, kaons and (anti)protons in Pb-Pb collisions at  $\sqrt{s_{\text{NN}}} = 2.76$  TeV.

Within uncertainties, for  $p_T^{\text{pp}} \geq 10$  GeV/c the functional form of  $S_{\text{loss}}$  is the same for the different identified particles and consistent with that measured for inclusive charged particles. While, for  $p_T^{\text{pp}} = 5$  GeV/c, the functional form of  $S_{\text{loss}}$  is only the same for inclusive charged particles, pions and kaons. Albeit the slope of the increase is significantly reduced for (anti)protons,  $S_{\text{loss}}$  is still observed to increase linearly with  $(\epsilon_{Bj} \tau_0)^{3/8} L$ . Therefore, the change in the particle composition at  $p_T < 10$  GeV/c for 0-40% Pb-Pb collisions could cause the subtle change in the slope at  $(\epsilon_{Bj} \tau_0)^{3/8} L \sim 4$  GeV $^{3/8}$ fm $^{1/4}$  observed in the top panel of Fig. 4.9.

Last but not least, it is important to point out that assuming  $\epsilon_{Bj} \tau_0$  between 0.2 and 1.2 GeV/fm $^2$  as calculated in the string percolation model for p-Pb collisions at 5.02 TeV [82]. Or



$\epsilon_{\text{Bj}} \tau_0 \sim 0.641 \text{ GeV/fm}^2$  which has been extracted from minimum bias pp collisions at  $\sqrt{s} = 7$  and 8 TeV [83]. One would expect jet quenching in p-Pb collisions, albeit, the size of the effect would be rather small for  $p_{\text{T}}^{\text{pp}} > 10 \text{ GeV}/c$  ( $0 < S_{\text{loss}} < 0.05$ ) compared with the large one predicted for pp collisions by some models [84]. However, within the current systematic uncertainties reported for p-Pb collisions at  $\sqrt{s_{\text{NN}}} = 5.02 \text{ TeV}$  it is hard to draw a conclusion based on data [85, 26, 86]. The results suggest the importance of studying how different QGP-related observables evolve as a function of quantities like energy density which is crucial to understand the similarities between pp and AA collisions [87].

## Conclusions

The inclusive charged particle production in heavy-ion collisions at  $\sqrt{s_{\text{NN}}} = 62.4$  and 200 GeV (2.76 and 5.02 TeV) measured by experiments at the RHIC (LHC) were used to extract the fractional momentum loss ( $S_{\text{loss}}$ ) and the Bjorken energy density. Using MC Glauber simulations, a characteristic path-length was estimated for the different collision centralities and for each colliding system. Surprisingly, for all the transverse momentum values which were explored:  $5 < p_{\text{T}} < 20 \text{ GeV}/c$ ,  $S_{\text{loss}}$  was found to increase linearly with  $(\epsilon_{\text{Bj}} \tau_0)^{3/8} L$  being  $\tau_0$  the equilibration time. Moreover, an universal functional form was found to describe the data from the different colliding systems which were analysed. In contrast, this universal (linear) behaviour is not observed if the scaling variable  $(\epsilon_{\text{Bj}} \tau_0)^{3/8} L$  is replaced by  $\epsilon_{\text{Bj}} \tau_0 ((\epsilon_{\text{Bj}} \tau_0)^{3/4} L^2)$ . The linear increase of  $S_{\text{loss}}$  is also observed for identified charged particles (pions, kaons and protons) even for  $p_{\text{T}}^{\text{pp}} = 5 \text{ GeV}/c$ . The behaviour of data could provide additional constraints to phenomenological models of jet quenching not only for heavy-ion collisions but also in the jet quenching searches in small collisions systems.

# Chapter 5

## Conclusions

In this thesis, the measurement of primary charged pions, kaons and (anti)protons in pp and Pb–Pb collisions at  $\sqrt{s_{\text{NN}}} = 5.02$  TeV using the ALICE Time Projection Chamber was accomplished. It is the first time that a low- $p_{\text{T}}$  (below 1 GeV/ $c$ ) PID analysis using the TPC has been carried on. The measurement of the TPC was combined with the corresponding measurements of the ITS, TOF, and HMPID ALICE detectors. An additional analysis based on the study of the decaying kink topology of charged kaons was also taken into account. The merging of the different measurements provide an overall  $p_{\text{T}}$  spectra of charged pions, kaons, and protons in an interval ranging from  $\sim 200$  MeV/ $c$  up to 12 GeV/ $c$  for 10 different centrality classes and the corresponding measurements for MB pp collisions.

The  $p_{\text{T}}$  spectra of identified charged particles in pp and Pb–Pb collisions can reveal important information such as the evolution and dynamics of the bulk production ( $p_{\text{T}} < 2$  GeV/ $c$ ). A shift of peak around 3 GeV/ $c$  in the baryon-to-meson ratio toward higher values of  $p_{\text{T}}$  in the baryon-to-meson ratio in Pb–Pb collisions at  $\sqrt{s_{\text{NN}}} = 5.02$  TeV was observed, which was attributed to a stronger presence of radial flow. In addition, by means of a Blast-Wave model, an increase of approximately 3% of the transverse expansion velocity in Pb–Pb collisions at  $\sqrt{s_{\text{NN}}} = 5.02$  TeV with respect to the corresponding collisions at  $\sqrt{s_{\text{NN}}} = 2.76$  TeV was observed. Studies of anisotropic flow, revealed an increase of  $v_2$ ,  $v_3$ , and  $v_4$  from Pb–Pb collisions at 2.76 to 5.02 TeV. This results showed to be more consistent with the hydrodynamical approach of anisotropic flow when a constant value of the shear viscosity ( $\eta/s$ ) is used rather than a temperature dependent  $\eta/s$ .

The spectra in the  $p_{\text{T}}$  interval,  $2 \lesssim p_{\text{T}} \lesssim 10$  GeV/ $c$  can be useful to test recombination models.

---

In the high  $p_T$  region,  $p_T > 10 \text{ GeV}/c$ , the  $R_{AA}$  was extracted for all the different species and for all the different centrality classes explored. The largest suppression was observed in the most central collisions and decreased towards peripheral collisions. However, the characteristic behavior of the  $R_{AA}$  for  $p_T > 8 \text{ GeV}/c$  is the same for pions, kaons and protons. Consequently, a different study aimed to understand parton energy loss was carried on. In this study, high  $p_T$  hadrons were used as proxies for jets to study parton energy loss. In fact, this study surveyed the fractional momentum loss from RHIC to LHC energies. It was concluded that a linear universal scaling of  $S_{\text{loss}}$  with  $(\epsilon\tau_0)^{3/8}L$  was observed for all the colliding systems explored. This linear behavior was confirmed when contrasting the correlation,  $S_{\text{loss}}$  vs.  $(\epsilon\tau_0)^{3/8}L$  of inclusive charged particles with the corresponding of identified particles.

# References

- [1] Renu Bala, Irais Bautista, Jana Bielcikova, and Antonio Ortiz. Heavy-ion physics at the LHC: Review of Run I results. *Int. J. Mod. Phys.*, E25(07):1642006, 2016.
- [2] Ulrich W. Heinz and Maurice Jacob. Evidence for a new state of matter: An Assessment of the results from the CERN lead beam program. 2000.
- [3] John Adams et al. Experimental and theoretical challenges in the search for the quark gluon plasma: The STAR Collaboration's critical assessment of the evidence from RHIC collisions. *Nucl. Phys.*, **A757**:102–183, 2005.
- [4] K. Adcox et al. Formation of dense partonic matter in relativistic nucleus-nucleus collisions at RHIC: Experimental evaluation by the PHENIX collaboration. *Nucl. Phys.*, **A757**:184–283, 2005.
- [5] P. Huovinen, P. F. Kolb, Ulrich W. Heinz, P. V. Ruuskanen, and S. A. Voloshin. Radial and elliptic flow at RHIC: Further predictions. *Phys. Lett.*, B503:58–64, 2001.
- [6] Berndt Muller and James L. Nagle. Results from the relativistic heavy ion collider. *Ann. Rev. Nucl. Part. Sci.*, 56:93–135, 2006.
- [7] The ALICE collaboration. Alice: Physics performance report, volume i. *Journal of Physics G: Nuclear and Particle Physics*, 30(11):1517, 2004.
- [8] The ALICE collaboration. Alice: Physics performance report, volume ii. *Journal of Physics G: Nuclear and Particle Physics*, 32(10):1295, 2006.
- [9] C. M. Hung and E. Shuryak. Equation of state, radial flow, and freeze-out in high energy heavy ion collisions. *Phys. Rev. C*, 57:1891–1906, Apr 1998.
- [10] Tuva Richert and ALICE collaboration. Alice summary of light flavour results at intermediate and high p t. *Journal of Physics: Conference Series*, 636(1):012009, 2015.
- [11] Stanley J. Brodsky and Anne Sickles. The baryon anomaly: Evidence for color transparency and direct hadron production at rhic. *Physics Letters B*, 668(2):111 – 115, 2008.
- [12] R. J. Fries, B. Müller, C. Nonaka, and S. A. Bass. Hadron production in heavy ion collisions: Fragmentation and recombination from a dense parton phase. *Phys. Rev. C*, 68:044902, Oct 2003.

- [13] V. Topor Pop, M. Gyulassy, J. Barrette, C. Gale, X. N. Wang, and N. Xu. Baryon junction loops and the baryon-meson anomaly at high energies. *Phys. Rev. C*, 70:064906, Dec 2004.
- [14] U. W. Heinz E. Schnedermann, J. Sollfrank. Thermal phenomenology of hadrons from 200-a/gev s+s collisions. *Phys. Rev.*, 48:2462–2475, 1993.
- [15] A. Tawfik and T. Harko. Quark-hadron phase transitions in the viscous early universe. *Phys. Rev. D*, 85:084032, Apr 2012.
- [16] J. D. Bjorken. Energy Loss of Energetic Partons in Quark - Gluon Plasma: Possible Extinction of High p(t) Jets in Hadron - Hadron Collisions. 1982.
- [17] J. et al. Adam. Centrality dependence of the nuclear modification factor of charged pions, kaons, and protons in pb-pb collisions at  $\sqrt{s_{NN}} = 2.76$  tev. *Physical Review C*, 93(3), Mar 2016.
- [18] Michael L. Miller, Klaus Reygers, Stephen J. Sanders, and Peter Steinberg. Glauber modeling in high-energy nuclear collisions. *Annual Review of Nuclear and Particle Science*, 57(1):205–243, 2007.
- [19] Betty Bezverkhny Abelev et al. Production of charged pions, kaons and protons at large transverse momenta in pp and Pb-Pb collisions at  $\sqrt{s_{NN}} = 2.76$  TeV. *Phys. Lett.*, **B736**:196–207, 2014.
- [20] A. Adare et al. Scaling properties of fractional momentum loss of high- $p_T$  hadrons in nucleus-nucleus collisions at  $\sqrt{s_{NN}}$  from 62.4 gev to 2.76 tev. *Phys. Rev. C*, 93:024911, Feb 2016.
- [21] R. Baier, Yuri L. Dokshitzer, S. Peigne, and D. Schiff. Induced gluon radiation in a QCD medium. *Phys. Lett.*, B345:277–286, 1995.
- [22] R. Baier, D. Schiff, and B. G. Zakharov. Energy loss in perturbative QCD. *Ann. Rev. Nucl. Part. Sci.*, 50:37–69, 2000.
- [23] R. Baier. Jet quenching. *Nucl. Phys.*, **A715**:209–218, 2003.
- [24] J. D. Bjorken. Highly Relativistic Nucleus-Nucleus Collisions: The Central Rapidity Region. *Phys. Rev.*, **D27**:140–151, 1983.
- [25] Antonio Ortiz and Omar Vázquez. Energy density and path-length dependence of the fractional momentum loss in heavy-ion collisions at  $\sqrt{s_{NN}}$  from 62.4 to 5020 GeV. *Phys. Rev.*, C97(1):014910, 2018.
- [26] Vardan Khachatryan et al. Charged-particle nuclear modification factors in Pb-Pb and p-Pb collisions at  $\sqrt{s_{NN}} = 5.02$  TeV. *JHEP*, **04**:039, 2017.
- [27] Kenneth G. Wilson. Confinement of quarks. *Phys. Rev. D*, 10:2445–2459, Oct 1974.
- [28] F. Karsch. Lattice QCD at high temperature and density. *Lect. Notes Phys.*, 583:209–249, 2002.

- [29] A. Andronic, P. Braun-Munzinger, K. Redlich, and J. Stachel. Decoding the phase structure of QCD via particle production at high energy. 2017.
- [30] A. Bazavov et al. Equation of state in (2+1)-flavor QCD. *Phys. Rev.*, D90:094503, 2014.
- [31] Szabolcs Borsanyi, Zoltan Fodor, Christian Hoelbling, Sandor D Katz, Stefan Krieg, Claudia Ratti, and Kalman K. Szabo. Is there still any  $T_c$  mystery in lattice QCD? Results with physical masses in the continuum limit III. *JHEP*, 09:073, 2010.
- [32] Szabolcs Borsanyi, Zoltan Fodor, Christian Hoelbling, Sandor D. Katz, Stefan Krieg, and Kalman K. Szabo. Full result for the QCD equation of state with 2+1 flavors. *Phys. Lett.*, B730:99–104, 2014.
- [33] P. Braun-Munzinger and J. Wambach. The Phase Diagram of Strongly-Interacting Matter. *Rev. Mod. Phys.*, 81:1031–1050, 2009.
- [34] F. Karsch and E. Laermann. Thermodynamics and in medium hadron properties from lattice QCD. 2003.
- [35] P. Petreczky. Lattice QCD at non-zero temperature. *J. Phys.*, G39:093002, 2012.
- [36] Owe Philipsen. The QCD equation of state from the lattice. *Prog. Part. Nucl. Phys.*, 70:55–107, 2013.
- [37] M. A. Stephanov. QCD phase diagram: An Overview. *PoS*, LAT2006:024, 2006.
- [38] Sourav Sarkar, Helmut Satz, and Bikash Sinha. *The physics of the quark-gluon plasma: introductory lectures*. Springer-Verlag, 2010.
- [39] Siegfried Bethke. Experimental tests of asymptotic freedom. *Prog. Part. Nucl. Phys.*, 58:351–386, 2007.
- [40] Krisztián Krajczár and the CMS Collaboration. Charged hadron multiplicity and transverse energy densities in pbbp collisions from cms. *Journal of Physics G: Nuclear and Particle Physics*, 38(12):124041, 2011.
- [41] Raimond Snellings. Elliptic Flow: A Brief Review. *New J. Phys.*, 13:055008, 2011.
- [42] Kohsuke Yagi, Tetsuo Hatsuda, and Yasuo Miake. *Quark-Gluon Plasma: From Big Bang to Little Bang*. Cambridge monographs on particle physics, nuclear physics, and cosmology. Cambridge Univ. Press, Cambridge, 2005.
- [43] Peter Braun-Munzinger, Krzysztof Redlich, and Johanna Stachel. Particle production in heavy ion collisions. 2003.
- [44] Anton Andronic. An overview of the experimental study of quark-gluon matter in high-energy nucleus-nucleus collisions. *Int. J. Mod. Phys.*, A29:1430047, 2014.
- [45] A. Andronic, P. Braun-Munzinger, and J. Stachel. Thermal hadron production in relativistic nuclear collisions: The Hadron mass spectrum, the horn, and the QCD phase transition. *Phys. Lett.*, B673:142–145, 2009. [Erratum: *Phys. Lett.* B678,516(2009)].

- [46] M. Floris. Hadron yields and the phase diagram of strongly interacting matter. *Nuclear Physics A*, 931(Supplement C):103 – 112, 2014. QUARK MATTER 2014.
- [47] J. et al. Adam. Anisotropic flow of charged particles in pb-pb collisions at  $\sqrt{s_{NN}} = 5.02$  TeV. *Phys. Rev. Lett.*, 116:132302, Apr 2016.
- [48] Ante Bilandzic, Raimond Snellings, and Sergei Voloshin. Flow analysis with cumulants: Direct calculations. *Phys. Rev. C*, 83:044913, Apr 2011.
- [49] R. J. Glauber. Cross sections in deuterium at high energies. *Phys. Rev.*, 100:242–248, Oct 1955.
- [50] Michael L. Miller, Klaus Reygers, Stephen J. Sanders, and Peter Steinberg. Glauber Modeling in High-Energy Nuclear Collisions. *Annual Review of Nuclear and Particle Science*, 57:205–243, 2007.
- [51] The ALICE collaboration. Performance of the alice vzero system. *Journal of Instrumentation*, 8(10):P10016, 2013.
- [52] P et al. Cortese. *ALICE forward detectors: FMD, TO and VO: Technical Design Report*. Technical Design Report ALICE. CERN, Geneva, 2004. Submitted on 10 Sep 2004.
- [53] K. et al. Aamodt. Centrality dependence of the charged-particle multiplicity density at midrapidity in pb-pb collisions at  $\sqrt{s_{NN}} = 2.76$  TeV. *Phys. Rev. Lett.*, 106:032301, Jan 2011.
- [54] Antonin Maire. ALICE TPC sectors and pad rows. General Photo, Oct 2011.
- [55] Andrea Rossi. Alice Alignment, Tracking and Physics Performance Results. *PoS, VERTEX2010:017*, 2010.
- [56] F. Anghinolfi et al. Ieee trans. *Nucl. Science*, 42(4):772, 1995.
- [57] J. et al. Adam. Centrality dependence of the nuclear modification factor of charged pions, kaons, and protons in pb-pb collisions at  $\sqrt{s_{NN}} = 2.76$  tev. *Phys. Rev. C*, 93:034913, Mar 2016.
- [58] Jaroslav Adam et al. Multiplicity dependence of charged pion, kaon, and (anti)proton production at large transverse momentum in p-Pb collisions at  $\sqrt{s_{NN}} = 5.02$  TeV. *Phys. Lett.*, B760:720–735, 2016.
- [59] B. Abelev et al. Production of charged pions, kaons and protons at large transverse momenta in pp and pb–pb collisions at  $\sqrt{s_{NN}} = 2.76$  tev. *Physics Letters B*, 736:196–207, 2014.
- [60] Berndt MÄCeller. Investigation of hot qcd matter: theoretical aspects. *Physica Scripta*, 2013(T158):014004, 2013.
- [61] Alejandro Ayala, Adnan Bashir, J.J. Cobos-Martínez, Saúl Hernández-Ortiz, and Alfredo Raya. The effective qcd phase diagram and the critical end point. *Nuclear Physics B*, 897:77–86, 2015.

- [62] Tanmoy Bhattacharya, Michael I. Buchoff, Norman H. Christ, H.-T. Ding, Rajan Gupta, Chulwoo Jung, F. Karsch, Zhongjie Lin, R. D. Mawhinney, Greg McGlynn, Swagato Mukherjee, David Murphy, P. Petreczky, Dwight Renfrew, Chris Schroeder, R. A. Soltz, P. M. Vranas, and Hantao Yin. QCD Phase Transition with Chiral Quarks and Physical Quark Masses. *Phys. Rev. Lett.*, 113:082001, Aug 2014.
- [63] I. Arsene et al. Quark–gluon plasma and color glass condensate at rhic? the perspective from the brahms experiment. *Nuclear Physics A*, 757:1–27, 2005.
- [64] J. M. Burward-Hoy. Centrality dependence of inclusive identified hadrons in PHENIX. In *18th Winter Workshop on Nuclear Dynamics (WWND 2002) Nassau, Bahamas, January 20-22, 2002*, 2002.
- [65] A. Adare et al. Scaling properties of fractional momentum loss of high- $p_T$  hadrons in nucleus-nucleus collisions at  $\sqrt{s_{NN}}$  from 62.4 GeV to 2.76 TeV. *Phys. Rev.*, **C93**(2):024911, 2016.
- [66] R. Baier, Yuri L. Dokshitzer, Alfred H. Mueller, and D. Schiff. Quenching of hadron spectra in media. *JHEP*, 09:033, 2001.
- [67] Konrad Tywoniuk. Parton energy loss in QCD matter. In *8th International Conference on Hard and Electromagnetic Probes of High-energy Nuclear Collisions: Hard Probes 2016 (HP2016) Wuhan, Hubei, China, September 23-27, 2016*, 2017.
- [68] Peter Christiansen, Konrad Tywoniuk, and Vytautas Vislavicius. Universal scaling dependence of QCD energy loss from data driven studies. *Phys. Rev.*, **C89**(3):034912, 2014.
- [69] François Arleo. Quenching of Hadron Spectra in Heavy Ion Collisions at the LHC. *Phys. Rev. Lett.*, 119(6):062302, 2017.
- [70] Peter Christiansen. Event-Shape Engineering and Jet Quenching. *J. Phys. Conf. Ser.*, **736**(1):012023, 2016.
- [71] Alejandro Ayala, Jamal Jalilian-Marian, J. Magnin, Antonio Ortiz, G. Paic, and Maria Elena Tejeda-Yeomans. Three and two-hadron correlations in  $s(NN)^{1/2} = 200$ -GeV proton-proton and nucleus-nucleus collisions. *Phys. Rev. Lett.*, **104**:042301, 2010.
- [72] A. Dainese, C. Loizides, and G. Paic. Leading-particle suppression in high energy nucleus-nucleus collisions. *Eur. Phys. J.*, **C38**:461–474, 2005.
- [73] C. Loizides, J. Nagle, and P. Steinberg. Improved version of the PHOBOS Glauber Monte Carlo. *SoftwareX*, **1-2**:13–18, 2015.
- [74] Betty Abelev et al. Centrality Dependence of Charged Particle Production at Large Transverse Momentum in Pb–Pb Collisions at  $\sqrt{s_{NN}} = 2.76$  TeV. *Phys. Lett.*, **B720**:52–62, 2013.
- [75] Charles Gale, Sangyong Jeon, and Bjoern Schenke. Hydrodynamic Modeling of Heavy-Ion Collisions. *Int. J. Mod. Phys.*, A28:1340011, 2013.



- [76] E. Cuautle and G. Paic. The energy density representation of the strangeness enhancement from p+p to Pb+Pb. 2016.
- [77] Jaroslav Adam et al. Measurement of transverse energy at midrapidity in Pb-Pb collisions at  $\sqrt{s_{NN}} = 2.76$  TeV. *Phys. Rev.*, **C94**(3):034903, 2016.
- [78] Jaroslav Adam et al. Centrality dependence of the nuclear modification factor of charged pions, kaons, and protons in Pb-Pb collisions at  $\sqrt{s_{NN}} = 2.76$  TeV. *Phys. Rev.*, **C93**(3):034913, 2016.
- [79] Jacquelyn Noronha-Hostler, Barbara Betz, Jorge Noronha, and Miklos Gyulassy. Event-by-event hydrodynamics + jet energy loss: A solution to the  $R_{AA} \otimes v_2$  puzzle. *Phys. Rev. Lett.*, 116(25):252301, 2016.
- [80] Barbara Betz, Miklos Gyulassy, Matthew Luzum, Jorge Noronha, Jacquelyn Noronha-Hostler, Israel Portillo, and Claudia Ratti. Cumulants and nonlinear response of high  $p_T$  harmonic flow at  $\sqrt{s_{NN}} = 5.02$  TeV. *Phys. Rev.*, C95(4):044901, 2017.
- [81] Antonio Ortiz. Mean  $p_T$  scaling with  $m/n_q$  at the LHC: Absence of (hydro) flow in small systems? *Nucl. Phys.*, **A943**:9–17, 2015.
- [82] I. Bautista Guzman, R. Alvarado, and P. Fierro. Collectivity in pPb and pp collisions with the string percolation model. In *Proceedings of the 38th International Conference on High Energy Physics (ICHEP2016). 3-10 August 2016. Chicago, USA*, page 1152, 2016.
- [83] Csanád, Máté and Csörgö, Tamás and Jiang, Ze-Fang and Yang, Chun-Bin. Initial energy density of  $\sqrt{s} = 7$  and 8 TeV p+p collisions at the LHC. *Universe*, 3(1):9, 2017.
- [84] B. G. Zakharov. Parton energy loss in the mini quark-gluon plasma and jet quenching in proton-proton collisions. *J. Phys.*, **G41**:075008, 2014.
- [85] Jaroslav Adam et al. Multiplicity dependence of charged pion, kaon, and (anti)proton production at large transverse momentum in p-Pb collisions at  $\sqrt{s_{NN}} = 5.02$  TeV. *Phys. Lett.*, **B760**:720–735, 2016.
- [86] Georges Aad et al. Transverse momentum, rapidity, and centrality dependence of inclusive charged-particle production in  $\sqrt{s_{NN}} = 5.02$  TeV p + Pb collisions measured by the ATLAS experiment. *Phys. Lett.*, **B763**:313–336, 2016.
- [87] G. Paic and E. Cuautle. Energy density in small systems equal to the one in heavy-ion collisions. *Int. J. Mod. Phys.*, **E25**(07):1642009, 2016.
- [88] Claus Grupen and Boris Shwartz. *Particle Detectors*. Cambridge Monographs on Particle Physics, Nuclear Physics and Cosmology. Cambridge University Press, 2 edition, 2008.
- [89] C. Patrignani et al. Review of Particle Physics. *Chin. Phys.*, C40(10):100001, 2016.

# Appendix A

## The Bethe-Bloch formula

This appendix is meant to review the theoretical framework used to describe the interaction of particles with matter. The review mainly focusses on the energy loss by ionization and excitation of atoms by relativistic particles. The average energy loss per length ( $\langle \frac{dE}{dx} \rangle$ ) is described by the Bethe-Bloch relation [88]

$$-\frac{dE}{dx} = 4\pi N_A r_e^2 m_e c^2 z^2 \frac{Z}{A} \frac{1}{\beta^2} \left( \ln \frac{2m_e c^2 \gamma^2 \beta^2}{I} - \beta^2 - \frac{\delta}{2} \right) \quad (\text{A.1})$$

where

- $z$  – charge of the incident particle in units of the elementary charge
- $Z, A$  – atomic number
- $m_e$  – electron mass
- $r_e$  – classical electron radius ( $r_e = \frac{1}{4\pi\epsilon_0} \frac{e^2}{m_e c^2}$ ) with  $\epsilon_0$  – permittivity of free space
- $N_A$  – Avogadro number ( $6.022 \times 10^{23} \text{ mol}^{-1}$ )
- $I$  – mean excitation energy, characteristic of the absorber material, which can be approximated by

$$I = 16Z^{0.9} \text{ eV for } Z > 1$$

- $\delta$  – the *density effect* parameter. It characterizes the screening of the transverse electric field of the incident particle by the charge density of atomic electrons.

In the limit,  $m_0 \gg m_e$ , the Bethe-Bloch parameterization can be approximated to

$$-\frac{dE}{dx} = 2\kappa \left( \ln \frac{E_{\text{kin}}^{\text{max}}}{I} - \beta^2 - \frac{\delta}{2} \right) \quad (\text{A.2})$$

where

$$E_{\text{kin}}^{\text{max}} \approx 2m_e c^2 \beta^2 \gamma^2$$

The units of  $-\frac{dE}{dx}$  are given as  $\text{MeV}/(\text{g}/\text{cm}^2)$ . The length unit  $dx$  (in  $\text{g}/\text{cm}^2$ ) is commonly given as  $dx = \rho ds$  with  $\rho$  density (in  $\text{g}/\text{cm}^3$ ) and  $ds$  length (in  $\text{cm}$ ) because is largely independent of the properties of the material. Equation A.1 describes only energy losses due to ionization and excitation. At high energies, radiation losses become important. However in the current study, the highest  $\beta\gamma$  is approximately 200, which is described by the logarithmic term. Figure ?? shows the correlation between the stopping power ( $= \langle -dE/dx \rangle$ ) vs.  $\beta\gamma$  of positive muons in copper.

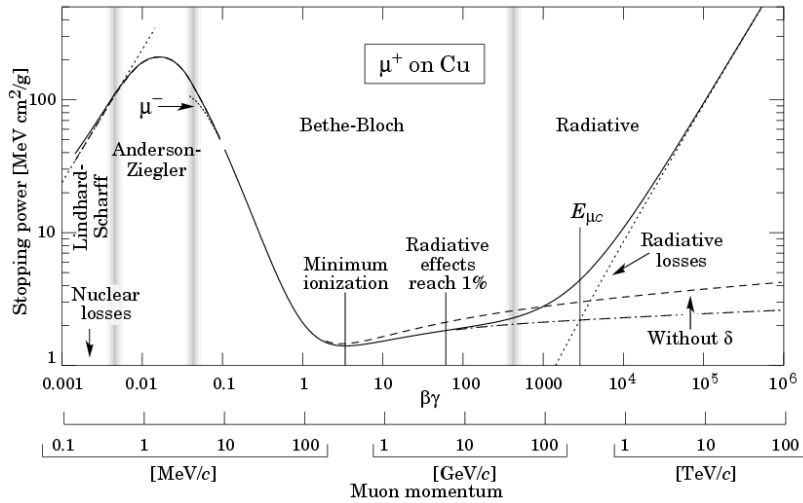


Fig. A.1 Stopping power of positive muons in copper. Figure taken from [89].